

University of Kentucky

UKnowledge

Theses and Dissertations--Civil Engineering

Civil Engineering


2024

ESTIMATION OF MECHANICAL BEHAVIOR OF UNSATURATED SOILS FROM A SOIL-WATER CHARACTERISTIC CURVE

Lucas Acheampong

University of Kentucky, lucas.acheampong@uky.edu

Author ORCID Identifier:

 <https://orcid.org/0009-0003-0335-9043>

Digital Object Identifier: <https://doi.org/10.13023/etd.2024.64>

[Right click to open a feedback form in a new tab to let us know how this document benefits you.](#)

Recommended Citation

Acheampong, Lucas, "ESTIMATION OF MECHANICAL BEHAVIOR OF UNSATURATED SOILS FROM A SOIL-WATER CHARACTERISTIC CURVE" (2024). *Theses and Dissertations--Civil Engineering*. 144.
https://uknowledge.uky.edu/ce_etds/144

This Master's Thesis is brought to you for free and open access by the Civil Engineering at UKnowledge. It has been accepted for inclusion in Theses and Dissertations--Civil Engineering by an authorized administrator of UKnowledge. For more information, please contact UKnowledge@lsv.uky.edu.

STUDENT AGREEMENT:

I represent that my thesis or dissertation and abstract are my original work. Proper attribution has been given to all outside sources. I understand that I am solely responsible for obtaining any needed copyright permissions. I have obtained needed written permission statement(s) from the owner(s) of each third-party copyrighted matter to be included in my work, allowing electronic distribution (if such use is not permitted by the fair use doctrine) which will be submitted to UKnowledge as Additional File.

I hereby grant to The University of Kentucky and its agents the irrevocable, non-exclusive, and royalty-free license to archive and make accessible my work in whole or in part in all forms of media, now or hereafter known. I agree that the document mentioned above may be made available immediately for worldwide access unless an embargo applies.

I retain all other ownership rights to the copyright of my work. I also retain the right to use in future works (such as articles or books) all or part of my work. I understand that I am free to register the copyright to my work.

REVIEW, APPROVAL AND ACCEPTANCE

The document mentioned above has been reviewed and accepted by the student's advisor, on behalf of the advisory committee, and by the Director of Graduate Studies (DGS), on behalf of the program; we verify that this is the final, approved version of the student's thesis including all changes required by the advisory committee. The undersigned agree to abide by the statements above.

Lucas Acheampong, Student

Dr. L. Sebastian Bryson, Major Professor

Dr. Mei Chen, Director of Graduate Studies

ESTIMATION OF MECHANICAL BEHAVIOR OF UNSATURATED SOILS FROM
A SOIL-WATER CHARACTERISTIC CURVE

THESIS

A thesis submitted in partial fulfillment of the
requirements for the degree of Master of Science in the
College of Engineering
at the University of Kentucky

By

Lucas Acheampong

Lexington, Kentucky

Director: Dr. L. Sebastian Bryson, Chair and Professor of Civil Engineering

Lexington, Kentucky

2024

Copyright © Lucas Acheampong 2024
<https://orcid.org/0009-0003-0335-9043>

ABSTRACT OF THESIS

ESTIMATION OF MECHANICAL BEHAVIOR OF UNSATURATED SOILS FROM A SOIL-WATER CHARACTERISTIC CURVE

The small-strain shear modulus and shear strength are two crucial mechanical behaviors used in the design of geotechnical structures and in the analyses of earth materials subjected to static and dynamic loadings. Traditional testing methods for these parameters are expensive and time-consuming. This research aimed to address these challenges by developing a model based on the inverse relationship between mechanical behavior of unsaturated soils and the soil-water characteristic curve (SWCC). The proposed model integrates a scaling function to align the SWCC with the mechanical property curve. Empirical relationships were established for the scaling function, specifically aligning with the air-entry value of the SWCC.

Recognizing that empirical relationships derived from small laboratory samples may not fully represent field conditions, this study calibrated the proposed relationships using data from large scale tests in a box. To achieve this, two soils were compacted within a large-scale test box with sensors positioned to measure matric suction, volumetric water content, and electrical conductivity at varying densities. Accelerometers were also placed to capture seismic data within the box. By correlating the small-strain shear modulus determined from shear wave velocity measurements with the proposed model, calibrations were made to better reflect large-scale test conditions. Subsequently, the modified model was applied to a field site, demonstrating satisfactory agreement with the measured data.

KEYWORDS: Mechanical Behavior, Small-Strain Shear Modulus, Soil-Water Characteristic Curve, Scaling Function, Air-Entry Value, Hysteresis.

Lucas Acheampong

(Name of Student)

April 24, 2024

Date

ESTIMATION OF MECHANICAL BEHAVIOR OF UNSATURATED SOILS FROM
A SOIL-WATER CHARACTERISTIC CURVE

By

Lucas Acheampong

Dr. L. Sebastian Bryson

Director of Thesis

Dr. Mei Chen

Director of Graduate Studies

April 24, 2024

Date

To:

My Mother, Afia Sarpong, and Uncle, Adams Fredua, this work is dedicated to you.

ACKNOWLEDGMENTS

First and foremost, Thanks be to The Almighty God for the completion of this incredible milestone.

I am deeply indebted to Dr. L. Sebastian Bryson for his unwavering belief in me and continuous inspiration throughout this journey. His guidance and supervision have been instrumental in bringing this research to fruition. I am forever grateful for his invaluable advice, which will resonate with me for years to come.

I am also immensely thankful to my esteemed committee members, Dr. Michael Kalinski and Dr. Edward Woolery, for their generous support, time, and expertise during my thesis defense. The knowledge and insights gained from their classes have significantly contributed to my understanding of earthquake engineering and geophysics.

This research owes its success to the generous funding from the United States Air Force, which facilitated the acquisition of essential equipment and materials. Additionally, the invaluable field data provided by the University of Rouen played a crucial role in bringing this study to fruition.

To my beloved family, your constant support and encouragement have been my anchor throughout my academic endeavors. I am profoundly grateful for your unwavering presence and belief in me.

Lastly, I extend my sincere appreciation to all my friends at the University of Kentucky, back home in Ghana, and around the world for their encouragement and support. Your friendship and motivation have been a constant source of strength and inspiration on this academic journey.

TABLE OF CONTENTS

ACKNOWLEDGMENTS	iii
TABLE OF CONTENTS.....	iv
LIST OF TABLES	vii
LIST OF FIGURES	viii
CHAPTER 1. INTRODUCTION	1
1.1 Problem Statement	1
1.2 Conceptual Overview of Study.....	2
1.3 Research Objectives.....	3
1.4 Contents Of Thesis.....	3
CHAPTER 2. DEVELOPMENT OF A SCALING FUNCTION TO ESTIMATE UNSATURATED MECHANICAL SOIL BEHAVIOR FROM A SOIL-WATER CHARACTERISTIC CURVE.....	6
2.1 Introduction.....	6
2.2 State of Small-Strain Shear Modulus and Shear Strength Equations for Unsaturated Soils	8
2.3 Development of Proposed Approach for Mechanical Behavior for Unsaturated Soils	9
2.3.1 Soil-Water Characteristic Curve	9
2.3.1.1 Considerations for Hysteresis	11
2.3.1.2 Mathematical Determination of the Air-Entry Value	12
2.3.2 Suction-Mechanical Relationship of Unsaturated Soils	14
2.3.3 Study Soils	16
2.3.4 Methods for Obtaining the Scaling Function, β	21
2.4 Proposed Approach for Unsaturated Small-Strain Shear Modulus	23
2.4.1 Calibration of the Material Constant for Hardin and Black (1969) Equation.....	24
2.4.2 Performance of the G-suction Equation.....	26
2.4.3 Performance of the Proposed G-suction Equation under Hydraulic Hysteresis Effects	28
2.4.4 Proposed Empirical Relationship for β for G-suction	30
2.4.5 Performance of Proposed Empirical Relationship for β for G-suction.....	32
2.5 Proposed Approach for Unsaturated Shear Strength	33
2.5.1 Performance of the τ -suction Equation	34

2.5.2	Performance of the Proposed τ -suction Equation under Hydraulic Hysteresis Effects	36
2.5.3	Proposed Empirical Relationship for β for τ -suction	37
2.5.4	Performance of Proposed Empirical Relationship for β for τ -suction	38
CHAPTER 3. Estimation of Unsaturated Small-Strain Shear Modulus in a Large-Scale Test Box and Field Site from a Soil-Water Characteristic Curve		
3.1	Introduction	40
3.2	Overview of Proposed Model to Estimate Small-Strain Shear Modulus of Unsaturated Soils	42
3.2.1	Hydrologic Behavior of Unsaturated Soils	42
3.2.2	Proposed Small-Strain Shear Modulus Model for Unsaturated Soils	44
3.2.3	Saturated Small-Strain Shear Modulus	46
3.2.4	Determination of Scaling Function	47
3.2.5	Performance Evaluation of Proposed G-suction Equation	48
3.3	Laboratory Box Testing	50
3.3.1	Test Soils and Preparation	50
3.3.2	Test Box Setup and Sensors	51
3.3.3	Testing Procedure	52
3.3.4	Hydrologic Model for Test Box	53
3.3.4.1	SWCC from Sensors	53
3.3.4.2	SWCC from Rosetta	54
3.3.5	Modification of Proposed G-Suction Equation with Box Test Data	55
3.4	Field Site	58
3.4.1	Description of Field Site	58
3.4.2	Hydrological Model for Field Site	61
3.4.3	Performance Evaluation of the Modified G-suction Equation at the Field Site	65
CHAPTER 4. SUMMARY AND CONCLUSIONS		
		68
APPENDICES		
		70
APPENDIX A - INDEX AND MECHANICAL TESTS DATA		
		71
APPENDIX B - TRIAXIAL TESTING PROCEDURE		
		77
APPENDIX C - TRIAXIAL TEST RESULTS		
		99
APPENDIX D - CODE FOR AUTOMATION FOR BENDER ELEMENTS		
		102
APPENDIX E – MATLAB CODE FOR PICKING ARRIVAL TIMES OF WAVES		
		108

APPENDIX F – ROSETTA	110
REFERENCES	111
VITA.....	119

LIST OF TABLES

Table 2-1 Geotechnical index properties of soils used to evaluate the performance of the proposed equation for small-strain shear modulus.	17
Table 2-2 SWCC fitting parameters for the study soils used for evaluating the performance of the proposed equation for small-strain shear modulus.	18
Table 2-3 Geotechnical index properties of literature soils used to evaluate the performance of the proposed equation for shear strength.	19
Table 2-4 SWCC fitting parameters for the literature soils used for evaluating the performance of the proposed equation for shear strength.	20
Table 2-5 Properties of soils used for calibrating the material constant for the Hardin and Black (1969) Equation.	25
Table 2-6. Properties of reference soils used to predict small-strain shear modulus based on knowledge of SWCC and modified G-suction equation.	32
Table 2-7. SWCC fitting parameters for the literature soil used for validating the performance of the proposed relationship for β	39
Table 3-1. Geotechnical index properties and SWCC fitting parameters of literature soils used to show inverse relationship.	44
Table 3-2. SWCC parameters and scaling function of the literature soils used to evaluate the performance of the proposed model.	49
Table 3-3. Geotechnical index properties of soils used for the box test to evaluate the performance of the proposed equation for small-strain shear modulus.	51
Table 3-4. SWCC fitting parameters for the sands from the box test data and Rosetta. ..	54
Table 3-5. Multipliers to modify the proposed G-suction model for large-scale compacted soils.	57
Table 3-6. Textural characteristics of the test site at various depths from laboratory samples.	59
Table 3-7. SWCC fitting parameters, air-entry values and scaling functions for the three areas of the field site at varying depths.	62
Table 3-8. The fitting parameters for Archie (1942) equation for the three study points of the field site.	65

LIST OF FIGURES

Figure 2-1 Soil-water characteristic curve showing the various zones and associated variables.	11
Figure 2-2 Graphical representation of the relationship between the SWCC and mechanical behavior with respect to increasing matric suction; (a) Bonny silt at 40 kPa (data from Khosravi et al., 2018a); and (b) Air-dry silty clay at 200 kPa (data from Cunningham et al., 2003).....	15
Figure 2-3 Values of β obtained from measured data for two literature soils (a) Small-strain shear modulus data for Mn Road Clay (data from Sawangsuriya et al., 2009) (b) Shear Strength data for SJ10 Hume Dam SB (data from Khalili et al., 2004).	22
Figure 2-4 Variation of the normalized small-strain shear modulus and shear strength data at the AEV with respect to the saturated measured data for different soil types.	23
Figure 2-5 Calibration of material constant, A using literature soils.	26
Figure 2-6 Measured and predicted small-strain shear modulus for six literature soils: (a) Ottawa Sand at 17.25 kPa; (b) Anaheim Clayey Sand at 35 kPa; (c) Completely Decomposed Tuff; (d) Bonny Silt-1; (e) Red Lake Falls at 35 kPa; (f) DI TH23 Slopes Clay at 35 kPa.	27
Figure 2-7 Performance of G -suction under hydraulic hysteretic effects and under different net normal stresses. In the figure, DP=Drying Path; WP=Wetting Path.	29
Figure 2-8 Variation of β to AEV for small-strain shear modulus; (a) soils with AEV less than 100 kPa; (b) For soils with AEV equal to or greater than 100 kPa.....	31
Figure 2-9 Validation of proposed equations for β with additional literature soils; (a) Compacted Silty Sand; (b) Fayette County Clay.....	33
Figure 2-10 Measured and predicted shear strength for six literature soils at constant and varying net normal stresses: (a) Madrid Grey Clay at 300kPa; (b) Guadalix Red Clay; (c) SJ10B Hume Dam Clay; (d) Mine Tailings at 150m; (e) Coarse Kaolin; (f) Botkin Pit Silt.	35
Figure 2-11 Performance of τ -suction under hysteretic effects for the Granitic Residual Clay (Han et al., 1995).....	37
Figure 2-12 The relationship between β and the AEV for shear strength using triaxial and shear strength data.....	38
Figure 2-13 Measured and predicted data using the modified Eq. (22) for the Indian Head Till at two net normal stresses.	39
Figure 3-1 Graphical representation of the relationship between the small-strain shear modulus behavior and SWCC with respect to increasing matric suction; (a) SG-2 (data from Lee et al., 2007); (b) Bonny silt at 40 kPa (data from Khosravi et al., 2018).....	45

Figure 3-2 Measured and predicted small-strain shear modulus for four literature soils: (a) Ottawa Sand at 17.25 kPa; (b) DI TH23 Slopes Clay at 35 kPa.; (c) Bonny Silt at 150 kPa; (d) Compacted Silty Sand at 400 kPa using the proposed empirical relationship in Eq. (12a). In the figure, DP=Drying Path; WP=Wetting Path.....	50
Figure 3-3 Test Box; (a) Aerial view of soil placed in box with sensors; (b) Schematic Diagram of box illustrating the setup.....	52
Figure 3-4 Wave propagation arrival times; (a) P-wave velocity; (b) S-wave velocity. ...	53
Figure 3-5 Soil-water characteristic curve for the test box from measured sensor in box and Rosetta; (a) KY River sand; and (b) Hamburg clay.	55
Figure 3-6 Rigorous approach for obtaining $\bar{\sigma}$ from measured small-strain shear modulus data and SWCC using proposed approach.....	56
Figure 3-7 Measured and predicted small-strain shear modulus data; (a) KY River sand; and (b) Hamburg clay.	57
Figure 3-8 Field site. (a) Sectional view of test site showing the various areas, dead zones. (b) Plan view showing the measured points.	59
Figure 3-9 Particle size distribution of the field site at Area 2 at depth 0.18-0.25m in comparison to the test soils in the laboratory.....	60
Figure 3-10 Variation of shear wave velocity and bulk unit weight at the three study points with depth.....	61
Figure 3-11 Comparison of porosities derived from Rosetta and shear wave velocity....	64
Figure 3-12 Variation of moisture conditions with depth. (a) electrical conductivity; (b) volumetric water content from Archie' equation.	65
Figure 3-13 Performance of the modified G-suction model in predicting the small-strain shear modulus at the three study points with depth.	67

CHAPTER 1. INTRODUCTION

1.1 Problem Statement

The mechanical behavior of soils, particularly the small-strain shear modulus and shear strength, plays a pivotal role in infrastructure design and the analyses of dynamic and static loading of earth materials. The dynamic response of soils is influenced by factors such as mean effective stress, soil structure, degree of saturation, and unit weight. Typically, since most structures are built and subjected to loads throughout their operational life above the ground water table, the impact of negative pore water pressures (matric suction) must be factored into their design and the analysis of external loads. To effectively model unsaturated soil behavior, the soil-water characteristic curve (SWCC) serves as a valuable tool (Zhai et al., 2019). The SWCC describes the relationship between soil water content (gravimetric, volumetric, and effective degree of saturation) and soil suction. The SWCC also provides hysteretic paths, enabling predictions of soil response to changing moisture conditions.

The small-strain shear modulus is defined by Atkinson and Salfors (1991) as the shear modulus measured at strain amplitudes below 1%. It is determined directly from shear wave velocity in the field from tests such as cross-hole technique, downhole technique, and spectral analysis of surface waves techniques, and in the laboratory setting from resonant column and bender elements testing. It is also determined indirectly from dynamic cone penetrometer (DCP) measurements subsequently using empirical equations to convert to California bearing ratio (CBR) and then to modulus using another empirical equation. This multistep approach compounds errors and makes it unreliable.

The shear strength of a soil reflects the soil's resistance to deformation under external loads. Triaxial and direct shear tests are commonly employed to determine shear strength. These tests not only involve the use of expensive equipments but are time-consuming to transport samples from the field to the laboratory and to run tests which can take days and weeks to complete. Another constraint is the reliance on saturated test results to predict field conditions which are usually not saturated. With the increased need to provide

preliminary analysis before and during construction over the years, these tests may not help meet project schedules.

Previous studies (Cunningham et al., 2003; Ng and Yung, 2008; Sivakumar et al., 2013; Morales et al., 2015; Ngoc et al., 2019) have highlighted an inverse *S*-shaped relationship between mechanical behavior of unsaturated soils and the SWCC. Investigating this relationship further, this research explores the impact of SWCC on both the small-strain shear modulus and shear strength on partially saturated soils.

Empirical relationships proposed by several researchers offer insights into small-strain shear modulus (Sawangsurriya et al., 2009; Xu and Zhou, 2016; Mahmoodabadi and Bryson, 2021a; Yan et al., 2022) and shear strength (Vanapalli et al., 1996; Han and Vanapalli, 2016; Zhou et al., 2016; Pham and Sutman, 2023) based on soil structure, moisture content and stress states. However, these relationships are often derived from small laboratory samples and may not fully represent field conditions. Hence, developing models applicable to both laboratory and field settings, accounting for moisture conditions, is crucial for estimating soil mechanical behavior in geotechnical engineering projects.

1.2 Conceptual Overview of Study

This study presents a model for estimating the mechanical behavior of unsaturated soils based on their inverse relationship with the soil-water characteristic curve (SWCC). The model incorporates a scaling function to describe this inverse relationship and requires inputs of saturated small-strain shear modulus and shear strength. The Mohr-Coulomb equation is recommended for estimating shear strength, while the Hardin and Black (1969) equation is recommended for determining saturated data.

The Hardin and Black (1969) equation was refined using laboratory data with varying soil textures and properties to determine the material constant, making it applicable across soil types. Additionally, it was observed that the air-entry value of the SWCC had a high correlation with the scaling function. Recognizing the pivotal role of the air-entry value in delineating the scaling function and characterizing the transition from saturated to unsaturated states, a method was described for accurately determining this parameter.

In addition, a large-scale test box was assembled with sensors placed to measure volumetric water content, matric suction and electrical conductivity for two tests compacted at varying moisture contents. Additionally, accelerometers were placed in the test box to capture wave propagation times. The data from the box setup was then used to refine the relationship for the scaling function since it was observed that the relationship derived from small laboratory specimens was not reflective of large-scale test soils and field conditions. The refined relationship together with the saturated small-strain shear modulus was then applied to a field site. The comparison with measured data demonstrated a strong agreement, affirming the reliability of the proposed model. The proposed model will be a valuable tool to provide preliminary analysis for geotechnical engineering projects.

1.3 Research Objectives

This research presents a model to estimate the mechanical behavior, that is small-strain shear modulus and shear strength, of unsaturated soils in the laboratory and field setting. The objectives of this research are:

- To develop a model for predicting unsaturated mechanical behavior, that is small-strain shear modulus and shear strength. The model depends on the inverse relationship between the mechanical behavior and soil-water characteristic curve.
- To refine the proposed model in a large-scale test box with compacted soils.
- To apply the refined model to a field site with varying levels of compaction.

1.4 Contents Of Thesis

Chapter 1: This chapter consists of the problem statement, conceptual overview of the study, objectives and contents of this thesis.

Chapter 2-3: Consist of papers submitted to journals, with the contents in verbatim.

Chapter 2: This chapter presents a proposed model for estimating the mechanical behavior of unsaturated soils, specifically focusing on small-strain shear modulus and shear

strength, based on the inverse relationship with the soil-water characteristic curve described by a scaling function. The proposed model relies on saturated mechanical behavior and scaling function. The saturated small-strain shear modulus can be laborious and expensive to determine. To address this, the Hardin and Black (1969) equation was modified by calibrating the material constant using data from literature soils to make it applicable across varying soil types. Furthermore, empirical relationships were established to facilitate the estimation of the scaling function. This paper has been submitted for publication to the Canadian Geotechnical Journal.

Acheampong L., and Bryson, L. S. 2023. Development of a Scaling Function to Estimate Unsaturated Mechanical Soil Behavior from a Soil-Water Characteristic Curve. Canadian Geotechnical Journal [SUBMITTED].

Chapter 3: This chapter presents the modification of the proposed model for estimating small-strain shear modulus under large-scale soil and field conditions. The proposed model initially developed from small laboratory samples were tested on two soils compacted in a large-scale test box fitted with sensors and accelerometers to measure moisture content and seismic data. Correlations were established to facilitate modification to the model derived from small laboratory samples. Subsequently, the modified model was applied to a field site, utilizing measured shear wave velocities and electrical resistivity measurements, along with soil-water characteristic curve data derived from pedotransfer transfer functions and the Archie (1942) equation. This paper has been submitted for publication to the Journal of Applied Geophysics.

Acheampong L., and Bryson, L. S. 2024. Estimation of Unsaturated Small-Strain Shear Modulus in a Large-Scale Test Box and Field Site from a Soil-Water Characteristic Curve. Journal of Applied Geophysics [SUBMITTED].

Chapter 4: This chapter summarizes the findings and conclusions of the research presented in Chapters 2 and 3.

Appendix A presents the index test results for laboratory test soils including specific gravity, Atterberg limits, proctor compaction, California bearing ratio, electrical measurements.

Appendix B presents the steps followed for the triaxial testing.

Appendix C presents the test results for consolidated drained and consolidated undrained triaxial tests and shear wave velocity from bender elements.

Appendix D presents the Microsoft PowerShell algorithm used in automating the bender elements testing.

Appendix E presents the MATLAB code for picking wave arrival times.

Appendix F presents the interface and data input for Rosetta.

CHAPTER 2. DEVELOPMENT OF A SCALING FUNCTION TO ESTIMATE UNSATURATED MECHANICAL SOIL BEHAVIOR FROM A SOIL-WATER CHARACTERISTIC CURVE

2.1 Introduction

The small-strain shear modulus and shear strength are mechanical properties important in the design of geotechnical structures like dams, embankments, pavement substructures, and retaining walls. These mechanical properties also play a pivotal role in the analyses of soil-structure interactions, slope stability, bearing capacity, and soil erosion problems (Dong et al., 2018; Ikechukwu et al., 2021). The soil beneath the groundwater table is typically considered saturated, whereas the soil above the groundwater table is considered to be partially saturated. There is a strong interest in assessing how partially saturated conditions affect the mechanical properties of soils. This is particularly significant since the stress distributions induced by the loads from various infrastructure systems are typically above the groundwater table, sometimes for the entire operational lifespan of the constructed facilities.

Therefore, it is imperative to account for soil responses to negative porewater pressures when evaluating the small-strain shear modulus and shear strength of the soil under partially saturated conditions. The negative porewater pressure is characterized by matric suction. The matric suction is defined as the difference between the pore air pressure, u_a , and pore water pressure, u_w . Matric suction exerts forces on the air-water interface, subsequently influencing the movement of soil particles. Consequently, alterations in matric suction lead to shifts in the stress state of the soil, ultimately impacting the mechanical response of partially saturated soils (Ngoc et al., 2020). The small-strain shear modulus defined by Atkinson and Salfors (1991) as the shear modulus of soils at strain amplitudes less than 1%, and the shear strength, which describes the deformability of a soil, are two mechanical behaviors that can be influenced by matric suction (Zhang and Lu, 2019; Mahmoodabadi and Bryson, 2021a).

Several experimental studies have shown that the small-strain shear modulus (Ng and Yung, 2008; Oh et al., 2009; Lu and Kaya, 2014; Morales et al., 2015; Khosravi et al., 2018a; Ngoc et al., 2019) and shear strength (Escario and Sáez, 1986; Vanapalli et al.,

1996; Cunningham et al., 2003; Sivakumar et al., 2013) vary nonlinearly with increasing matric suction. This observed trend can be attributed to the variability in capillary water content along with the associated capillary forces and weak physicochemical forces such as Van der Waals attraction (Lu and Likos, 2006; Ngoc et al., 2019). Capillary forces are usually considered as complex functions of grain size distribution, matric suction, degree of saturation, and the contact angle of soil grains. In contrast, Van der Waal attractions in the soil arise from intermolecular forces between atoms of adjacent soil particles. These elements directly affect the constitutive stress within the soil skeleton, consequently influencing the mechanical behavior of the soil (Lu and Likos, 2006; Han and Vanapalli, 2016).

The soil-water characteristic curve (SWCC), which describes the behavior of soil moisture with increasing matric suction has been incorporated in analyzing the hydro-mechanical behavior of unsaturated soils (Han and Vanapalli, 2016; Crawford et al., 2019; Ng and Peprah-Manu, 2023). This has led to concerted efforts to derive estimations of small-strain shear modulus and shear strength based on their relationship with the SWCC. However, few models (Han and Vanapalli, 2016; Mahmoodabadi and Bryson, 2021a; Tran et al., 2023) exist that can be used to predict both the small-strain shear modulus and shear strength based directly on the SWCC. Mahmoodabadi and Bryson (2021a) presented an approach that allowed for the estimation of the small-strain shear modulus over a wide range of matric suction and net normal stresses based on the SWCC. The approach is effective but requires a modification of the SWCC through optimization based on the assumption that the air-entry point, which is the breakpoint between the saturation phase (i.e., boundary zone) and the dewatering phase (i.e., transition zone) of the SWCC, does not directly mirror the breakpoint of the normalized shear modulus data. The breakpoint of the normalized shear modulus data was defined as the intersection point of the tangency line drawn through transition zone and the boundary zone for the shear modulus data.

This study presents a more simplistic predictive approach than the Mahmoodabadi and Bryson (2021a) model. The proposed model predicts the small-strain shear modulus and shear strength of unsaturated soils based on a direct relationship between the SWCC and the mechanical behavior of unsaturated soils. The proposed model provides

preliminary guidance in estimating small-strain shear modulus and shear strength behavior in soils under partially saturated conditions, under various stress states and moisture states.

2.2 State of Small-Strain Shear Modulus and Shear Strength Equations for Unsaturated Soils

Several deterministic models exist to estimate the small-strain shear modulus and shear strength of unsaturated soils. These models typically consist of a saturated mechanical property component and a component that varies with respect to the matric suction. The deterministic models for small-strain shear modulus can be divided into three groups; (a) equations in the “Hardin-style” family which are influenced by the overconsolidation ratio, void ratio, effective normal stress, and parameters changing with respect to matric suction (Sawangsurriya et al., 2009; Xu and Zhou, 2016; Ngoc et al., 2019; Zhang et al., 2021); (b) equations that are semi-empirical (Ng and Yung, 2008; Oh and Vanapalli, 2014; Xu and Zhou, 2016; Taukoor et al., 2019; Yan et al., 2022); and (c) equations that depend directly on the relationship between the small-strain modulus and the SWCC (Han and Vanapalli, 2016; Ngoc et al., 2020; Mahmoodabadi and Bryson, 2021a).

The deterministic models for shear strength can also be divided into two groups; (a) estimation-type equations (Vanapalli et al., 1996; Zhou et al., 2016; Naghadeh and Toker, 2019; Pham and Sutman, 2023); (b) fitting-type equations (Lee et al., 2005; Han and Vanapalli, 2016; Zhai et al., 2019; Gao et al., 2020). The estimation-type equations generally do not require measured unsaturated data for the prediction of unsaturated shear strength. However, they are linked to external parameters that can be either a material property or stress state condition. On the other hand, the fitting-type equations require some measured unsaturated data to make predictions across a range of suction.

Currently, the mathematical models used to estimate the small-strain shear modulus and shear strength of unsaturated soils differ due to variations in the testing procedures for these two mechanical properties. However, the influence of matric suction on these two mechanical behaviors are similar making it feasible and beneficial to employ a unified mathematical framework to describe both the small-strain shear modulus and shear strength

(Han and Vanapalli, 2016). The development of models to estimate these geomechanical properties under varying matric suction and net normal stress reduces the extensive and resource-intensive testing required.

The primary objective of this study was to develop a model that predicts both the small-strain shear modulus and shear strength of unsaturated soils based on the SWCC, which would not require any modification of the SWCC or extra fitting parameters. The proposed model for estimating mechanical property of partially saturated soils was correlated to a characteristic of the SWCC to develop empirical relationships for guidance in the absence of measured unsaturated mechanical property data. The influence of the drying and wetting paths, defined as hysteresis, on the proposed model was investigated. Recommendations were provided on how to apply the model under such conditions, which becomes crucial due to seasonal variations in field conditions that correspond to climate events.

The proposed model provided good predictions at a wide range of net normal stress and matric suction up to the residual zone of the SWCC. An additional contribution of this study was to calibrate the material constant of the Hardin and Black (1969) equation which can be used as a preliminary guide in the absence of measured saturated data for various soil types. This is important because having a single material constant that accommodates various soil types improves its usefulness across a broad spectrum of soil textures.

2.3 Development of Proposed Approach for Mechanical Behavior for Unsaturated Soils

2.3.1 Soil-Water Characteristic Curve

As discussed previously, the SWCC is critical in understanding and predicting the behavior of unsaturated soils. To define the SWCC, hydrologic models have been developed to estimate the water content-matric potential relationship. The van Genuchten (1980) model described in Eq. (2-1) was used in this study as, it is a robust model that is well-suited across the range of soil textures (Mahmoodabadi and Bryson, 2021a).

$$S_e = \left(\frac{\theta - \theta_r}{\theta_s - \theta_r} \right) = \left[1 + \left(\frac{\psi}{a} \right)^n \right]^{-m} \quad (2-1)$$

where S_e is the effective degree of saturation; ψ is matric suction; θ is the volumetric water content; θ_s is the saturated volumetric water content; θ_r is the residual volumetric water content; a is the curve fitting parameter related to the air entry value, with the version shown in this equation gives the units in kPa; n is related to the water extraction beyond the air-entry value and is usually related to the pore-size distribution; and m is a function related to the residual matric suction. The fitting parameters were determined by minimizing the least square difference between measured and predicted values using the Microsoft Excel Equation Solver. The fitting parameters are non-unique in the sense that they can differ significantly depending on the initial input data and boundary conditions used in the optimization process (Fredlund, 2019).

The SWCC is represented by three distinct regions: boundary, transition, and residual zones for laboratory description as illustrated in Figure 2-1. These zones are separated by the air-entry value (AEV) and residual value. The AEV signifies the matric suction level at which the desaturation of large pores begins, allowing air to permeate the pore spaces of the soil. The residual value marks the point beyond which soil water desaturation becomes minimal and sporadic as shown by the flattening of the SWCC. Consequently, the influence of soil suction on mechanical behavior diminishes at the residual state (Schnellmann et al., 2015; Han and Vanapalli, 2016). For cohesive soils, capillary effects and soil suction govern mechanical behavior, causing variation across a large range of suction. However, for cohesionless soils, the influence of suction and physicochemical inter-particle forces wane, leading to a decrease in small-strain shear modulus and shear strength in the residual zone (Oh et al., 2009; Ghayoomi and McCartney, 2011).

Several researchers (Ahmad-Adli et al., 2014; Song and Hong, 2020) have illustrated the influence of grain-size distribution on the AEV. Their findings show that soils with higher fines content have a higher AEV than those that are coarse-grained. This can be explained by the rate of saturation, which tends to be faster for coarse-grained soils

such as sands, and extremely slow for soils with high fines content such as silts and clays. Given the challenges in distinguishing between the behaviors of cohesive and cohesionless soils beyond the transition or across a wide range of suction values beyond the residual point, the air-entry value serves as a consistent delineator for both types of soils.

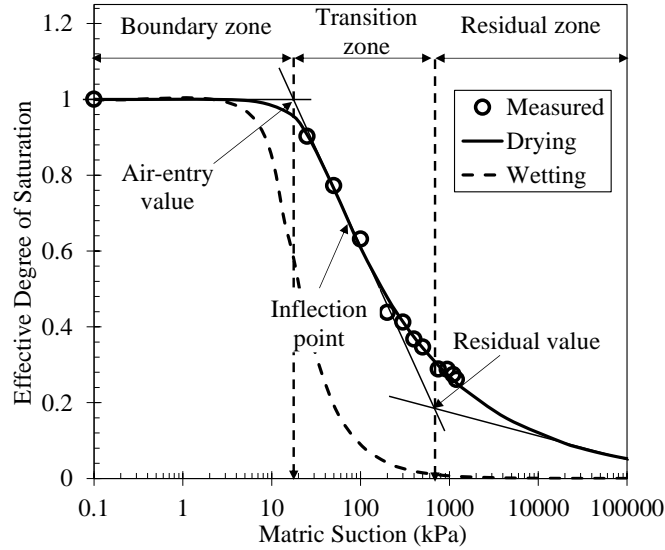


Figure 2-1 Soil-water characteristic curve showing the various zones and associated variables.

2.3.1.1 Considerations for Hysteresis

Hysteretic effects result in unequal moisture values at a common matric suction for the desorption (drying) and adsorption (wetting) paths. It is crucial to recognize the relevance of the drying or wetting SWCC in a given scenario, depending on the presence of significant seasonal variations (Mahmoodabadi and Bryson, 2021b). Given that laboratory measurements typically focus on drying SWCCs, wetting SWCCs can be estimated by adjusting the fitting parameters of the SWCC for the drying path (Pham et al., 2002; Fredlund et al., 2011; Zhou et al., 2012). In this study, wetting curves were obtained for some study soils using a modified van Genuchten (1980) model with multiplication factors presented by Ahmed et al. (2021) shown in Eq. (2-2).

$$S_e = \left[1 + \left(\frac{f_1 \psi}{\alpha} \right)^{f_2 n} \right]^{-f_3 m} \quad (2-2)$$

where f_1 , f_2 , and f_3 are the multiplication factors taken to be 2.2, 1.2, and 2.6 respectively.

Typically, soils on the drying path exhibit a higher shear strength compared to those on the wetting path when placed under the same matric suctions (Han et al., 1995; Rahardjo et al., 2004; Thu et al., 2006; Guan et al., 2010). This phenomenon can be explained by considering that interparticle forces rely on the contact area within soil particles and matric suction. Thus, as matric suction increases, soil in the wetting path (higher water content) will exhibit a reduced contact area between the water and soil particles. This leads to a reduced interparticle force during wetting path compared to drying path to resist deformation.

In contrast, the drying path exhibits a lower small-strain shear modulus than the wetting path for silts and clays as shown by several researchers (Ng et al., 2009; Khosravi and McCartney, 2012; Shi et al., 2022). This behavior can also be ascribed to the influence of matric suction and contact area on interparticle forces. During the wetting path, the contact area between particles is reduced, leading to a quicker travel path for shear wave velocity. The small-strain shear modulus is calculated from the shear wave velocity as shown in Eq. (2-3). Therefore, the modulus becomes higher for a wetting path compared to that of a drying path for soils placed in at the same density.

$$G = \rho \cdot V_s^2 \quad (2-3)$$

where ρ is the bulk mass density; and V_s is the shear wave velocity.

However, sands exhibit a different trend with higher values observed along the drying path as opposed to the wetting paths (Khosravi et al., 2018b). Therefore, it is important to understand the influence soil type when estimating small-strain shear modulus for drying and wetting path.

2.3.1.2 Mathematical Determination of the Air-Entry Value

The determination of the AEV is commonly achieved through graphical construction as illustrated in Figure 2-1. However, a more precise and efficient approach involves numerical determination, which eliminates any potential ambiguity characteristic of visual

identification. Moreover, a numerical approach addresses the non-uniqueness inherent in these fitting parameters for hydrologic models, wherein various combinations of fitting parameters can yield the same AEV for the soil. In this study, the AEV for the soils were determined using the mathematical approach presented by Soltani et al. (2021), following the three-step process as outlined below:

- a) The inflection point matric suction, ψ_{inf} was determined by calculating the positive real root of the second derivative of the van Genuchten (1980) effective degree of saturation equation shown in Eq. (2-2) and is expressed as:

$$\frac{d^2 S_e}{d(\log \psi)^2} = \frac{2.3 \left[\left(\frac{\psi}{\alpha} \right)^n + 1 \right]^{-m} \cdot \left[m^2 \cdot n^2 \cdot \left(\frac{\psi}{\alpha} \right)^{2n} - m \cdot n^2 \cdot \left(\frac{\psi}{\alpha} \right)^n \right]}{\psi \cdot \left[\left(\frac{\psi}{\alpha} \right)^{2n} + 2 \left(\frac{\psi}{\alpha} \right)^n + 1 \right]} = 0 \xrightarrow{\text{Root}} \psi_{\text{inf}} \quad (2-4)$$

- b) The gradient of the tangent line at the saturation portion of the SWCC, Δ_{sat} , is subsequently approximated as:

$$\Delta_{\text{sat}} = \frac{dS_e}{d(\log \psi_{\text{inf}})} = -2.3 \cdot m \cdot n \cdot \left(\frac{\psi_{\text{inf}}}{\alpha} \right)^n \cdot \left[\left(\frac{\psi_{\text{inf}}}{\alpha} \right)^n + 1 \right]^{-m-1} \quad (2-5)$$

- c) The precise value of the AEV, ψ_{aev} , is then determined from the intersection point by calculating the inverse logarithm given as:

$$\psi_{\text{aev}} = \exp \left(\log \psi_{\text{inf}} + \frac{1 - S_{e\text{inf}}}{\Delta_{\text{sat}}} \right) \quad (2-6)$$

where $S_{e\text{inf}}$ is the effective degree of saturation at the inflection point.

The AEV, as determined through the effective degree of saturation method (S -SWCC) described above provides a good representation of the “true” AEV for the soil. This is because the S -SWCC remains constant and equal to unity while the soil is fully saturated and does not reflect any volume change (Fredlund, 2019). This is why the initial

line from the saturated unity point within the boundary zone is always drawn horizontally as shown in Figure 2-1.

2.3.2 Suction-Mechanical Relationship of Unsaturated Soils

Several studies (Khosravi et al., 2010; Dong et al., 2016; Han and Vanapalli, 2016; Xu and Zhou, 2016) have shown that the small-strain shear modulus and shear strength with increasing matric suction trends inversely with the SWCC. This relationship is shown in Figure 2-2 using literature soils. The soils are Bonny silt reported by Khosravi et al. (2018a) and Air-dry silty clay as reported by Cunningham et al. (2003). In the figure, the small-strain shear modulus and shear strength of the soils before the AEV exhibits a linear trend, which represents the boundary zone of the SWCC. At the AEV, there is a bend from the linear regime, which progresses into a nonlinear regime within the transition zone of the SWCC. The linear regime represents the soil in saturated conditions since there are no air bubbles in the soil but as it transitions past the AEV, the soil becomes unsaturated and that results in the characteristic nonlinear trend of soil mechanical behavior. The slope of the SWCC can therefore be mirrored onto the mechanical behavior using a negative scaling function.

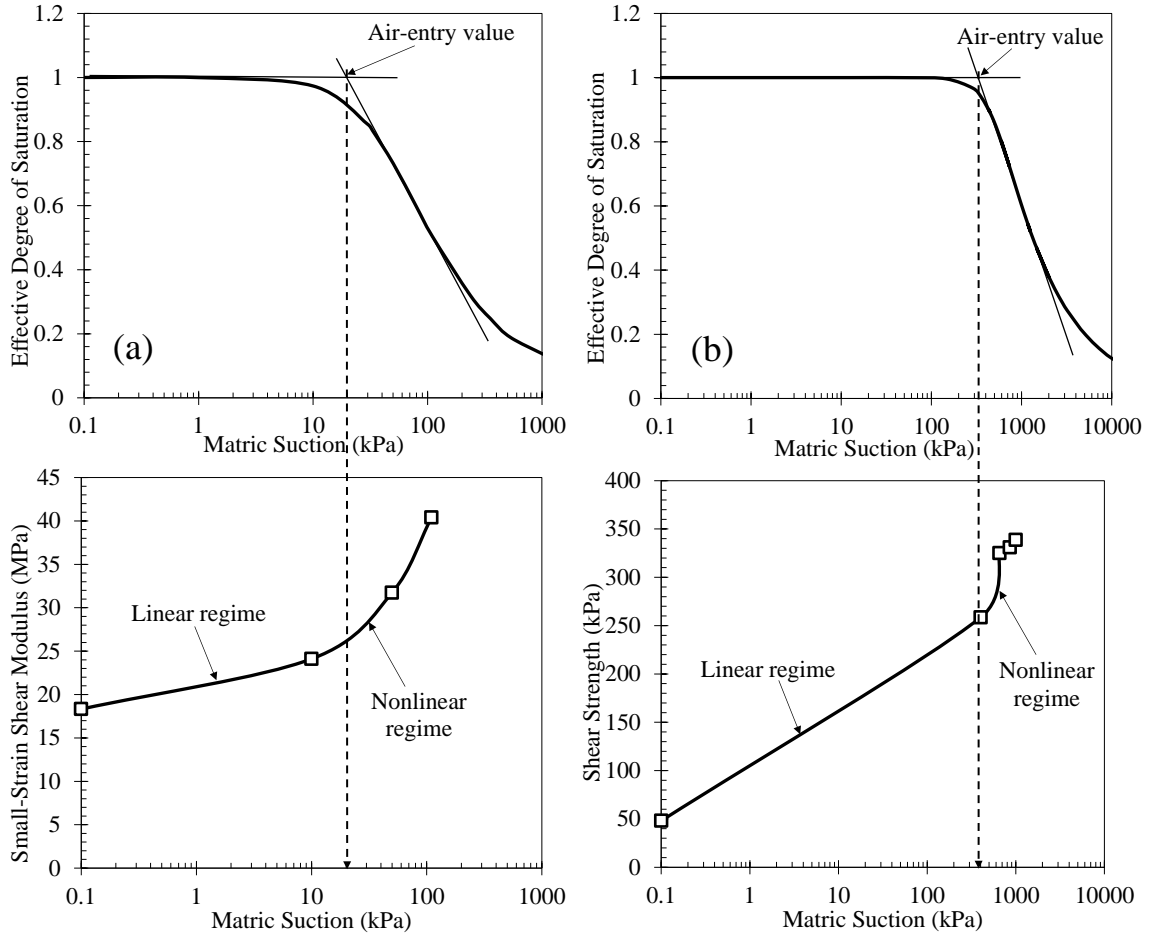


Figure 2-2 Graphical representation of the relationship between the SWCC and mechanical behavior with respect to increasing matric suction; (a) Bonny silt at 40 kPa (data from Khosravi et al., 2018a); and (b) Air-dry silty clay at 200 kPa (data from Cunningham et al., 2003)

The relationship between mechanical behavior and the SWCC can be expressed mathematically as:

$$\frac{dU}{d\psi} \propto -\frac{dS_e}{d\psi} \quad (2-7)$$

where U represents the mechanical behavior of unsaturated soils. i.e., in this study the small-strain shear modulus and shear strength.

Eq. (2-7) can be rewritten by introducing a constant as:

$$\frac{dU}{d\psi} = -\beta \frac{dS_e}{d\psi} \quad (2-8)$$

where β is defined as the scaling function that defines the negative slope between the SWCC and the mechanical behavior of unsaturated soils with increasing matric suction. Therefore, with information on β , it becomes possible to align the SWCC onto mechanical behavior of partially saturated soils.

Separating the variables and integrating them with respect to matric suction yields:

$$U(\psi) - U_0 = - \int_{\psi_0}^{\psi} \beta \left(\frac{dS_e}{d\psi} \right) d\psi \quad (2-9)$$

where $U(\psi)$ and U_0 are the mechanical behavior at various matric suctions and initial conditions, respectively; ψ_0 and ψ are the initial and subsequent matric suctions corresponding with the effective degree of saturation, respectively.

The integration of Eq. (2-9) results in the closed form equation which will be referred to as the general form equation for unsaturated soil mechanical behavior given as:

$$U(\psi) - U_0 = -\beta [S_e(\psi) - S_e(\psi_0)] \quad (2-10)$$

where $S_e(\psi)$ is the effective degree of saturation at a given matric suction and is given from Eq. (2-1) and Eq. (2-2) for both drying and wetting paths, respectively. Because the initial effective degree of saturation at the saturated point, $S_e(\psi_0)$ is 1, Eq. (2-10) will simplify to Eq. (2-11) presented as:

$$U(\psi) - U_0 = -\beta [S_e(\psi) - 1] \quad (2-11)$$

Eq. (2-11) is intended to provide a prediction of mechanical behavior with respect to matric suction based on the proportional inverse relationship of the SWCC and known initial saturated small-strain shear modulus and shear strength.

2.3.3 Study Soils

Thirteen literature soils were utilized to assess the performance of the proposed model at predicting the small-strain shear modulus experimental data. The soils with their references, soil classification, geotechnical index properties (plasticity and specific

gravity) and testing techniques are presented in Table 2-1. The soils were selected to cover a wide range of soils ranging from fine grained (silts and clays) to coarse grained (sands), and low plasticity (liquid limit less than 50) to high plasticity (liquid limit greater than 50).

The initial saturated and single unsaturated small-strain shear modulus points can be determined using bender elements (Wang et al., 2021) and resonant columns (Yan et al., 2023). Hoyos et al. (2015) performed a simultaneous series of suction-controlled resonant column and bender elements tests to compare the small-strain shear modulus obtained using these approaches. It was concluded from the study that the shear modulus obtained from resonant column testing yielded reasonably close results to those obtained from the bender elements technique. Therefore, it becomes imperative to use data from both testing techniques in the development of the proposed model for small-strain shear modulus.

Table 2-1 Geotechnical index properties of soils used to evaluate the performance of the proposed equation for small-strain shear modulus.

Reference	Soil name	USCS	S_G	LL (%)	PI (%)	Method
Takkabutr (2006)	Ottawa Sand	SP	2.65	N/A	N/A	RC
	Arlington Clay	CH	2.75	62	37	
Ng and Yung (2008)	Completely Decomposed Tuff	ML	2.73	43	14	BE
Khosravi et al. (2010)	F-75 Quartz Sand	SW	2.65	N/A	N/A	RC
Sawangsurriya et al. (2009)	Anaheim Clayey Sand	SC	2.70	28	14	BE
	Anaheim Clayey Silt	ML	2.69	28	11	
	Mn Road Clay	CL	2.66	26	9	
	Red Lake Falls Clay	CL	2.69	42	24	
	D1 TH23 Slopes Clay	CH	2.75	85	52	
Mancuso et al. (2002)	Metramo Silty Sand	SM	2.64	35.4	13.7	RC
Khosravi et al. (2018a)	Bonny Silt-1 ^a	ML	2.6	25	4	BE
Khosravi and McCartney (2012)	Bonny Silt-2 ^a	ML	2.6	25	4	BE
Mendoza et al. (2005)	Kaolin S5	MH	2.61	80	35	BE
Hippley (2003)	Rock Flour	ML	2.68	N/A	N/A	RC

Note: USCS = Unified Soil Classification System; S_G = specific gravity; PI = plasticity index; LL = liquid limit; Fines and Clay = Percentage of fines (silts and clays) and clay per total weight of the soil sample respectively; a = same soil but tested under different net normal stresses and initial dry densities; RC = Resonant Column and BE = Bender Elements.

Table 2-2 presents the fitting parameters for the van Genuchten (1980) equation (v_G), AEVs and β values obtained from measured data along with the coefficients of

determination, R^2 , between measured and predicted data for the soils sourced from literature. The analysis for the R^2 values will be discussed in subsequent sections. The study soils were classified into three distinct groups; (1) soils for which small-strain shear modulus measurements were obtained using bender elements; (2) soils for which the small-strain shear modulus measurements were acquired through resonant column testing; and (3) soils for which the small-strain shear modulus measurements were obtained using resonant column testing but were also employed to evaluate the performance of the scaling function under hysteretic effects.

Table 2-2 SWCC fitting parameters for the study soils used for evaluating the performance of the proposed equation for small-strain shear modulus.

Group #	Soil Name	$(\sigma - u_a)$ (kPa)	vG model parameters			Eq. (2-6)	R^2		
			α (kPa)	n	m	AEV (kPa)		β (kPa)	
Group #1	Completely Decomposed Tuff	110	47.87	2.19	0.13	31.91	235.67	0.83	
		200	47.87	2.19	0.13	31.91	237.75	0.80	
		300	47.87	2.19	0.13	31.91	212.77	0.83	
		400	47.87	2.19	0.13	31.91	158.47	0.85	
		Anaheim Clayey Sand	35	286.81	0.79	0.49	43.24	506.88	0.99
		Anaheim Clayey Silt	35	23.22	1.27	0.23	10.20	184.93	0.77
		Mn Road Clay	35	499.63	0.84	0.40	98.27	494.73	1.00
		Red Lake Falls Clay	35	596.38	0.85	0.42	116.68	804.98	0.95
		D1 TH23 Slopes Clay	35	1961.53	0.79	0.67	225.22	360.38	0.94
		Bonny Silt-1	40	42.47	1.78	0.37	20.37	46.17	0.96
	600		59.24	1.94	0.43	28.57	106.93	0.98	
	900		65.05	2.37	0.41	36.38	191.66	0.98	
		Kaolin S5	0.1	2396.58	1.60	0.50	933.98	206.47	0.95
	Group #2	Ottawa Sand	0.1	42.57	2.90	0.49	25.55	49.48	0.97
6.8			42.57	2.90	0.49	25.55	57.57	0.98	
17.25			42.57	2.90	0.49	25.55	80.58	0.97	
34.45			42.57	2.90	0.49	25.55	111.46	0.89	
		Arlington Clay	0.1	1038.63	1.30	0.46	340.44	223.32	0.82
6.8			1038.63	1.30	0.46	340.44	224.62	0.80	
17.25			1038.63	1.30	0.46	340.44	239.82	0.82	
34.45			1038.63	1.30	0.46	340.44	248.85	0.88	
		F-75 Quartz Sand	3.5	2.41	39.98	0.06	2.38	5.08	0.91
12			2.85	45.05	0.07	2.82	7.04	0.86	

Group #3	Metramo Silty Sand	20	1.75	5.16	0.35	1.36	5.34	0.91
		100	47.45	4.65	0.82	31.89	162.65	0.73
		200	47.45	4.65	0.82	31.89	164.43	0.88
		400	47.45	4.65	0.82	31.89	193.15	0.75
	Rock Flour	0.69	3.03	1.40	0.26	1.37	80.40	0.78
		138	3.03	1.40	0.26	1.37	80.01	0.65
	Bonny Silt-2 ^d	100	27.78	5.00	0.80	19.25	7.44	0.92
		150	25.00	4.60	0.78	16.84	8.49	0.96
	Bonny Silt-2 ^w	200	25.00	4.60	0.78	16.84	7.65	0.92
		100	16.67	3.60	0.72	10.23	6.33	0.94
		150	14.29	3.50	0.71	8.66	4.20	0.93
		200	14.29	3.50	0.71	8.66	2.07	0.93

Note: superscripts d and w represent drying and wetting paths respectively; $(\sigma - u_a) =$ net normal stress

Shear strength parameters such as ϕ' and c' are often determined using triaxial and direct shear testing methods. Thus, literature soils taken to evaluate the performance of the proposed equation for estimating shear strength were selected to comprise soils tested using both methods. Table 2-3 provides the index soil properties, saturated shear strength parameters and testing methods for the study soils used to evaluate the performance of the proposed equation for shear strength.

Table 2-3 Geotechnical index properties of literature soils used to evaluate the performance of the proposed equation for shear strength.

Reference	Soil name	USCS	ϕ' (deg)	c' (kPa)	S_G	LL (%)	PI (%)	Method
Escario and Juca (1989)	Madrid Clayey Sand	CL	39.5	40	2.71	28	8	DS
	Guadalix Red Clay	CL	34	20	2.66	33	13.6	
	Madrid Grey Clay	CH	25.3	30	2.64	71	35	
Oloo and Fredlund (1996)	Botkin Pit Silt	ML	28	2.5	2.68	22	6	DS
Hamid and Miller (2009)	Minco Silt	CL	34.5	12	2.67	28	8	DS
Rassam and Williams (1999)	Mine Tailings-1	-	41.7	0	-	-	-	TX
	Mine Tailings-2	-	40.7	0	-	-	-	TX
Khalili et al. (2004)	SJ10A Hume Dam Clay	CL	29	5	-	39	18	
	SJ10B Hume Dam Clay	CL	29	19	-	33	21	

	SJ11 Hume Dam Clay	CL	30	5	-	25	19	
Cunningham et al. (2003)	Air-dry Silty Clay	ML	31	20	2.64	28	18	TX
Lee et al. (2005)	Weathered Granite	SM	41.4	19.3	2.65	NP	NP	TX
Thu et al. (2006)	Coarse Kaolin	MH	32	0	2.65	51.0	15.4	TX
Schnellmann et al. (2013)	Sand vom Stücken	SW-SM	33.6	0	2.72	NP	NP	TX
Miao et al. (2002)	Nanyang Expansive Clay	CH	21.3	32	2.70	58.3	31.8	TX
Han et al. (1995)	Granitic Residual Clay	CH	33	-	2.66	47	18	DS

Note: DS = Direct Shear and TX = Triaxial Test

Table 2-4 provides an overview of the net normal stresses, SWCC fitting parameters, and β values obtained from measured data, along with the R^2 values between measured and predicted data. The study classifies the soils into three groups; (1) soils for which shear strength parameters were obtained through direct shear testing, (2) soils for which shear strength parameters were obtained from triaxial testing; and (3) soils for which shear strength parameters were obtained from direct shear and were utilized to investigate hydraulic hysteresis on the scaling function.

Table 2-4 SWCC fitting parameters for the literature soils used for evaluating the performance of the proposed equation for shear strength.

Group #	Soil name	$(\sigma - u_a)$ (kPa)	vG model parameters			Eq. (2-6)		R^2
			α (kPa)	n	m	AEV (kPa)	β (kPa)	
Group #1	Madrid Clayey Sand	120	37.08	2.94	0.11	29.10	167.95	0.81
	Guadalix Red Clay	120	300	0.73	0.50	38.56	666.39	0.89
	Madrid Grey Clay	300	3200	0.57	0.85	119.87	636.55	0.94
	Botkin Pit Silt	50	34.16	8.62	0.02	32.997	105.09	0.95
		100	34.16	8.62	0.02	32.997	134.48	0.89
		150	34.16	8.62	0.02	32.997	156.36	0.95
	Minco Silt	0	64.31	2.01	0.43	31.87	121.86	0.90
		105	64.31	2.01	0.43	31.87	100.82	0.87
		155	64.31	2.01	0.43	31.87	122.13	0.96
210		64.31	2.01	0.43	31.87	140.02	0.88	
Group #2	Mine Tailings-50m	30	2.15	10.36	0.05	2.05	28.32	0.89
		125	2.15	10.36	0.05	2.05	38.45	0.86

		250	2.15	10.36	0.05	2.05	46.17	0.83
	Mine Tailings-150m	30	8.08	3.47	0.15	6.32	37.72	0.99
		125	8.08	3.47	0.15	6.32	66.16	0.93
		250	8.08	3.47	0.15	6.32	77.01	0.92
	SJ10A Hume Dam Clay	200	190	1.04	0.11	95.28	903.17	0.99
	SJ10B Hume Dam Clay	200	250	0.82	0.18	79.95	703.52	0.94
	SJ11 Hume Dam Clay	200	400	0.81	0.28	94.69	912.42	1.00
	Air-dry Silty Clay	0	494.69	3.26	3.26	362.74	937.87	0.76
		50	494.69	3.26	3.26	362.74	877.95	0.72
		100	494.69	3.26	3.26	362.74	968.51	0.76
		200	494.69	3.26	3.26	362.74	891.21	0.76
		400	494.69	3.26	3.26	362.74	855.22	0.68
	Weathered Granite	0.1	1.73	8.41	0.03	1.66	37.81	0.66
		100	4.48	7.75	0.04	4.26	50.25	0.76
		200	8.51	3.75	0.09	7.19	66.59	0.84
		300	14.19	3.03	0.11	11.16	81.87	0.90
	Coarse Kaolin	50	60.54	9.44	0.08	56.85	205.92	0.97
		100	60.54	9.44	0.08	56.85	217.09	0.93
		150	60.54	9.44	0.08	56.85	210.78	0.92
		200	60.54	9.44	0.08	56.85	224.40	0.95
		250	60.54	9.44	0.08	56.85	218.70	0.97
		300	60.54	9.44	0.08	56.85	236.02	0.96
	Sand vom Stücken	50	0.57	8.51	0.04	0.54	107.73	0.92
		230	0.57	8.51	0.04	0.54	134.09	0.94
		320	0.57	8.51	0.04	0.54	138.75	0.99
	Nanyang Expansive Clay	-	59.82	9.41	0.07	96.14	191.90	0.99
Group #3	Granitic Residual Clay ^d	200	64.27	0.70	0.30	11.68	1689.79	0.98
	Granitic Residual Clay ^w	200	6.29	1.11	0.09	3.54	1898.4	0.92

2.3.4 Methods for Obtaining the Scaling Function, β

A rigorous approach was initially employed to derive the scaling function, denoted as β in this study. This rigorous approach involved plotting a linear regression of Eq. (2-11) using measured data while setting the intercept to zero. The slope of line is β . This approach is illustrated in Figure 2-3 using two of the literature soils. In the figure, the mechanical properties are represented by G and τ , corresponding to the small-strain shear modulus and shear strength, respectively. When relating the equations in Figure 2-3 (a) and Figure 2-3 (b) to Eq. (2-11), it becomes evident that the obtained β values are approximately 494.73 MPa and 912.42 kPa for the small-strain shear modulus and shear

strength data, respectively. The units of β are dependent on the units of the saturated and unsaturated mechanical properties.

The β values presented in Table 2-2 and Table 2-4 were obtained using the rigorous approach. It is worth noting that an alternative approach for obtaining the β values involve employing a least squares optimization, which utilizes both measured and predicted values at common matric suctions. However, this approach was not adopted to minimize the complexity associated with optimizing β calibration.

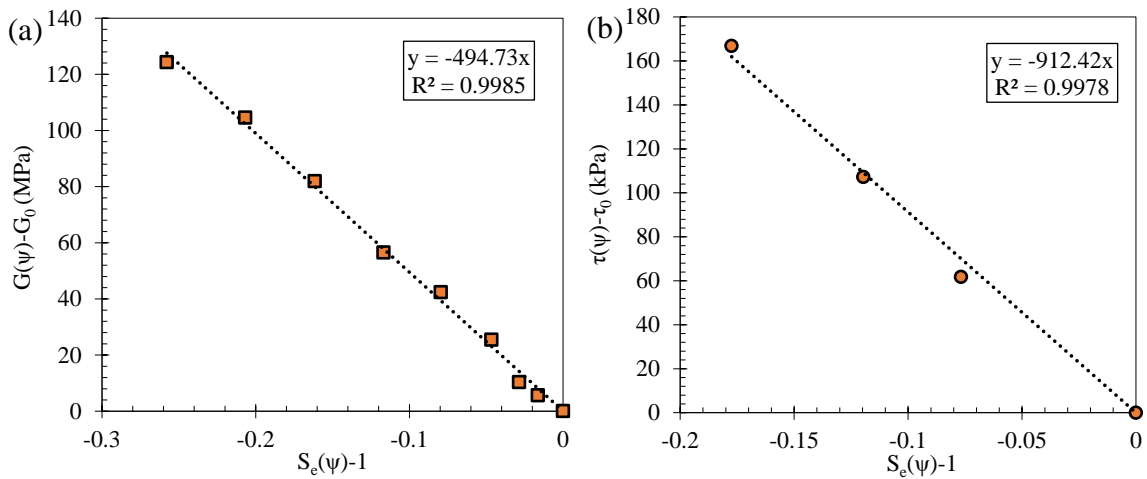


Figure 2-3 Values of β obtained from measured data for two literature soils (a) Small-strain shear modulus data for Mn Road Clay (data from Sawangsuriya et al., 2009) (b) Shear Strength data for SJ10 Hume Dam SB (data from Khalili et al., 2004).

As illustrated in Figure 2-3, the rigorous approach for getting β necessitates knowing at least one unsaturated data point since the relationship is a straight line that goes through the origin representing saturated conditions. From the analysis of the literature data, a simple unsaturated point to find is the small-strain shear modulus and shear strength at the AEV for the soil. The reason for this point is because the AEV is an integral anchor parameter of the SWCC used to characterize unsaturated soil properties. This is because it is at the AEV where soils transition into the unsaturated soil behavior with the presence of air bubbles. Figure 2-4 displays the normalized small-strain modulus data at AEV in relation to the saturated measured data, G_{aev}/G_0 as well as the normalized shear strength data at AEV with respect to the saturated measured data, τ_{aev}/τ_0 encompassing soil types outlined in Tables 2-1 and 2-3.

In Figure 2-4 (a), it is evident that, for silts to sandy silts, the normalized G_{aev}/G_0 data ranges from 1.0 to 1.4. An average value of 1.2 is recommended. For fine sands to sandy clays, the range extends from 1.0 to 1.8, with a suggested average value of 1.4. Notably, only a single data point was recorded for a fat clay at 2.3 and is recommended as the average value since it follows the increasing trend with respect to increasing behavior with increased AEV for all soil types. In Figure 2-4 (b), it is observed that the normalized τ_{aev}/τ_0 varies from 1.0 to 1.2 for sands to silts, with 1.1 suggested as an average value for practical use. For clayey silts to clays, the range falls between 1.0 to 1.7, with a recommended average value of 1.4.

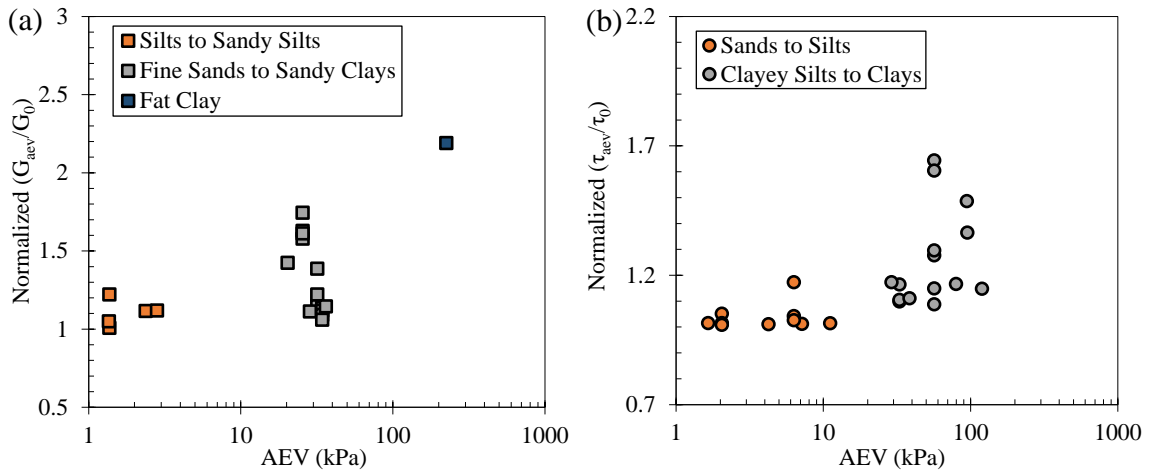


Figure 2-4 Variation of the normalized small-strain shear modulus and shear strength data at the AEV with respect to the saturated measured data for different soil types.

2.4 Proposed Approach for Unsaturated Small-Strain Shear Modulus

The proposed general form mechanical-suction relationship presented in Eq. (2-11) can be rewritten for the small-strain shear modulus as Eq. (2-12). This will be denoted as the G -suction equation hereon.

$$G(\psi) = G_0 - \beta [S_e(\psi) - 1] \quad (2-12)$$

where $G(\psi)$ is the unsaturated small-strain shear modulus at a given matric suction.

The predictive G -suction equation defines the small-strain shear modulus curve with respect to an initial measured saturated small-strain shear modulus, G_0 . As was discussed earlier, small-strain shear modulus data obtained from the bender elements technique and resonant column can be used together. However, it is still a limitation that these tests can be time consuming and expensive in obtaining an initial saturated small-strain shear modulus. Hardin and Black (1969) proposed an equation that can be used to estimate the saturated small-strain shear modulus with information on the void ratio, confining stress, and plasticity index. The equation is given as:

$$G_0 = Af(e)(OCR)^k (\bar{\sigma}'_0)^\zeta \quad (2-13)$$

where A represents a dimensionless material constant coefficient; $f(e)$ is a function related to the void ratio, e ; OCR denotes the overconsolidation ratio; k is an exponent specific to the overconsolidation ratio dependent on the plasticity index; $\bar{\sigma}'_0$ is the mean effective stress; and ζ is an exponent based on contact between particles and strain amplitude, typically assumed to be 0.5. The expression for the void ratio function is presented as:

$$f(e) = \frac{(2.973 - e)^2}{1 + e} \quad (2-14)$$

This study calibrated the A value for use across all soil types to allow for preliminary estimation of saturated small-strain shear modulus in the absence of measured data.

2.4.1 Calibration of the Material Constant for Hardin and Black (1969) Equation

In this study eight literature soils with measured saturated small-strain shear modulus were fit with a regression equation to calibrate for the material constant, A , in the Hardin and Black (1969) equation presented as Eq. (2-13). The soils are presented in Table 2-5 with information on the soil types, confining stresses, void ratios, measured small-strain shear modulus, and testing techniques. The soils were selected to cover a wide range of soil textures from coarse sands to fat clays.

Table 2-5 Properties of soils used for calibrating the material constant for the Hardin and Black (1969) Equation.

Reference	Soil name	USCS	$\bar{\sigma}'_0$ (kPa)	e	$f(e)$	G_0 (MPa)	Method
Takkabutr (2006)	Ottawa Sand	SP	0.1	0.46	4.35	15.53	RC
Khosravi et al. (2010)	F-75 Quartz Sand	SW	20	0.58	3.63	34.92	RC
Mancuso et al. (2002)	Metramo Silty Sand	SM	100	0.35	5.12	129	RC
Hippley (2003)	Rock Flour	ML	0.69	0.68	3.14	2.52	RC
Ng and Yung (2008)	Completely Decomposed Tuff	ML	400	0.48	4.18	327.8	BE
Khosravi et al. (2018a)	Bonny Silt-1	ML	40	0.85	2.45	18.31	BE
Sawangsurriya et al. (2009)	D1 TH23 Slopes Clay	CH	35	1.15	1.54	27.19	BE
Kidd (2011)	Lee County Clay	CH	7	0.65	3.29	55.82	BE

The variation of $G_0/f(e)$ with respect to $(\bar{\sigma}')^{0.5}$ was plotted as illustrated in Figure 2-5. A linear best-fit relationship was established, and from the plotted data, $A = 3419.4$, which is the average slope of all the data points, was determined. Using this value of A back in Eq. (2-13) gives:

$$G_0 = 3419.4 \cdot f(e)(OCR)^k (\bar{\sigma}')^{0.5} \quad (2-15)$$

Eq. (2-15) gives as the calibrated Hardin and Black (1969) equation, proposed for estimating the initial saturated small-shear modulus when actual measured data is unavailable. It is imperative to approach the application of the calibrated material constant, A , with careful consideration and engineering judgment recognizing the possibility of both under-predictions and over-predictions, depending on the normal stress placed on the soil as shown in Figure 2-5.

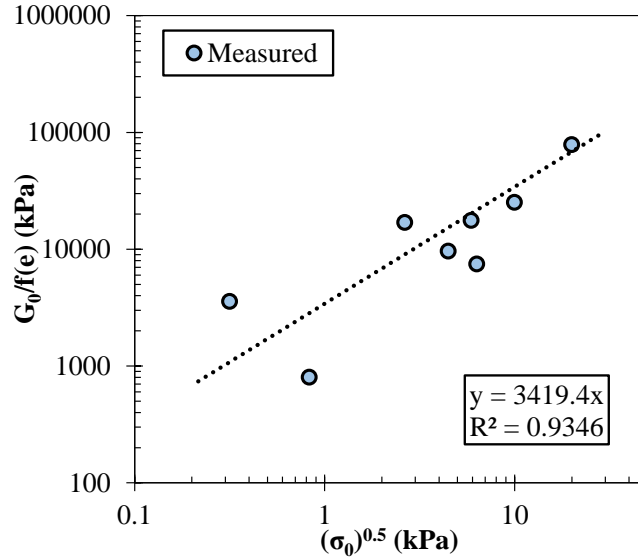


Figure 2-5 Calibration of material constant, A using literature soils.

2.4.2 Performance of the G-suction Equation

Figure 2-6 shows the measured and predicted small-strain shear modulus using the proposed G -suction equation. The predictive performance demonstrates a linear increase in the small-strain shear modulus as matric suction increases up to the AEV and subsequent nonlinear trend for all the soils. Notably, this trend remains consistent regardless of soil type, applied net normal stress, and testing technique. Figures 2-6 (c) and 2-6 (d) present the prediction model for two silts, Completely Decomposed Tuff and Bonny Silt-1, each subjected to varying net normal stresses and tested using a resonant column and bender element, respectively.

It is worth noting that Figure 2-6 (c) provides some insight into the reason behind the relatively minimal correlation coefficients reported in Table 2-2 for Completely Decomposed Tuff, ranging from 0.80 to 0.85. As previously discussed, the proposed model does not account for a decrease in small-strain shear modulus beyond the transition zone, especially as it approaches the residual zone. Consequently, among the various soils examined in Table 2 to evaluate the G -suction equation, those demonstrating a subsequent drop beyond the transition zone, such as Arlington Clay, Metramo Silty Sand, and Rock Flour exhibit minimal R^2 values. Here minimal R^2 values were considered as those between 0.6 and 0.9.

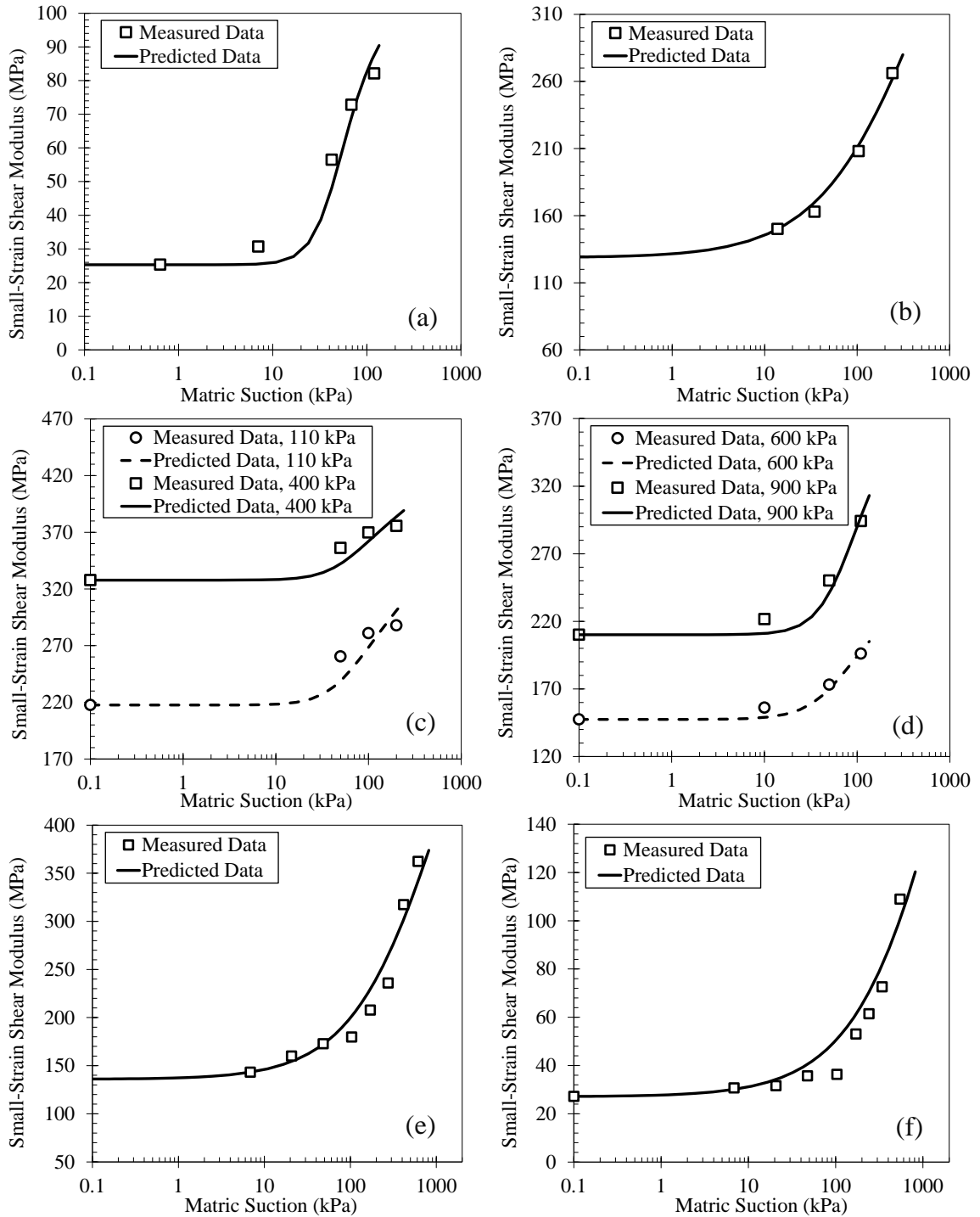


Figure 2-6 Measured and predicted small-strain shear modulus for six literature soils: (a) Ottawa Sand at 17.25 kPa; (b) Anaheim Clayey Sand at 35 kPa; (c) Completely Decomposed Tuff; (d) Bonny Silt-1; (e) Red Lake Falls at 35 kPa; (f) DI TH23 Slopes Clay at 35 kPa.

2.4.3 Performance of the Proposed G-suction Equation under Hydraulic Hysteresis Effects

The study investigated the effects of hysteresis on the scaling parameter utilizing the Bonny Silt-2, subjected to three distinct net normal stresses (i.e., 100 kPa, 150 kPa, and 200 kPa). SWCCs were acquired at these net normal stresses for both drying and wetting paths, continuing until it approached the residual suction value approximately 100 kPa. Figure 2-7 shows that the drying path small-strain shear modulus is less than that of the wetting path, as discussed earlier. The trend of the G -suction prediction for the wetting path follows the same as that for drying path, which increases linearly up to the AEV which were 10.23 kPa, 8.66 kPa and 8.66 kPa for the net normal stresses of 100 kPa, 150 kPa and 200 kPa, respectively. The path then progresses nonlinearly until the residual suction.

Since the AEV is smaller for the wetting path and to mirror the SWCC onto the small-strain shear modulus behavior, which is higher than the drying path, it would require a smaller β to exactly mirror the behavior onto the drying path SWCC. The reported β values for the wetting path are 6.33 MPa, 4.20 MPa, and 2.07 MPa, and for the drying path were 7.44 MPa, 8.49 MPa, and 7.65 MPa for the net normal stresses of 100 kPa, 150 kPa and 200 kPa, respectively. The β value for a wetting path in the absence of a wetting SWCC, can be determined by first estimating the wetting path SWCC (as per Eq. 2-2) and then applying Eq. (2-12).

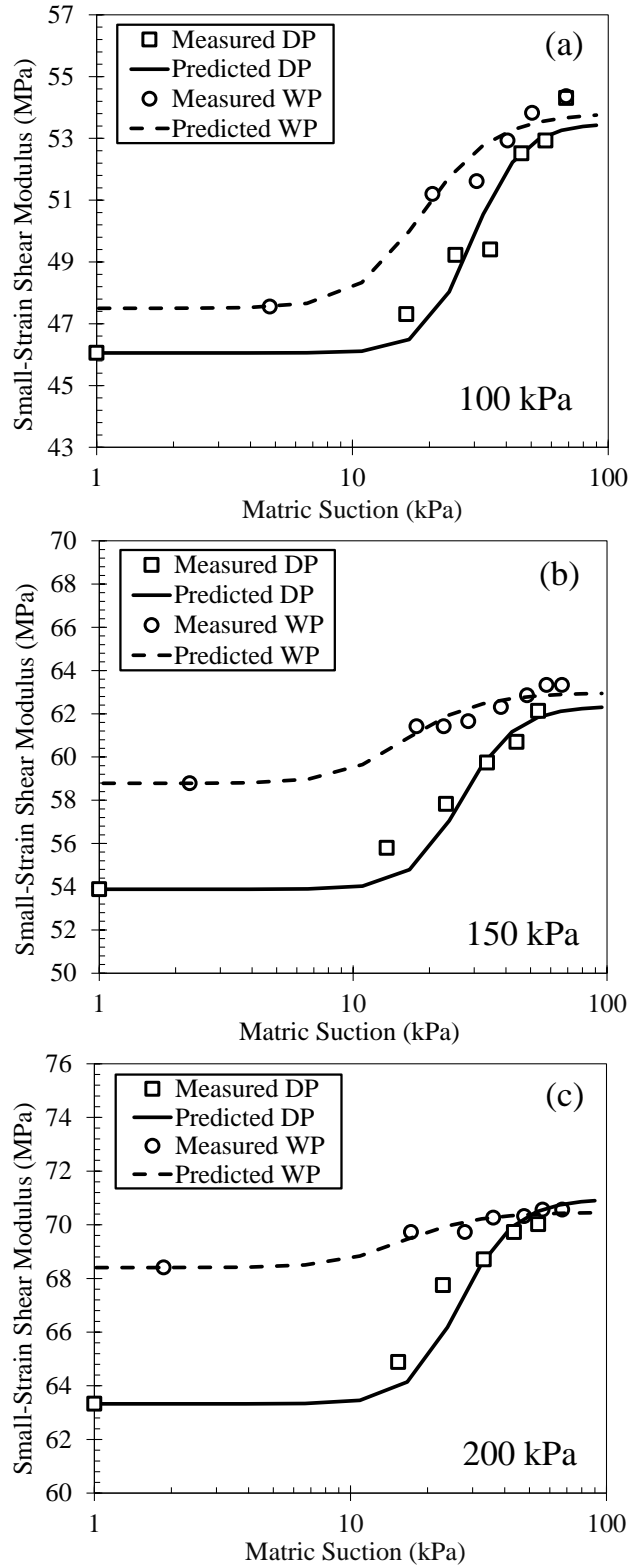


Figure 2-7 Performance of G-suction under hydraulic hysteric effects and under different net normal stresses. In the figure, DP=Drying Path; WP=Wetting Path.

2.4.4 Proposed Empirical Relationship for β for G -suction

As discussed earlier, the scaling function, β , serves as the negative slope to mirror the SWCC onto the mechanical behavior. Thus, the β for the G -suction curve must correlate with parameters or variables of the SWCC. However, the fitting parameters obtained from the van Genuchten (1980) model are non-unique depending on the optimization technique, this non-uniqueness introduce ambiguity when developing a correlation based on the SWCC fitting parameters. The air-entry value marks the boundary between the saturated and unsaturated mechanical behavior of soils, which renders it crucial in predicting unsaturated soil properties (Wang et al., 2020; Soltani et al., 2021). Thus, the scaling function can be justified to correlate with the air-entry value since the negative slope is reflective of this break point.

To provide guidance in the application of the G -suction equation outlined in Eq. (2-12) in the absence of experimental data, Figure 2-8 illustrates the variation of β with respect to the AEV for the soils under study. As shown in Figure 2-8 (a), β demonstrates a significant increase for AEVs below 100 kPa, characteristic of sands, lean silts, and lean clays. In contrast, AEVs equal to or greater than 100 kPa, which align with fat silts and fat clays, exhibit a significant decrease as shown in Figure 2-8 (b). It can also be seen that as AEV approaches infinity, the AEVs yield approximate to 5138.30 and 188.38 for Figures 2.8 (a) and 2-8 (b), respectively. Thus, two distinct relationships were described for the β for small-strain shear modulus. A regression analysis of the data showed that the saturation growth rate model adequately described the relationship between the scaling function and the AEV. The R^2 for the two relationships are 0.65 and 0.97 indicative of a fair correlation between β and AEV less than 100 kPa and an excellent correlation between β and AEV equal to or greater than 100 kPa, as shown in Figure 2-8.

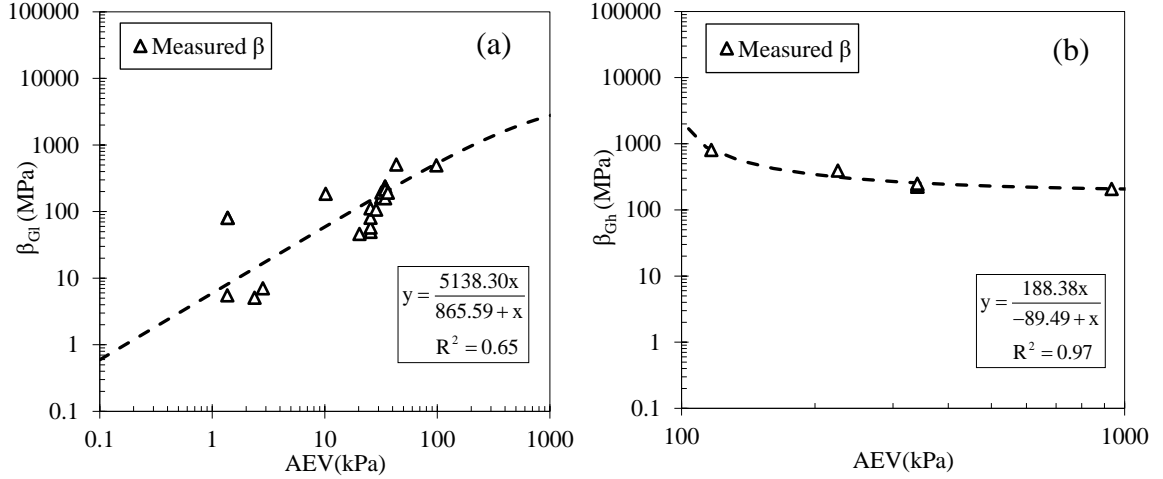


Figure 2-8 Variation of β to AEV for small-strain shear modulus; (a) soils with AEV less than 100 kPa; (b) For soils with AEV equal to or greater than 100 kPa.

To distinguish between the two models, the relationship for the β of soils with an AEV less than 100 kPa is denoted as β_{Gl} and is expressed as:

$$\beta_{Gl} = \frac{\lambda_1 \cdot AEV}{\lambda_2 + AEV} \quad (2-16a)$$

where λ_1 and λ_2 represent coefficients for β_{Gl} specified as 5138.30 and 865.59, respectively.

Conversely, for soils with an AEV equal to or greater than 100 kPa, it is represented as β_{Gh} and is expressed as:

$$\beta_{Gh} = \frac{\mu_1 \cdot AEV}{\mu_2 + AEV} \quad (2-16b)$$

where μ_1 and μ_2 represent coefficients for β_{Gh} specified as 188.38 and -89.49, respectively.

Rewriting Eq. (2-12) with the proposed relationships gives:

$$G_t(\psi) = G_0 - \left[\frac{\lambda_1 \cdot AEV}{\lambda_2 + AEV} \right] [S_e(\psi) - 1] \quad (2-17a)$$

$$G_h(\psi) = G_0 - \left[\frac{\mu_1 \cdot AEV}{\mu_2 + AEV} \right] [S_e(\psi) - 1] \quad (2-17b)$$

By employing the established relationships, coupled with knowledge of the SWCC of the soil, and an initial saturated shear modulus, it becomes feasible to estimate the unsaturated small-strain shear modulus for various soil types and stress conditions. However, a more definitive conclusion about the universal applicability of proposed relationships cannot be drawn due to the limited dataset although the soils used varied in terms of properties, testing methods, and stress conditions. Nevertheless, this framework can provide a preliminary directive for estimating the small-strain shear modulus, contingent upon prudent engineering judgement.

2.4.5 Performance of Proposed Empirical Relationship for β for G-suction

Two literature soils not employed in developing the proposed Eqs. (2-17a) and (2-17b) were selected for validation of the empirical relationship. The information on the study soils is outlined in Table 2-6. Specifically, a sandy soil tested at two net normal stresses of 50 kPa and 400 kPa was selected to assess the performance of Eq. (2-17a), while a fat clayey soil was selected to evaluate Eq. (2-17b).

In the case of the Fayette County Clay, measurements of small-strain shear modulus were conducted utilizing bender elements along a wetting path during sample saturation. As mentioned earlier, a wetting SWCC can be derived from a drying SWCC using Eq. (2-2). This approach was applied to the SWCC data for Fayette County Clay, which was obtained via the pressure plate technique. From Figure 2-9, it is evident that Eqs. (2-17a) and (2-17b) provide a reasonable accurate prediction of the measured small-strain shear modulus for these soils.

Table 2-6. Properties of reference soils used to predict small-strain shear modulus based on knowledge of SWCC and modified G-suction equation.

Reference	Soil name	USCS	$(\sigma - u_a)$ (kPa)	α (kPa)	n	m	Eq. (2-6) AEV (kPa)	β (kPa)	R^2
Hoyos et al. (2015)	Compacted Silty Sand	SM	50	26.17	1.05	0.32	8.06	47.38	0.93

			400	26.17	1.05	0.32	8.06	47.38	0.98
Kidd (2011)	Fayette County Clay	CH	7	336.72	0.98	0.13	149.73	468.19	0.77

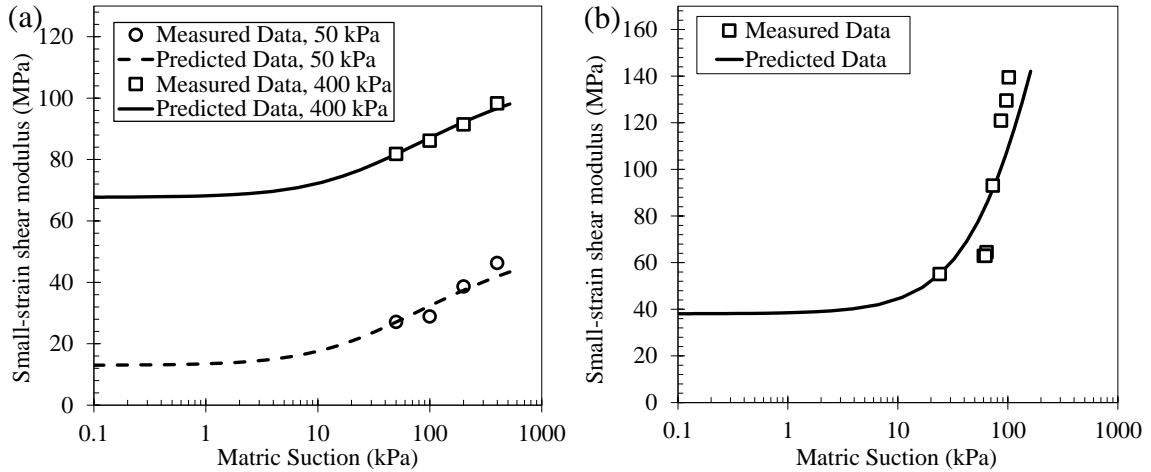


Figure 2-9 Validation of proposed equations for β with additional literature soils; (a) Compacted Silty Sand; (b) Fayette County Clay.

2.5 Proposed Approach for Unsaturated Shear Strength

The proposed mechanical-suction equation in Eq. (2-11) can be written in terms of shear strength as expressed in Eq. (2-18) and will be referred to as the τ -suction equation.

$$\tau(\psi) - \tau_0 = -\beta [S_e(\psi) - 1] \quad (2-18)$$

where $\tau(\psi)$ is the unsaturated shear strength at a given matric suction; τ_0 is the initial saturated shear strength at failure.

The approach of employing the τ -suction equation for predicting the shear strength of unsaturated soils requires, as was recognized with the small-strain shear modulus, an initial saturated shear strength. This parameter can be estimated using the classical Mohr-Coulomb failure criteria presented as:

$$\tau_0 = c' + \sigma' \tan(\phi') \quad (2-19)$$

where c' is the effective cohesion intercept at zero matric suction; σ' is the normal effective stress at failure during testing; and ϕ' is the effective internal angle of friction. The data for the triaxial tests is presented in terms of deviatoric stress. This information was then transformed into shear strength using the Mohr-Coulomb failure envelope, which is described in relation to principal stresses as:

$$\tau = \left(\frac{\sigma'_{1f} - \sigma'_{3f}}{2} \right) \cdot \left(\frac{1 - \sin \phi'}{\cos \phi'} \right) \quad (2-20)$$

where τ represents the Mohr-Coulomb failure criteria for saturated or unsaturated conditions; σ'_{1f} and σ'_{3f} are the major and minor principal effective stresses at failure, respectively.

2.5.1 Performance of the τ -suction Equation

From the results of the different soils, it is observed that the predicted shear strength matches well with the measured data as illustrated in Figure 2-10. The predicted τ -suction function indicates a flattened linear increase until the AEV and then increases nonlinearly. Additionally, just as was observed with the small-strain shear modulus data beyond the transition zone, the proposed approach consistently indicates an increase in shear strength. This is shown with the Guadalix Red Clay in Figure 2-10 (b), which shows an increase in shear strength for the measured data although there is a decrease after the peak shear strength around 6000 kPa. Consequently, the R^2 values decreased due to the inclusion of data within the residual zone. This is also observed in the Madrid Clay Sand and Air-dry Silty Clay, as outlined in Table 2-4.

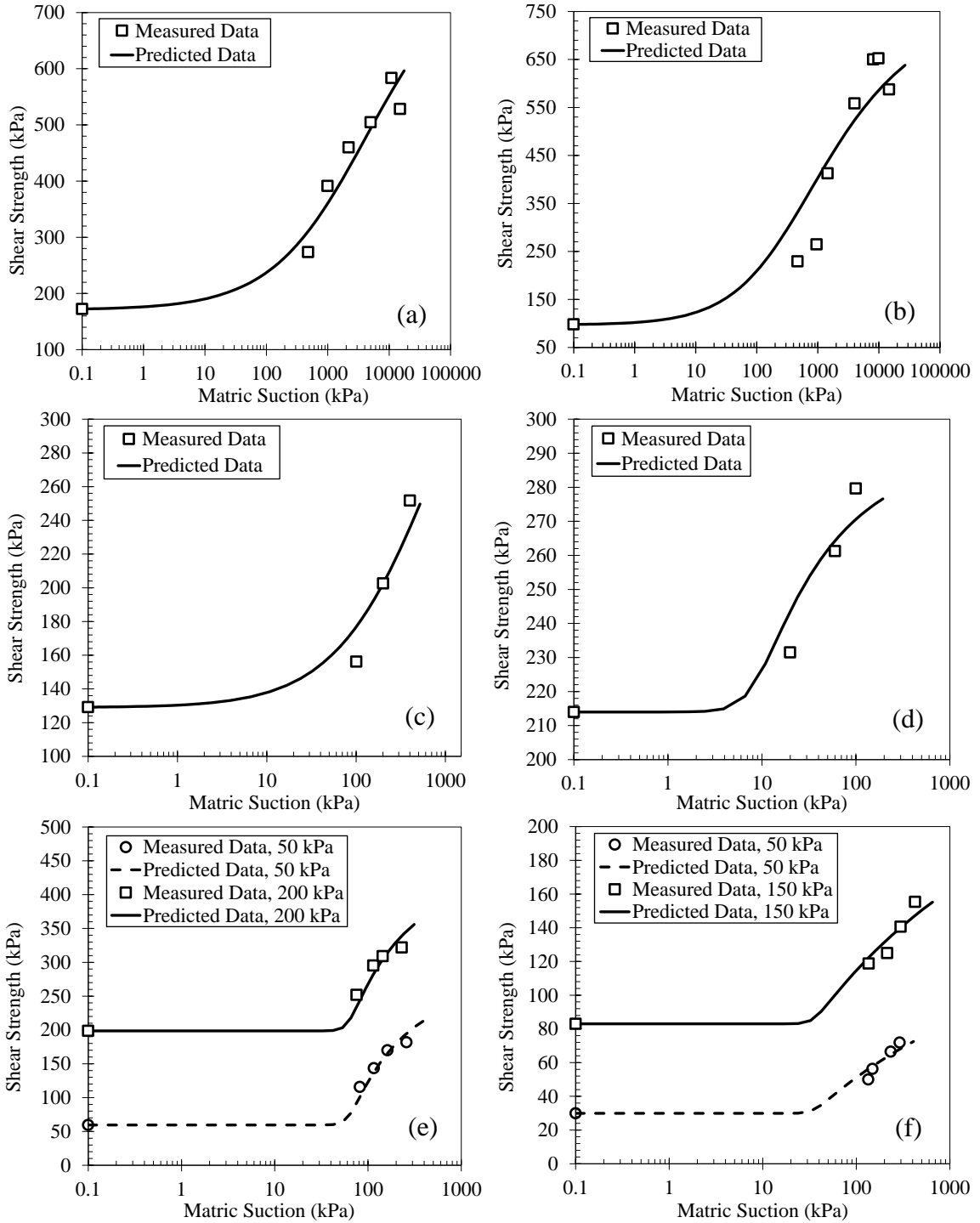


Figure 2-10 Measured and predicted shear strength for six literature soils at constant and varying net normal stresses: (a) Madrid Grey Clay at 300kPa; (b) Guadalix Red Clay; (c) SJ10B Hume Dam Clay; (d) Mine Tailings at 150m; (e) Coarse Kaolin; (f) Botkin Pit Silt.

2.5.2 Performance of the Proposed τ -suction Equation under Hydraulic Hysteresis Effects

To investigate the performance of β under hydraulic hysteretic conditions, Granitic Residual Clay was selected for this purpose (see Table 2-4). The shear strength for the wetting path was lower than the drying curve as shown in Figure 2-11 different to the behavior observed for small-strain shear modulus, which was higher at the wetting path than the drying path. As was discussed, the area of contact of particles is reduced during the wetting path and thus would result in a smaller shear strength as compared to the drying path. To mirror the wetting path mechanical behavior onto the drying SWCC, it would require a higher β value than that for the drying path.

The β values obtained for the Granitic Residual Clay shear strength data were 1689.79 kPa and 1898.4 kPa for the drying and wetting path, respectively. The β value obtained for a drying path can be adjusted for the wetting path by estimating the wetting path SWCC and then applying Eq. (2-18) similar to the procedure outlined for the small-strain shear modulus.

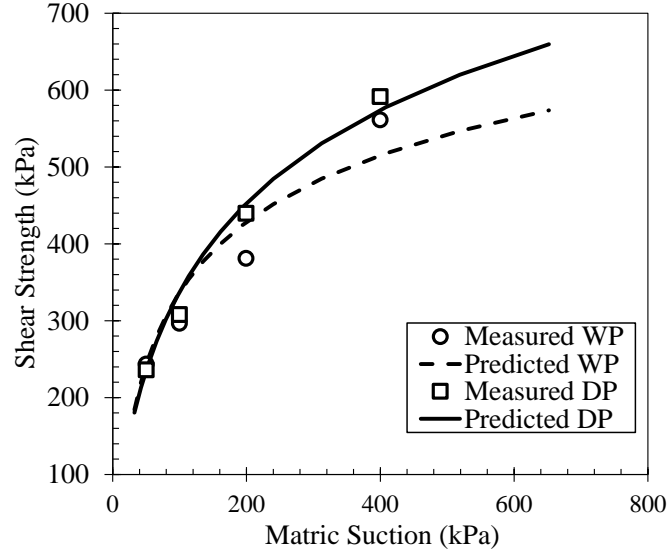


Figure 2-11 Performance of τ -suction under hysteretic effects for the Granitic Residual Clay (Han et al., 1995)

2.5.3 Proposed Empirical Relationship for β for τ -suction

In the absence of measured data, a relationship for β based on the SWCC for unsaturated shear strength is required. Figure 2-12 shows the variation of β values from measured triaxial and shear strength data plotted as a function of AEV for the study soils. The data is fitted with a saturation growth rate regression model. The plot illustrates a variable increase in β starting from an AEV of 0.1 kPa, which flattens out around 1000 kPa. The empirical relationship derived from the saturation growth rate model is expressed as,

$$\beta = \frac{\varepsilon_1 \cdot AEV}{\varepsilon_2 + AEV} \quad (2-21)$$

where ε_1 and ε_2 are the correlation coefficients for the scaling parameter for τ -suction equation given as 1351.92 and 163.26, respectively. In this case, as the AEV reaches a maximum of close to 1000 kPa and greater, the corresponding β values equal ε_1 .

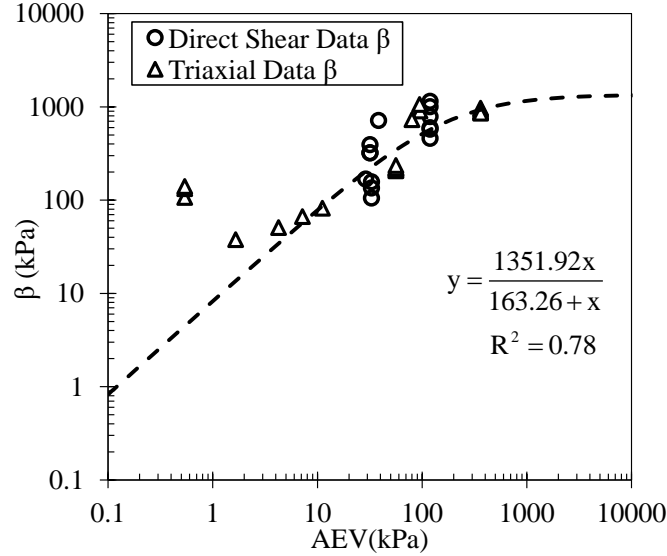


Figure 2-12 The relationship between β and the AEV for shear strength using triaxial and shear strength data.

The proposed relationship can be inserted in the τ -suction equation presented in Eq. (2-18) which is given as:

$$\tau(\psi) - \tau_0 = - \left[\frac{\varepsilon_1 \cdot AEV}{\varepsilon_2 + AEV} \right] [S_e(\psi) - 1] \quad (2-22)$$

2.5.4 Performance of Proposed Empirical Relationship for β for τ -suction

The performance of the proposed Eq. (2-22), which incorporates the correlation for β with AEV, was validated using the Indian Head Till tested by Vanapalli et al. (1996). As with the small-strain shear modulus, the validation soil was not used in the development of Eq. (2-22). Table 2-7 presents the SWCC fitting parameters, AEV, and β at two net normal stresses for this verification. Figure 2-13 illustrates the shear strength prediction alongside the actual measurements, demonstrating that the proposed Eq. (2-22) provides a well-matched estimation of the shear strength data. The SWCCs for the tested soil were performed at the same net normal stress as the direct shear test.

Table 2-7. SWCC fitting parameters for the literature soil used for validating the performance of the proposed relationship for β .

Reference	Soil name	USCS	$(\sigma - u_a)$ (kPa)	α (kPa)	n	m	Eq. (6) AEV (kPa)	β (kPa)	R^2
Vanapalli et al. (1996)	Indian Head Till	ML	25	60.28	1.25	0.12	33.35	229.31	0.97
			200	812.70	1.15	0.37	259.98	830.43	0.99

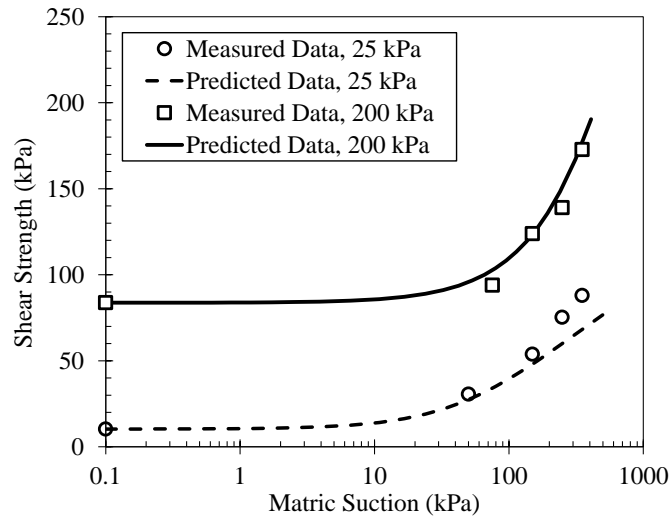


Figure 2-13 Measured and predicted data using the modified Eq. (22) for the Indian Head Till at two net normal stresses.

As discussed earlier with G -suction, it is recognized that the coefficients given by Eq. (2-21) were derived using soils covering a wide range of properties, testing methods and net normal stresses. However, these coefficients may not be representative for all soil types and stress conditions. Regardless, Eq. (2-22) may serve as a preliminary guidance for estimating shear strength of a soil in the absence of experimental data

CHAPTER 3. ESTIMATION OF UNSATURATED SMALL-STRAIN SHEAR MODULUS IN A LARGE-SCALE TEST BOX AND FIELD SITE FROM A SOIL-WATER CHARACTERISTIC CURVE

3.1 Introduction

The small-strain shear modulus of a soil is an important parameter used in the field of geotechnical engineering to determine the stability and stiffness properties of earth materials subjected to static and dynamic loading (Dong et al., 2018; Liu et al., 2021). Typically, in the field, small-strain shear modulus is determined from shear wave velocity by Eq. (3-1) using cross-hole technique, downhole technique, uphole technique, seismic dilatometer, multi spectral analysis of surface waves and other in-situ field methods (Liu et al., 2022; Romana-Giraldo and Bryson, 2023). In laboratory settings, the shear wave velocity is commonly obtained through methods like resonant column testing, bender elements testing, torsional shear testing (Wang et al., 2021; Yan et al., 2023). Among these, resonant column and bender elements are the most frequently employed laboratory methods for determining shear wave velocity (Yang and Liu, 2016; Romana-Giraldo and Bryson, 2023). Notably, results obtained from both techniques provide close approximation, as reported by Hoyos et al. (2015).

$$G = \rho \cdot V_s^2 \quad (3-1)$$

where G is the small-strain shear modulus; ρ is the bulk mass density; and V_s is the shear wave velocity.

The small-strain shear modulus can be indirectly estimated from dynamic cone penetrometer (DCP) measurements in the field, which are then converted to California bearing ratio (CBR) and subsequently to modulus, termed as resilient modulus due to its determination at larger strains. However, this indirect approach of estimating the small-strain shear modulus is not only expensive and laborious but also prone to compounded errors arising from the use of the various empirical relationships. The determination of the small-strain shear modulus from the shear wave velocity is influenced by various soil particle characteristics (size, shape, mineralogy), void ratio, soil type, degree of saturation, stress state and history (Hardin and Richart Jr, 1963; Jafarian et al., 2018; Romana-Giraldo

and Bryson, 2023). These properties and state conditions have been integral in the development of predictive models for small-strain shear modulus.

Among these factors, the effect of soil moisture on the mechanical behavior of unsaturated soils due to the presence of negative pore pressures (matric suction) has been extensively studied (Zhai et al., 2019). The relationship between the soil moisture and matric suction is best described by the soil-water characteristic curve (SWCC). The SWCC holds significant importance for stiffness and strength assessment of partially saturated soils (Bayat et al., 2019; Kristo et al., 2019; Mahmoodabadi and Bryson, 2021a). In addition, it should be noted that field conditions exhibit varying moisture conditions (hysteresis) due to seasonal variations (Barus et al., 2019; Ahmed et al., 2021). Therefore, consideration of hysteresis is important in the determination of stiffness and strength of unsaturated soils. This aspect is often overlooked when employing DCP-derived or other soil properties-derived empirical relationships to determine shear modulus.

Currently, most deterministic models (Sawangsurriya et al., 2009; Han and Vanapalli, 2016; Ngoc et al., 2019; Mahmoodabadi and Bryson, 2021a; Yan et al., 2022) for estimating the small-strain shear modulus of unsaturated soils rely only on data obtained from small laboratory specimens subjected to varying pressures and accounting for soil suction. However, it is important to recognize that both field and laboratory conditions differ significantly in terms of mechanical and hydrological properties due to factors like boundary conditions, sampling disturbance, spatial variability, and seasonal variations (Mahmoodabadi and Bryson, 2021b; Dadashiserej et al., 2023). Therefore, predictive models derived solely from small laboratory specimens may not accurately reflect field conditions and thus would require some modifications. Few models (Carlton and Pestana, 2016; Barus et al., 2019) exist that combined laboratory and field tests data to develop a unified model for estimating small-strain shear modulus. However, the model by Carlton and Pestana (2016) focused on parameters such as void ratio, plasticity, and stress state without the inclusion of the impact of moisture conditions. On the other hand, the model proposed by Barus et al. (2019) accounted for the influence of the SWCC, but it was specifically developed to estimate small-strain shear modulus post-compaction, limiting its broader applicability.

This study introduces a model to estimate the small-strain shear modulus of unsaturated soils based on the inverse relationship between SWCC and mechanical behavior obtained from small laboratory specimen testing. The proposed model is then applied to compacted soils in a large-scale test box to develop a correlation applicable to field sites under both pre-compaction and post-compaction conditions. The secondary objective was to evaluate the performance of pedotransfer functions in estimating the fitting parameters for the SWCC in comparison to the SWCC obtained from moisture sensors in the large-scale test box. Finally, the modified model with the correlation from the test box is applied to a field-site, demonstrating its ability to predict measured data. The model offers significant benefits for preliminary analysis in geotechnical projects requiring knowledge of small-strain shear modulus.

3.2 Overview of Proposed Model to Estimate Small-Strain Shear Modulus of Unsaturated Soils

3.2.1 Hydrologic Behavior of Unsaturated Soils

The hydrologic behavior of unsaturated soils is primarily characterized based on the soil-water characteristic curve (SWCC). Among its key defining points are the air-entry value and residual value, which serve to delineate boundary-transition and transition-residual zones, respectively (Fredlund, 2019; Rahardjo et al., 2019). The air-entry value (AEV) marks the transition from a saturated to an unsaturated state, holding significant importance in describing soil mechanical behavior. Therefore, accurately determining the AEV is crucial. This study employs the approach outlined by Soltani et al. (2021) to precisely determine the AEV for the soils, offering a more accurate alternative to visual identification methods. On the other hand, the residual value indicates minimal water desaturation, signifying reduced influence of matric suction on mechanical behavior in the residual zone (Han and Vanapalli, 2016; Mahmoodabadi and Bryson, 2021a).

Establishing the SWCC in the laboratory involves various testing methods, such as the axis translation technique (employing Tempe cell and pressure plate devices), Fredlund SWCC device, or dewpoint potentiometer (Nam et al., 2010; Fredlund, 2019). Among these methods, the axis translation technique with the pressure plate device is commonly

used (Li et al., 2005). However, data collection using these methods can be labor-intensive and time-consuming, especially when gathering data points across increasing matric suction for a single soil test.

To address this challenge, hydrologic models have been developed to analytically estimate the SWCC from a limited number of measured data points. In this study, the van Genuchten (1980) hydrologic model described in Eq. (3-2) was utilized due to its robustness and applicability across a wide range of soil textures (Mahmoodabadi and Bryson, 2021a).

$$S_e = \left(\frac{\theta - \theta_r}{\theta_s - \theta_r} \right) = \left[1 + \left(\frac{\psi}{\alpha} \right)^n \right]^{-m} \quad (3-2)$$

where S_e is the effective degree of saturation; ψ is matric suction; θ is the volumetric water content; θ_s is the saturated volumetric water content; θ_r is the residual volumetric water content; α is the fitting parameter related to the air-entry value; n is related to the water extraction beyond the air-entry value and is usually associated to the pore-size distribution; and m is a fitting parameter related to the residual matric suction. The model fitting parameters were determined through optimization using the least square difference between the measured and predicted data, a process facilitated by the Microsoft Excel Equation Solver.

The model fitting parameters can be indirectly determined using pedotransfer functions (PTFs). These PTFs are mathematical models that estimate soil hydraulic, physical and chemical properties based on readily available data. Various PTFs have been developed by researchers, incorporating various soil properties (Schaap et al., 1998; Pittaki-Chrysodonta et al., 2018; Minasny et al., 2021). Schaap et al. (2001) introduced Rosetta, a computer program which utilizes hierarchical PTFs and neural network analyses to estimate the van Genuchten fitting parameters. The hierarchical PTFs required as input for Rosetta include the USDA textural class, percentages of sand, silt, and clay, bulk density, and volumetric water content at 33 kPa and 1500 kPa. Notably, textural characteristics and bulk density are frequently used input parameters, as they can be derived without having to run numerous tests.

In field settings, moisture conditions often demonstrate hysteretic behavior, involving drying and wetting cycles contingent upon initial moisture levels. Given the likelihood of seasonal fluctuations, it becomes crucial to accommodate such variations in analysis and modeling. Ahmed et al. (2021) introduced a method facilitating the estimation of the wetting curve from a drying curve through the utilization of multiplication factors within the modified van Genuchten (1980) equation presented as:

$$S_e = \left[1 + \left(\frac{f_1 \psi}{\alpha} \right)^{f_2 n} \right]^{-f_3 m} \quad (3-3)$$

where f_1 , f_2 , and f_3 are multiplication factors for the conversion taken to be 2.2, 1.2, and 2.6 respectively.

3.2.2 Proposed Small-Strain Shear Modulus Model for Unsaturated Soils

Several experimental studies (Khosravi et al., 2010; Dong et al., 2016; Xu and Zhou, 2016) have demonstrated the inverse S -shaped relationship between the small-strain shear modulus of unsaturated soils and the SWCC, with increasing matric suction. This inverse relationship was illustrated using two distinct soil types sourced from literature, as shown in Figure 3-1. The soils utilized were SG-2, as reported by Lee et al. (2007) and Bonny silt, as reported by Khosravi et al. (2018), both subjected to testing using the bender elements method. The geotechnical index properties and van Genuchten (1980) fitting parameters for the two soils are provided in Table 3-1.

Table 3-1. Geotechnical index properties and SWCC fitting parameters of literature soils used to show inverse relationship.

Soil name	USCS	S_G	PI	α (kPa)	n	m	AEV (kPa)
SG-2	SP	2.67	4.9	10.50	1.47	0.37	6.16
Bonny silt-1	ML	2.6	4	42.47	1.78	0.37	20.37

Note: USCS = Unified Soil Classification System; S_G = specific gravity of the soil; PI = plasticity Index.

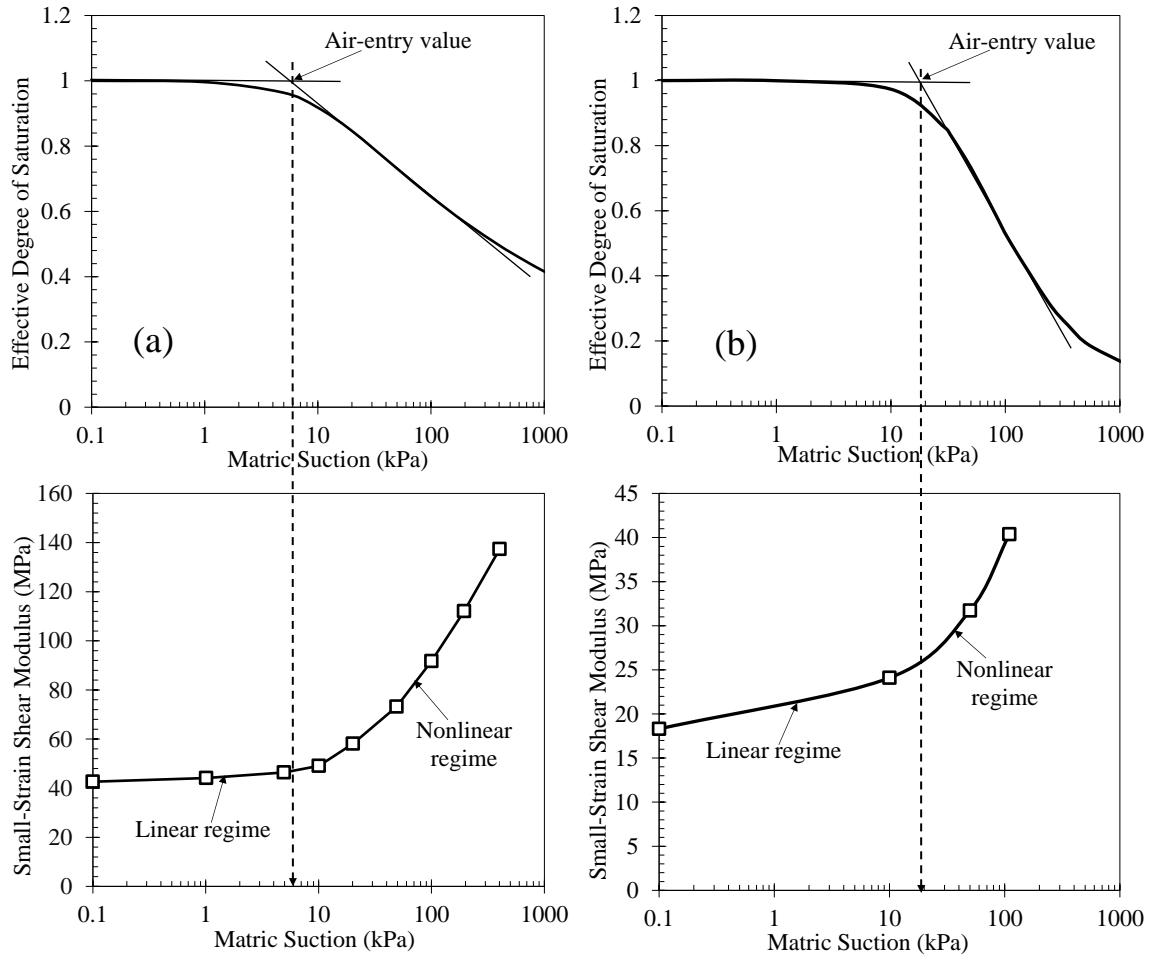


Figure 3-1 Graphical representation of the relationship between the small-strain shear modulus behavior and SWCC with respect to increasing matric suction; (a) SG-2 (data from Lee et al., 2007); (b) Bonny silt at 40 kPa (data from Khosravi et al., 2018a).

The inverse relationship between the small-strain shear modulus and the SWCC can be mathematically expressed as:

$$\frac{dG}{d\psi} \propto -\frac{dS_e}{d\psi} \quad (3-4)$$

where G represents the small-strain shear modulus of partially saturated soils; and ψ is the matric suction, defined as the difference between the pore-air and pore-water pressure ($u_a - u_w$).

Eq. (3-4) was rewritten by introducing a constant, β defined as the scaling function. The β describes the negative slope to mirror the SWCC onto the small-strain shear modulus curve.

$$\frac{dG}{d\psi} = -\beta \frac{dS_e}{d\psi} \quad (3-5)$$

By integrating both sides of the equation with respect to matric suction and setting the initial saturation point to be unity, the following expression was derived:

$$G(\psi) - G_0 = -\beta [S_e(\psi) - 1] \quad (3-6)$$

where $G(\psi)$ is the small-strain shear modulus at various matric suctions; G_0 is the initial saturated small-strain shear modulus; and $S_e(\psi)$ is the effective degree of saturation at a given matric suction and is given by Eqs. (3-2) and (3-3) for both the drying and wetting curves of the SWCC, respectively. Eq. (3-6), termed herein as the G -suction equation, provides a general framework model for predicting small-strain shear modulus with respect to matric suction, based on the inverse relationship of the SWCC and a known initial saturated small-strain shear modulus.

3.2.3 Saturated Small-Strain Shear Modulus

The proposed G -suction model relies on the determination of the saturated small-strain shear modulus, which requires costly equipment and considerable amount of time for testing. Hardin and Black (1969) introduced an equation for estimating the saturated small-strain shear modulus based on void ratio, confining stress, and plasticity index. The equation is given as:

$$G_0 = A \cdot f(e) (OCR)^k (\bar{\sigma}'_0)^\zeta \quad (3-7)$$

where A represents a dimensionless material constant coefficient; $f(e)$ is a function related to the void ratio, e ; OCR is the overconsolidation ratio; k is an exponent specific to the overconsolidation ratio dependent on the plasticity index of the soil; $\bar{\sigma}'_0$ is

the mean effective stress; and ζ is an exponent based on contact between particles and strain amplitude, typically assumed to be 0.5. The equation for the void ratio function is:

$$f(e) = \frac{(2.973 - e)^2}{1 + e} \quad (3-8)$$

The mean effective stress is expressed as:

$$\bar{\sigma}'_0 = \frac{\sigma'_v}{3}(2 \cdot K_0 + 1) \quad (3-9)$$

where σ'_v is the effective stress of the soil; K_0 is the coefficient of earth pressure at rest which is expressed as:

$$K_0 = 1 - \sin(\phi') \quad (3-10)$$

where ϕ' is the drained friction angle of the soil.

The parameter A has been defined differently depending on various soil types. However, preliminary studies calibrated the A value using data on saturated small-strain shear modulus obtained from literature soils with varying properties and testing methods (resonant column and bender elements), to account for various soil types. Through regression analysis, by plotting $G_0/f(e)(kPa)$ against $\bar{\sigma}'_0{}^{0.5}$, a gradient of 3419.4 was derived. This gradient represents the calibrated A value for the Hardin and Black (1969) equation, which is subsequently integrated into Eq. (3-11), defined as:

$$G_0 = 3419.4 \cdot f(e)(OCR)^k (\bar{\sigma}'_0)^{0.5} \quad (3-11)$$

3.2.4 Determination of Scaling Function

The scaling function, β , was rigorously derived by optimizing measured and predicted data for 13 literature soils using Excel Solver. From this analysis, empirical relationships were established to estimate β by passing a regression model through a plot of β against AEV. These relationships were formulated considering the variability in net

normal stresses, matric suction, and moisture conditions (including both drying and wetting) of the study soils. The empirical relationships are expressed as:

$$\beta_{Gl} = \frac{5138.30 \cdot AEV}{865.59 + AEV} \quad \text{if } AEV \leq 100 \text{ kPa} \quad (3-12a)$$

$$\beta_{Gh} = \frac{188.38 \cdot AEV}{-89.49 + AEV} \quad \text{if } AEV > 100 \text{ kPa} \quad (3-12b)$$

where β_{Gl} is the scaling function applicable to soils with AEV less than or equal to 100 kPa, and β_{Gh} represents the scaling function applicable to soils with AEV greater than 100 kPa.

3.2.5 Performance Evaluation of Proposed G-suction Equation

The proposed G -suction equation was evaluated using data from 13 literature soils. Table 3-2 provides the SWCC fitting parameters for 4 of the 13 soils. In Figure 3-2(a) and 3-2(b), a well graded sand and fat clay, respectively, were utilized to demonstrate that the G -suction model well predicts the measured data. Hysteretic conditions were evaluated by using test data from Khosravi and McCartney (2012) at three different net normal stresses of 100 kPa, 150 kPa (Figure 3-2 (c)) and 200kPa. The scaling function, β was found to be smaller for the wetting curve than the drying curve due to the reduced contact area between the soil particles as moisture content increases, leading to a faster propagation path for the shear wave velocity and consequently yielding a higher small-strain shear modulus.

However, as the small-strain shear modulus increases, the AEV decreases, requiring a lower β . Since obtaining β using the rigorous approach requires measured small-strain shear modulus data, the proposed empirical relationship presented in Eq. (3-12a) was employed to estimate β based on the AEV less than 100 kPa. Subsequently, this estimation was incorporated into the G -suction model and tested on two soils. One soil, compacted silty sand, as reported by Hoyos et al. (2015), was tested under two net normal stresses of 50 kPa and 400 kPa (Figure 3-2 (d)). The predicted small-strain shear modulus

from the modified equation closely aligned with the measured data, validating the effectiveness of the approach.

Table 3-2. SWCC parameters and scaling function of the literature soils used to evaluate the performance of the proposed model.

Reference	Soil name (USCS)	$(\sigma - u_a)$ (kPa)	α (kPa)	n	m	AEV (kPa)	β (kPa)
Takkabutr (2006)	Ottawa Sand (SP)	17.25	42.57	2.90	0.49	25.55	49.48 ^a
Sawangsurriya et al. (2009)	DI TH23 Slopes (CH)	35	286.81	0.79	0.49	43.24	506.88 ^a
Khosravi and McCartney (2012)	Bonnie Silt-2 ^d (ML)	150	25	4.60	0.78	16.84	8.49 ^a
	Bonnie Silt-2 ^w (ML)	150	14.29	3.50	0.71	8.66	4.20 ^a
Hoyos et al. (2015)	Compacted Silty Sand (SM)	400	26.17	1.05	0.32	8.06	47.38 ^b

Note: superscripts *d* and *w* are drying and wetting paths, respectively; *a* and *b* are scaling functions obtained by the rigorous approach and empirical relationship in Eq. (12a), respectively.

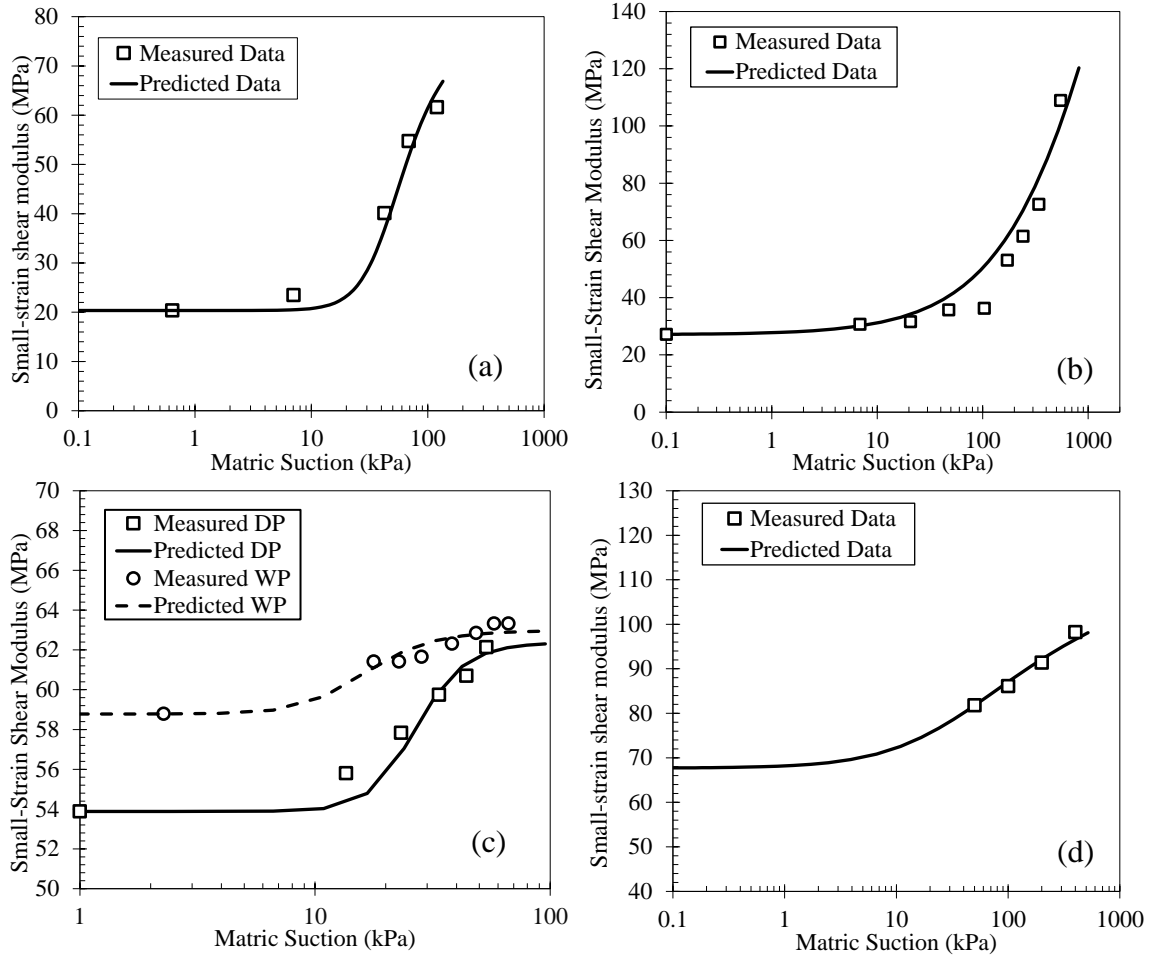


Figure 3-2 Measured and predicted small-strain shear modulus for four literature soils: (a) Ottawa Sand at 17.25 kPa; (b) DI TH23 Slopes Clay at 35 kPa.; (c) Bonny Silt at 150 kPa; (d) Compacted Silty Sand at 400 kPa using the proposed empirical relationship in Eq. (12a). In the figure, DP=Drying Path; WP=Wetting Path.

3.3 Laboratory Box Testing

3.3.1 Test Soils and Preparation

The test soils used in this study were natural clay and river sand, specifically named Hamburg clay, and Kentucky (KY) River sand, respectively, based on their sampling location in the state of Kentucky. Table 3-3 outlines the geotechnical index properties of these two test soils. These soils were selected to represent a variety of textures and plasticity levels typical of soils used in developing the proposed G -suction equation. To ensure consistency, the test soils were compacted to attain dry unit weights approximately equivalent to standard Proctor compaction.

Table 3-3. Geotechnical index properties of soils used for the box test to evaluate the performance of the proposed equation for small-strain shear modulus.

Soil Name	USCS	S_G	PI	Sand (%)	Silt (%)	Clay (%)	γ_{dry} (kN/m ³)	ω_{opt} (%)	γ_b (kN/m ³)	ϕ' (deg)
Kentucky River sand	SP-SM	2.65	-	88.6	11.4	-	16.08	15.4	18.56	32
Hamburg clay	CL	2.64	12	8.45	23.28	68.27	15.81	21.6	19.23	30

Note: γ_{dry} = maximum dry unit weight; ω_{opt} = optimum moisture content; γ_b = bulk unit weight; and ϕ' = drained friction angle.

3.3.2 Test Box Setup and Sensors

The test box utilized in this study was fabricated from Lexan polycarbonate and had dimensions of 60 cm x 60 cm x 40 cm (length x width x height) with a thickness of 3.3 cm. Within this box, TEROS 12 volumetric moisture and electrical conductivity sensors were strategically positioned at various depths to measure volumetric water content. Simultaneously, TEROS 21 sensors were placed at the same locations to measure matric potential. Additionally, PCB accelerometers were installed alongside the moisture and electrical sensors. To induce shear and compressional waves within the soil, a metallic plate was positioned at the soil surface (Figure 3-3 (a)) and struck with a hammer longitudinally and transversely, respectively. A schematic diagram illustrating the layout of the test box, including the arrangement of sensors and accelerometers, is illustrated in Figure 3-3 (b).

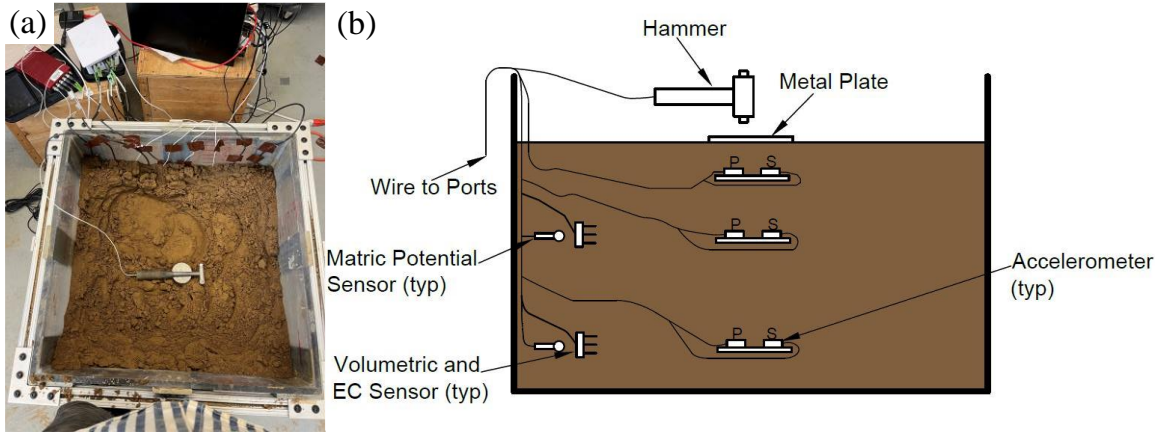


Figure 3-3 Test Box; (a) Aerial view of soil placed in box with sensors; (b) Schematic Diagram of box illustrating the setup.

3.3.3 Testing Procedure

The soil compaction procedure involved dropping a 24 kg hammer from a height of 30.48 cm, delivering 11 blows per pass across 9 points to cover the entire soil surface to ensure uniform compaction throughout the soil surface. Each soil sample underwent four tests at specific moisture contents: 18%, 20%, 22%, and 24% for Hamburg clay, and 10%, 12%, 14%, and 16% for Kentucky River sand. These moisture contents were centered around their respective optimum moisture contents determined from standard Proctor tests (21.6% for Hamburg clay and 15.4% for Kentucky River sand, as shown in Table 3-3).

To minimize sidewall deflection and box expansion during compaction, steel stiffness members and threaded rods were installed to the exterior of the test box, ensuring accurate soil volume estimation within the box. A drainage layer primarily composed of gravel was placed beneath the test soil, with a geosynthetic fabric atop it to prevent clogging by finer soil particles. Additionally, samples were taken and placed in moisture cans after allowing the soil to reach moisture equilibrium over 24 hours. The moisture obtained from the can was then compared with the moisture measured by the volumetric moisture sensors.

After 24 hours, a metal plate was positioned on the compacted soil surface and struck with a hammer to generate waves (input) that traveled through the soil and were detected by the accelerometers (receiver). Figure 3-4 illustrates a typical input wave (blue) from the hammer and the corresponding received wave (red) detected by the accelerometer.

The highest blue peak represents the impact from the hammer, while the smaller blue waveforms depict residual vibrations from metal plate, considered as noise. The waveforms were recorded as output using DataPhysics software and exported into a spreadsheet file. The arrival time was then determined through visual inspection of the point of first deflection, a method commonly adopted by various researchers (Viggiani and Atkinson, 1995; Lings and Greening, 2001). Subsequently, shear (S) and compressive (P) waves were computed as:

$$V = \frac{L}{t} \quad (3-13)$$

where V is the wave velocity; L is the wave travel distance; t denotes the wave velocity propagation time.

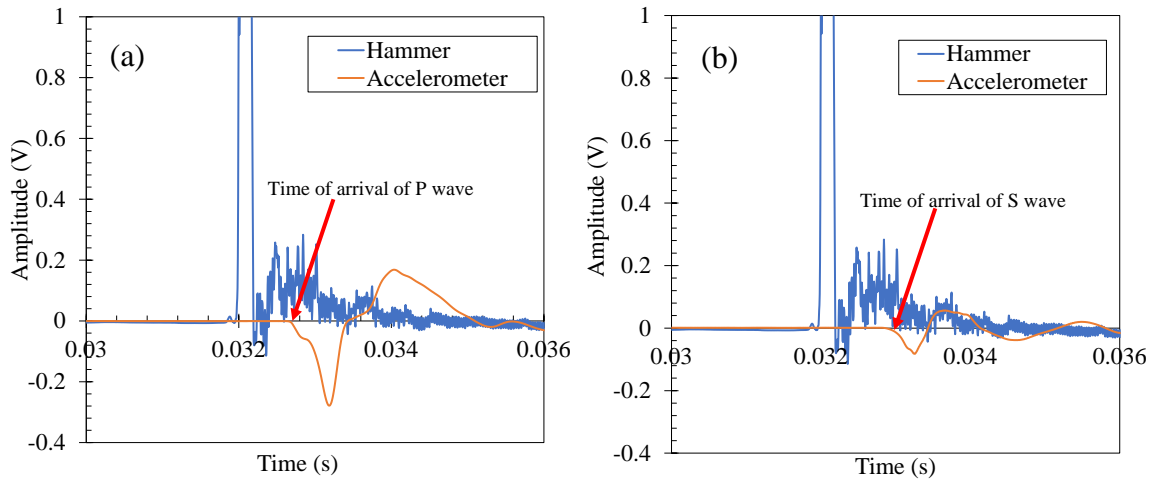


Figure 3-4 Wave propagation arrival times; (a) P-wave velocity; (b) S-wave velocity.

3.3.4 Hydrologic Model for Test Box

3.3.4.1 SWCC from Sensors

As previously discussed, TEROS 12 volumetric and electrical conductivity sensors, as well as TEROS 21 matric potential sensors, were positioned at various depths within the test box for both the Hamburg clay and KY River sand. These sensors were employed to measure soil moisture, electrical conductivity, and matric potential, respectively. In the case of Hamburg clay, sensors were situated at three distinct depths, while for the KY River

sand, sensors were placed at two depths. The data gathered from these sensor depths was subsequently plotted and fitted with hydrologic models to describe the SWCC.

3.3.4.2 SWCC from Rosetta

The HYDRUS-1D version 3.0 software, developed by Simunek et al. (2005) and embedded with Rosetta, was utilized to predict hydrologic fitting parameters, α and n , as well as moisture contents θ_s and θ_r for the test soils. Rosetta requires input data regarding textural characteristics (% sand, % silt, and % clay) along with the bulk density of the soil. Various studies (Li et al., 2016; Wassar et al., 2016; Pittaki–Chrysodonta et al., 2021) have evaluated the performance of Rosetta in estimating soil hydrologic fitting parameters. Pittaki–Chrysodonta et al. (2021) reported that sands and silts tend to yield better results with Rosetta compared to clays, although it still provided a close fit with measured data. Since KY River sand had no clay percentage, zero value was inputted as the value under clay percents. The fitting parameter m was obtained from the Mualem (1976) approximation presented as:

$$m = 1 - \frac{1}{n} \quad (3-14)$$

Table 3-4 summarizes the fitting parameters derived from the van Genuchten (1980) model by optimizing the measured data from the test box and utilizing Rosetta. Both hydrologic fitting models demonstrate close agreement with the measured data for KY River sand, as depicted in Figure 3-5 (a). However, for Hamburg clay, as illustrated in Figure 3-5 (b), the SWCC derived using Rosetta exhibits a higher air-entry value compared to the SWCC derived from optimization using measured box data.

Table 3-4. SWCC fitting parameters for the sands from the box test data and Rosetta.

Data source	Soil name	α (kPa)	n	m	θ_s	θ_r	AEV (kPa)
Box sensors	Hamburg clay	12.71	1.15	0.13	0.4329	0.03	6.396
	KY River sand	23.47	1.68	0.41	0.1918	0.03	10.388
Rosetta	Hamburg clay	50.25	1.16	0.14	0.3272	0.08	24.952
	KY River sand	23.47	2.47	0.60	0.2758	0.04	12.168

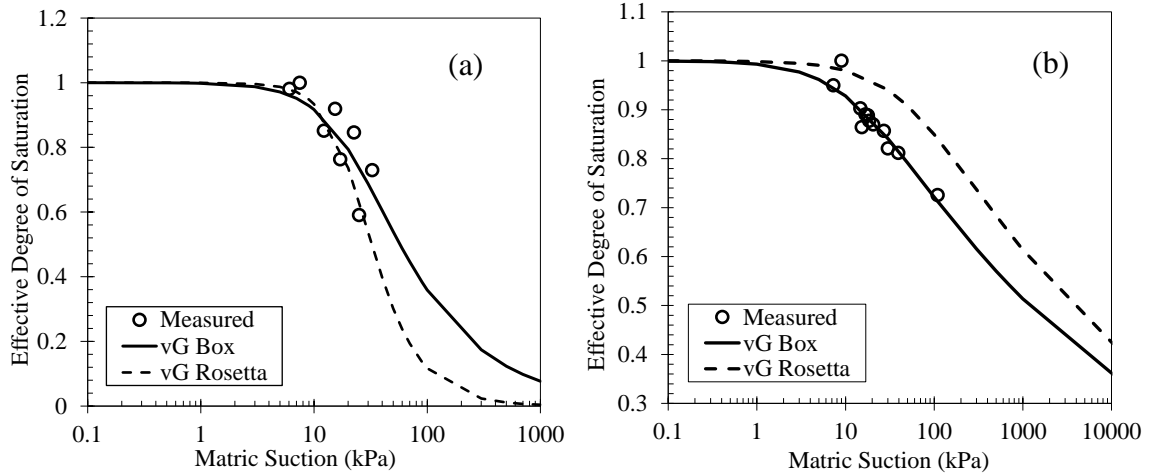


Figure 3-5 Soil-water characteristic curve for the test box from measured sensor in box and Rosetta; (a) KY River sand; and (b) Hamburg clay.

3.3.5 Modification of Proposed G-Suction Equation with Box Test Data

The proposed G -suction model was applied to analyze the two soils compacted within the test box. This involved utilizing the saturated small-strain shear modulus obtained from the modified Hardin and Black (1969) equation in Eq. (3-11), along with the SWCC, to predict the unsaturated small-strain shear modulus in the test box. To achieve this, the rigorous approach was applied to obtain β using the measured data, as shown in Figure 3-6. The scaling function, β for KY River sand and Hamburg clay based on the rigorous approach was estimated to be 94.468 kPa and 399.26 kPa, respectively. The objective was to calibrate the proposed empirical relationship for β to enable its application on a large-scale soil.

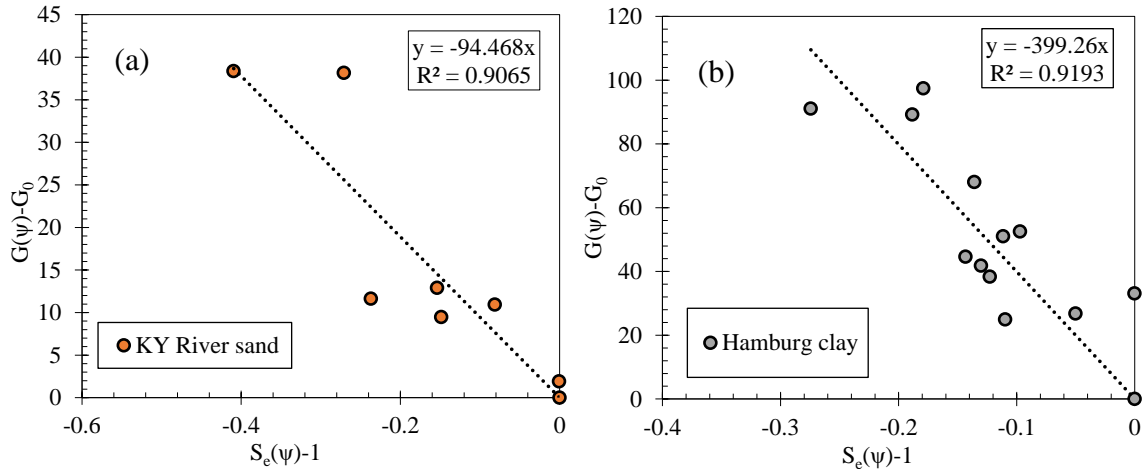


Figure 3-6 Rigorous approach for obtaining β from measured small-strain shear modulus data and SWCC using proposed approach.

Figure 3-7 illustrates the predicted data closely matches the measured data when employing the rigorous approach. However, it should be noted that the proposed model tends to increase even within the residual zone of the SWCC, as can be seen for the Hamburg Clay at a matric suction close to a 100 kPa. The measured data at 100 kPa is approximately 120 kPa and the predicted data is approximately 160 kPa which is higher and is a limitation of the model. The proposed empirical relationship in Eq. (3-12a) was also utilized to estimate β using the AEV from Rosetta and the box sensors and subsequently incorporated in the G -suction equation to predict the measured data. The G -suction model using the β obtained from Eq. (3-12a) for both the test box and Rosetta exhibits a satisfactory agreement with the measured data for KY River sand, as depicted in Figure 3-7 (a). However, there is a slight deviation between 5 kPa to 10 kPa for the Rosetta β and between 3 kPa to 50 kPa for the test box β .

In the case of Hamburg clay, as depicted in Figure 3-7 (b), there is a notable offset for the G -suction model obtained for both Rosetta and the test box in comparison to the G -suction model obtained from the rigorous approach. This is because the AEV obtained for the Hamburg clay for the box sensors and Rosetta when used to calculate for β is lower compared to the β obtained by optimization of measured data. Since the β is purposed to mirror mechanical behavior to SWCC, the smaller β results in a flat curve.

Due to these limitations in the proposed Eq. (3-12a) in estimating the rigorous β , the goal of the test box was to modify the proposed empirical relationship for large-scale test soils and field conditions, which differ from small laboratory samples used to generate the empirical equations. To do this a multiplier is required to adjust the lower predictions from Eq. (3-12a) onto the optimized β .

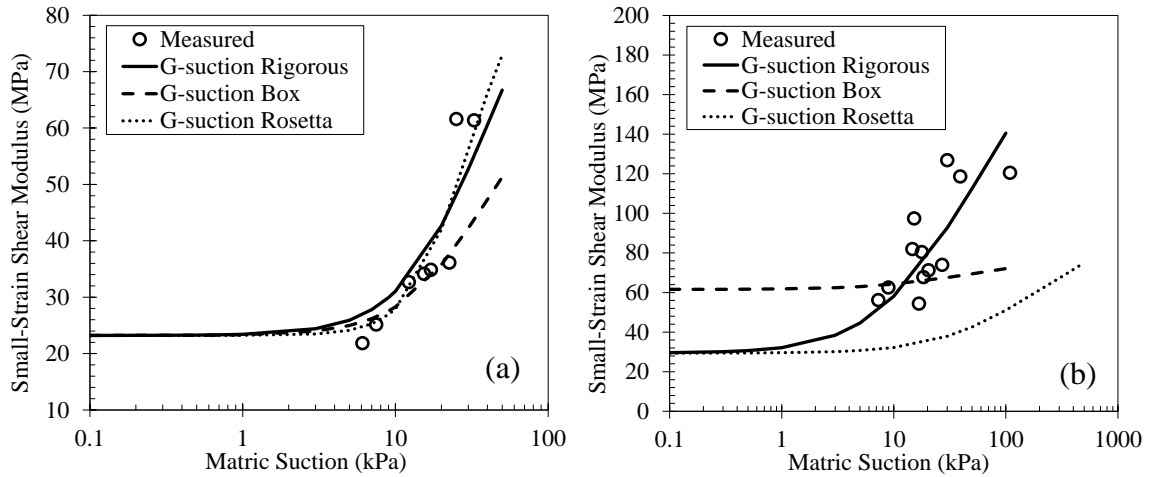


Figure 3-7 Measured and predicted small-strain shear modulus data; (a) KY River sand; and (b) Hamburg clay.

Table 3-5 provides the multipliers acquired by dividing the β obtained using the rigorous approach by the β obtained from both Rosetta and the test box using the empirical equation presented in Eq. (3-12a). Since the two test soils consist of sand and clay, a midpoint was included for silts based on the average. However, it is imperative for future research to determine the multiplier for silts.

$$M = \frac{\beta_{rig}}{\beta_{emp}} \quad (3-15)$$

where M is the multiplier to correlate the β obtained using the empirical relationship from small laboratory samples to a large compacted soil; β_{rig} is the scaling function obtained using the rigorous approach by optimizing measured data from the test box; β_{emp} is the scaling function obtained from Eq. (3-12a) in the absence of measured shear modulus data.

Table 3-5. Multipliers to modify the proposed G-suction model for large-scale compacted soils.

Data Source	KY River sand M	Hamburg clay M	Midpoint M (silts)
Box	1.55	10.59	6.07
Rosetta	1.33	2.77	2.05

Eq. (3-6) can be reformulated as Eq. (3-16) to address large-scale soils when unsaturated small-strain shear modulus data is unavailable.

$$G(\psi) - G_0 = -M \cdot \beta_{emp} [S_e(\psi) - 1] \quad (3-16)$$

Again, it is acknowledged that the proposed multiplier was developed for two soil types, and under limited moisture and density states. Additional research is required to ascertain factors influencing the multiplier.

3.4 Field Site

3.4.1 Description of Field Site

Field measurements of seismic and electrical resistivity were conducted at the Centre for Studies on Risks, the Environment, Mobility, and Urban Planning (CEREMA) facilities in Rouen Normandy, France, in 2019 by researchers from the University of Rouen Normandy. The test site was divided into three distinct areas, denoted as Area 1, Area 2, Area 3, each intended to represent different levels of target compaction efforts. These areas were designed to be 7 m long, 5 m wide and 0.75 m deep. To facilitate machinery access during construction and sampling within these areas, two zones were designated as "dead zones," each measuring 4 m in length. Consequently, no data was collected in these dead zones. The layout of the site, including the designated areas and dead zones, is illustrated in Figure 3-8.

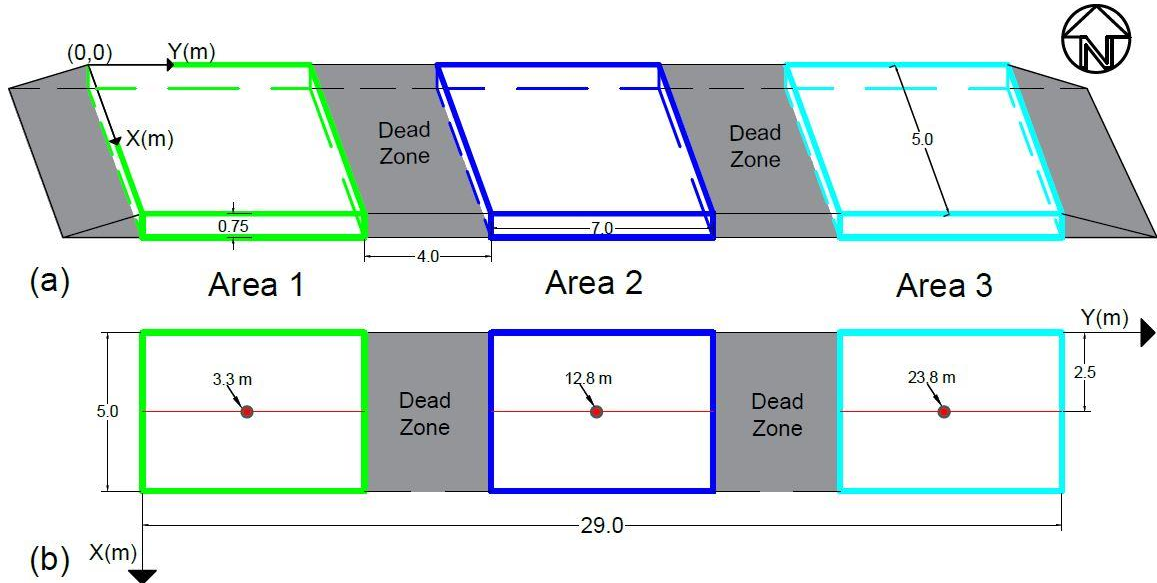


Figure 3-8 Field site. (a) Sectional view of test site showing the various areas, dead zones. (b) Plan view showing the measured points.

For this study, three specific points were selected, each situated at the midpoint of the three designated areas. The points were selected to minimize any potential boundary effects that may result from the uncompacted dead zones. Along the $X = 2.5$ m axis, the selected points were positioned at $Y = 3.3$ m for Area 1, $Y = 12.8$ m for Area 2, and $Y = 23.8$ m for Area 3. Geotechnical index properties of the three areas of the field site are presented in Table 3-6. The specific gravity and drained friction angle of the field site were assumed to be 2.65 and 30° , respectively. Additionally, the particle size distribution of the field site at a depth of 0.43-0.50 m was compared to the test soils, as illustrated in Figure 3-9. This comparison confirmed that the field site corresponds to a clayey silt classification according to the French soil classification system adopted by the research team in France.

Table 3-6. Textural characteristics of the test site at various depths from laboratory samples.

Area	Depth (m)	Sand (%)	Silt (%)	Clay (%)	γ_b (kN/m ³)	ω (%)
Area 1	0.18-0.25	17.2	58.2	24.6	17.55	15.6
	0.25-0.43	7.9	72.0	20.1	16.57	18.4
	0.43-0.75	7.8	81.3	10.9	16.57	16.5
Area 2	0.06-0.10	10.1	71.1	18.8	17.36	17.5

	0.10-0.14	15.0	69.6	15.4	17.06	15.5
	0.14-0.18	6.7	71.1	22.2	17.16	17.8
	0.18-0.35	5.5	74.4	20.1	17.06	17.7
	0.35-0.39	15.0	69.1	15.9	16.97	15.5
	0.39-0.43	3.2	78.7	18.1	16.93	17.9
	0.43-0.54	2.5	68.8	28.7	16.87	15.4
	0.54-0.59	0.9	78.1	21.0	16.87	17.9
	0.59-0.75	0.4	82.3	17.3	16.48	17.7
Area 3	0.18-0.25	7.6	75.9	16.5	16.67	14.4
	0.25-0.50	1.6	76.9	21.5	17.46	18.2
	0.50-0.75	7.2	67.0	25.8	15.79	17.3

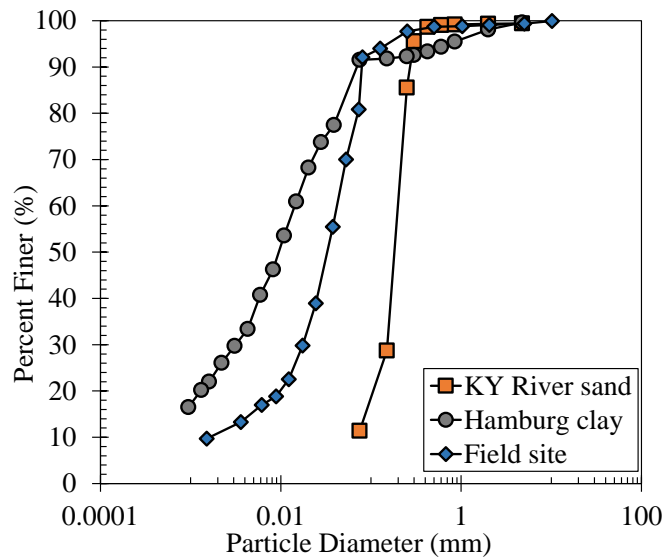


Figure 3-9 Particle size distribution of the field site at Area 2 at depth 0.18-0.25m in comparison to the test soils in the laboratory.

Seismic data were collected using the Multichannel Analysis of Surface Waves (MASW) method, employing 24 geophones spaced at 30 cm intervals at the center of the test site. The seismic shots were generated using a 1 kg hammer, with four successive hammer impacts stacked to enhance signal-to-noise ratio. Additionally, electrical measurements were conducted using the Wenner-Schlumberger setup, with 48 electrodes set at 0.50 m spacing for longitudinal profiling and 0.25 m spacing for transversal profiling.

Given the significance of dry unit weight in determining various soil properties, including void ratio, porosity, overburden pressure, and ultimately the saturated small-strain shear modulus, it was imperative to estimate the bulk unit weight using the shear wave velocity. In the absence of in situ data on unit weights at different depths for the three areas at the field site, the empirical relationship proposed by Mayne (2001) was utilized. This relationship, presented in Eq. (3-17) and derived from 727 datasets, enables the estimation of bulk unit weight based solely on shear wave velocity data at varying depths.

$$\gamma_b = 8.32 \log(V_s) - 1.61 \log(z) \quad (3-17)$$

where z is the depth of interest in meters.

As mentioned earlier, the three areas were distinct based on their level of compaction. Area 1 had the highest level of compaction followed by Area 2 and then Area 3. However, as illustrated in Figure 3-10, the targeted compaction strength for these areas was achieved at the selected points up to a depth of 0.2 m. Beyond this depth, Area 2 exhibited greater compaction compared to Area 3, followed by Area 1.

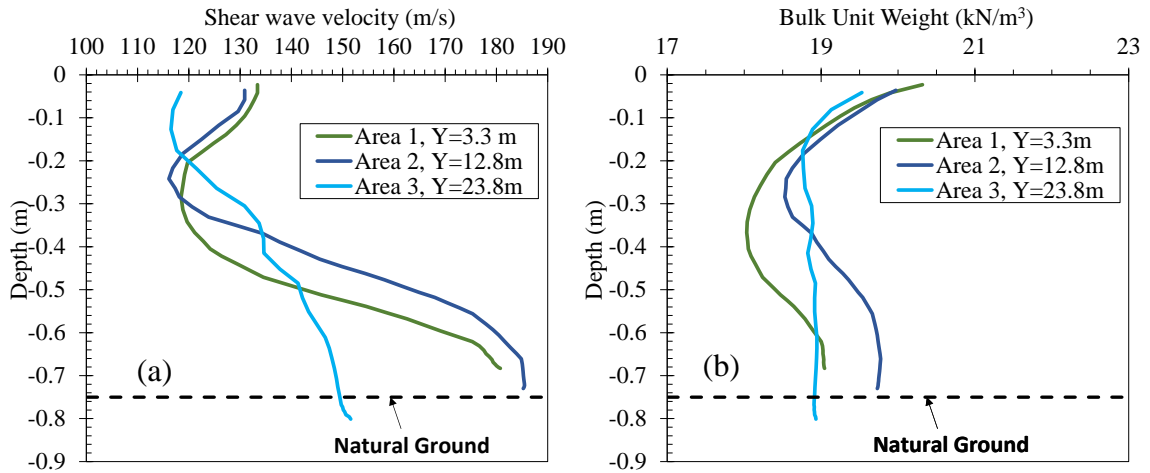


Figure 3-10 Variation of shear wave velocity and bulk unit weight at the three study points with depth.

3.4.2 Hydrological Model for Field Site

As discussed earlier, Rosetta provides the van Genuchten (1980) fitting parameters α , n , θ_s and θ_r based on textural characteristics and bulk unit weight of the soil. The parameter m was then determined using the Mualem (1976) approximation in Eq. (3-14).

Subsequently, the SWCC can be predicted using dummy range of matric suctions. Field conditions typically align well with the wetting curve of the SWCC obtained from the laboratory tests, following the first wetting curve (Li et al., 2005; Barus et al., 2019). In this study, the initial soil moisture at the field site was dry and subsequently made wet before performing seismic and electrical tests, indicative of a wetting path been followed. Therefore, the modified van Genuchten (1980) hydrologic model presented in Eq. (3-3) was used. The scaling function, β required was then calculated using the empirical relationship presented in Eq. (3-10a) since the soil at the test site had an AEV less than 100 kPa as presented in Table 3-7. Since the material at the test site was classified as silt, a multiplier of 2.05 was applied taken from Table 3-5.

Table 3-7. SWCC fitting parameters, air-entry values and scaling functions for the three areas of the field site at varying depths.

Area	Depth (m)	α (kPa)	n	m	θ_s	θ_r	AEV (kPa)	$M \cdot \beta_{emp}$ (kPa)
Area 1	0.18-0.25	101.01	1.39	0.28	0.3323	0.0589	15.9256	190.300
	0.25-0.43	138.89	1.52	0.34	0.3709	0.0631	22.1297	262.587
	0.43-0.75	125.00	1.53	0.35	0.3674	0.0509	19.9539	237.351
Area 2	0.06-0.10	120.48	1.46	0.32	0.3458	0.0563	19.0429	226.748
	0.10-0.14	119.05	1.48	0.33	0.3396	0.0510	18.8593	224.608
	0.14-0.18	126.58	1.47	0.32	0.3602	0.0630	20.0198	238.117
	0.18-0.35	129.87	1.49	0.33	0.3649	0.0617	20.5777	244.599
	0.35-0.39	121.95	1.49	0.33	0.3423	0.0522	19.3333	230.131
	0.39-0.43	131.58	1.50	0.33	0.3733	0.0610	20.8875	248.194
	0.43-0.54	121.95	1.45	0.31	0.3802	0.0730	19.2399	229.042
	0.54-0.59	133.33	1.50	0.33	0.3826	0.0661	21.1516	251.258
	0.59-0.75	136.99	1.53	0.35	0.3934	0.0639	21.8540	259.396
Area 3	0.18-0.25	135.14	1.53	0.34	0.3676	0.0581	21.5414	255.776
	0.25-0.50	123.46	1.45	0.31	0.3658	0.0632	19.4865	231.914
	0.50-0.75	142.86	1.53	0.35	0.3960	0.0739	22.7984	270.318

To determine the effective degree of saturation at the field provided with the θ_s and θ_r from Rosetta, the parameter needed is the volumetric water content, θ at the various depths. This can be estimated in the field using methods such as oven drying of field samples, volumetric sensors, remote sensing, and satellite data. Indirect methods, such as the use of soil electrical properties, have become popular (Calamita et al., 2012) Soil electrical properties depend on the soil structure and soil moisture content (Romero-Ruiz et al., 2018; de Melo et al., 2021). To convert these electrical measurements to moisture content, the Archie (1942) equation presented in Eq. (3-18) has been shown to provide a good estimate of soil moisture (Roodposhti et al., 2019; Tso et al., 2019). The Eq. (3-18) was given in terms of electrical conductivity. Therefore, electrical resistivity measurements at the site were converted to electrical conductivity and subsequently used to estimate the volumetric water content.

$$\theta = \left(\frac{EC_t}{EC_w} \cdot p \cdot \varphi^{q-r} \right)^{\frac{1}{q}} \quad (3-18)$$

where EC_t is the bulk electrical conductivity; EC_w is the electrical conductivity of pore water taken to be 1 mS/cm; p is the tortuosity factor; q is the saturation exponent factor; r is the cementation factor; and φ is the porosity of the soil.

The porosity of the soil, φ is calculated as:

$$\varphi = 1 - \frac{S_G \cdot \gamma_w}{\gamma_b} \quad (3-19)$$

where γ_w is the unit weight of water.

Figure 3-11 presents the two porosities acquired at Area 2 of the field site, specifically at Y=12.8 m, utilizing Rosetta (θ_s) and the porosity derived from the bulk unit weight (as per Eq. 3-17). It is evident that although the two porosities may exhibit different trends, with the porosity from Rosetta increasing with depth whereas the porosity from shear wave velocity tends to decrease after a depth of 0.3m, they both fluctuate within the porosity range of 0.33 to 0.39.

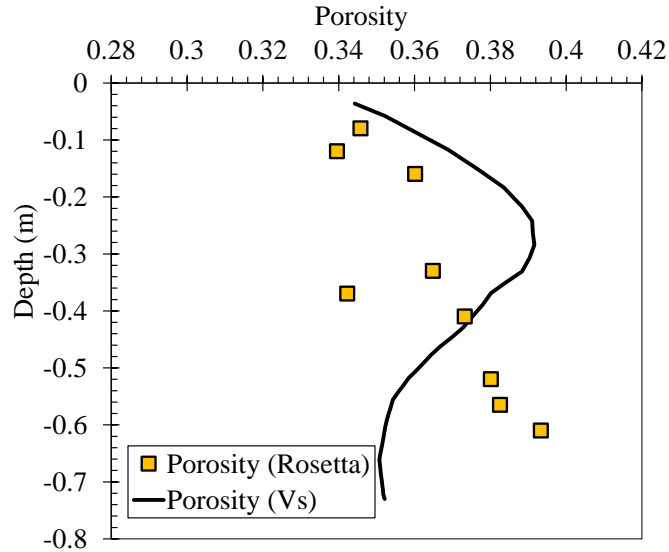


Figure 3-11 Comparison of porosities derived from Rosetta and shear wave velocity.

Table 3-8 presents the coefficients obtained from optimization using the least squares based on general numbers reported by Roodposhti et al. (2019) for Archie's equation. These coefficients fall within the ranges of $0.5 < p < 1.5$, $1 < q < 2.5$, and $1.4 < r < 2.5$. The range of values of q remained consistent at 2.5 across the three study points, indicating similar moisture content. However, there were notable differences in the p and r values. The p values exhibited no discernible pattern, with Area 2 having the lowest values, followed by an increase in Area 1, and then Area 3, possibly attributed to the convoluted flow of water through soil pores. Conversely, the r values increased from Area 1 to Area 3, and then to Area 2, possibly reflecting differences in compaction levels across the three areas.

Figure 3-12 illustrates that as the electrical conductivity of the soil increases, using Area 2 at $Y=12.8$ m, the volumetric water content also increases with depth. This is because the increasing presence of moisture in the soil space results in increasing conductivity of the soil. However, it should be noted that the variation in the volumetric water content primarily stems from the soil structure, mainly porosity, as presented in the Archie equation.

Table 3-8. The fitting parameters for Archie (1942) equation for the three study points of the field site.

Area	Position	p	q	r
Area 1	Y = 3.3 m	1.462	2.5	1.000
Area 2	Y = 12.8 m	0.500	2.5	2.445
Area 3	Y = 23.8 m	1.500	2.5	2.272

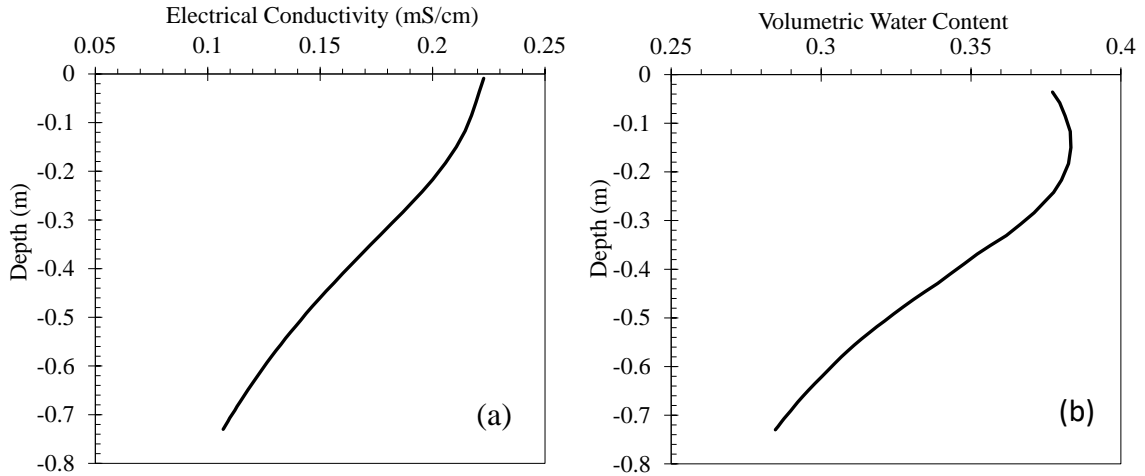


Figure 3-12 Variation of moisture conditions with depth. (a) electrical conductivity; (b) volumetric water content from Archie' equation.

3.4.3 Performance Evaluation of the Modified G-suction Equation at the Field Site

Figure 3-13 illustrates a comprehensive comparison between the measured and predicted small-strain shear modulus obtained through field measurements of shear wave velocity and the application of the modified G -suction equation outlined in Eq. (3-16). It is worth noting that data collected at near the ground surface, particularly up to a depth of 0.2 m, was found unreliable due to inherent errors associated with dispersion curve fitting at the highest frequencies (Adama et al., 2023). These errors stem from the difficulty in defining the first higher modes of surface waves accurately, leading to reliance solely on the fundamental mode for the inversion process. Additionally, considering the shallow depth of investigation, residual vibrations at the surface from movements in the vicinity of the investigation area could contribute to this error.

In Area 2 (Figure 3-13 (b)), the predicted data showed satisfactory agreement after the dispersion error zone, extending up to the natural ground. This area had the highest compaction among the three areas, as shown in Figure 3-10 by the shear wave velocity and bulk density. Conversely, in Area 1 (Figure 3-13 (a)), the measured data showed significant variation, ranging from 20 MPa to 60 MPa, while the predicted data ranged from 20 MPa to 40 MPa. In Area 3, the measured data ranged from 10 MPa to 30 MPa, while the predicted data ranged from 25 MPa to 50 MPa. Notably, the predicted data was shown to overpredict for Area 1, whereas the predicted data for Area 3 was shown to underpredict the measured data but exhibit a similar pattern and ultimately converge at the natural ground level.

It is important to note that the offset of the predicted data for both Areas 1 and 2 was approximately 10 MPa from the measured data. This trend in the predicted data behavior for the three areas may be because of the level of compaction of the three areas with Area 2 shown to have a higher compaction than Area 3 followed by Area 1 as shown in Figure 3-10. Therefore, the proposed model may overpredict or underpredict the measured data based on the level of compaction. Thus, the model should be utilized with engineering judgment when applied in field conditions. As a result, future research should study the influence of compaction effort or bulk density on the proposed model on field conditions. Overall, Figure 3-13 provides valuable insight into the performance of the modified G -suction model to match closely to the measured data but may exhibit variation based on the compaction effort.

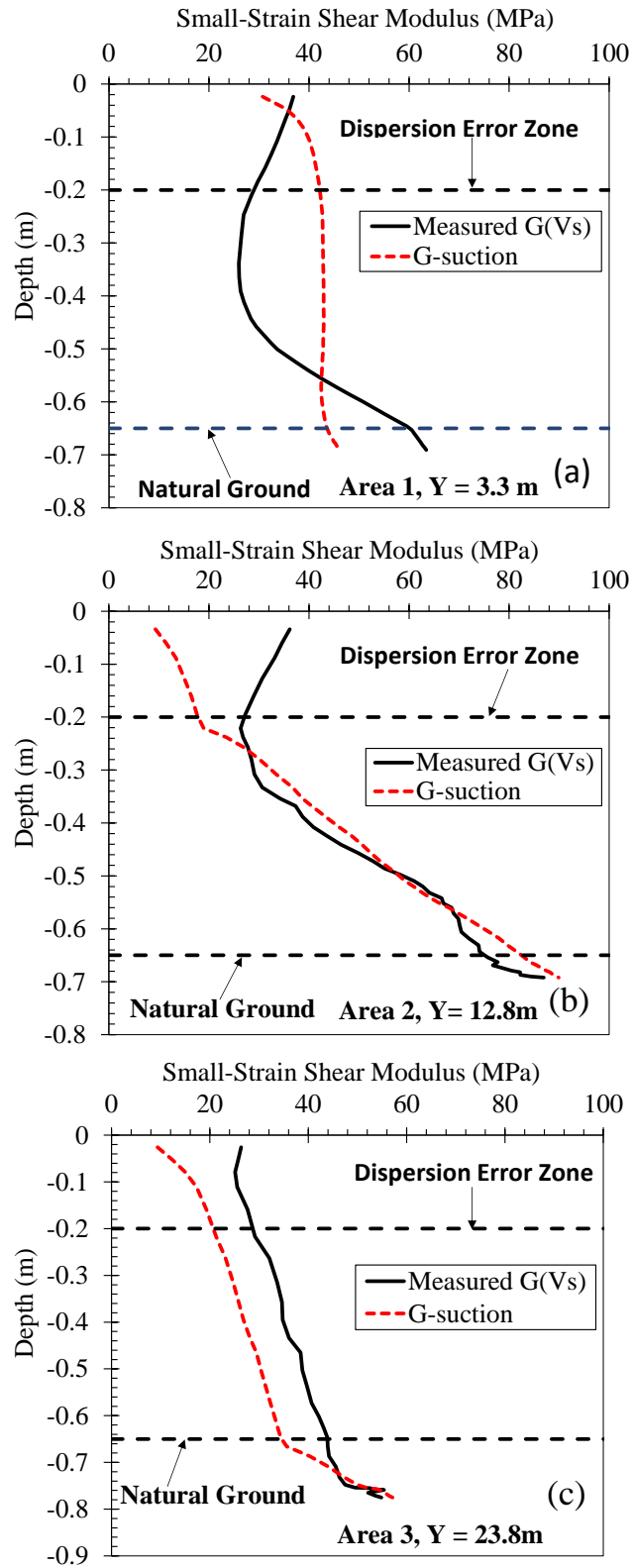


Figure 3-13 Performance of the modified G-suction model in predicting the small-strain shear modulus at the three study points with depth.

CHAPTER 4. SUMMARY AND CONCLUSIONS

Chapter 2 presents a novel approach for the prediction of the small-strain shear modulus and shear strength of unsaturated soils, based on the inverse relationship with the soil-water characteristic curve. The proposed equations demonstrate a good agreement between measured and predicted mechanical behavior across various soil properties, net normal stresses, and matric suctions up until the residual zone of the SWCC. Given the importance of the initial saturated small-strain shear modulus in the proposed model, this study calibrated the Hardin and Black (1969) equation based on measured literature data. This calibration extends its applicability to estimating saturated small-strain shear modulus for various soil types ranging from silts to clays and sands. In the case of shear strength, the classical Mohr-Coulomb equation was recommended.

Efforts to establish a correlation for the scaling function, β showed promising results with the air-entry value (AEV). For the small-strain shear modulus, employing 13 literature soils led to the establishment of two predictive equations tailored to soils with AEV below 100 kPa and those equal to or exceeding 100 kPa, respectively. Additionally, an equation was developed for shear strength drawing on data acquired from triaxial and direct shear tests for 13 literature soils. The proposed G -suction and τ -suction β values were tested for hysteretic effects to investigate the behavior of such conditions on β . The study revealed that the β values for the drying path for the small-strain shear modulus was lower than the wetting path, while the opposite held true for shear strength.

Acknowledging the variability in testing techniques for small-strain shear modulus, predominantly with bender elements or resonant column tests, and for shear strength, encompassing drained and undrained triaxial and direct shear tests, the predictive equation for β demonstrates commendable accuracy in estimating small-strain shear modulus and shear strength for unsaturated soils when used in the general G -suction and τ -suction equations. However, it is imperative to exercise caution and employ engineering judgement when utilizing the predictive equations for β in the absence of measured data. It is recommended that the proposed model should be further investigated for the residual zone

of the SWCC, while exploring potential correlations with material properties or stress conditions.

In chapter 3, the performance of a proposed model developed from the inverse relationship between the small-strain shear modulus and the soil-water characteristic curve (SWCC) from small laboratory samples to a large-scale box. The test soils, consisting of sand and clay from Kentucky, were placed in the box at four different densities. The test box was installed with sensors to measure volumetric water content, matric potential and electrical conductivity. In addition, accelerometers were installed to receive seismic waves for the determination of shear and compressional waves. This allowed for measured small-strain shear modulus data to be predicted for using the proposed G -suction model. The model was modified to account for varying conditions between small laboratory samples and large-scale compacted soil.

Finally, the modified model was assessed on a field site using the saturated small-strain shear modulus equation derived from the modified Hardin and Black (1969) equation, along with SWCC fitting parameters obtained from Rosetta. Volumetric water content at the field site was estimated from electrical resistivity using the Archie (1942) equation, enabling the calculation of the effective degree of saturation. The predicted data showed satisfactory agreement with the measured data at the field site. Overall, the study demonstrates the effectiveness of the proposed model in predicting small-strain shear modulus for both small laboratory specimens and field data, providing valuable insights for preliminary geotechnical engineering analysis.

APPENDICES

APPENDIX A - INDEX AND MECHANICAL TESTS DATA

The geotechnical index properties of four Kentucky soils are presented in Table A-1. The initial electrical capacitance and resistance recorded during California bearing ratio (CBR) testing for the four soils is presented in Table A-2. The proctor compaction and CBR test results are shown in Figure A-1 and A-2, respectively. Also presented are the variation of capacitance and resistivity with displacement for the four soils as presented in Figures A-3 to A-6.

Table A-1 Geotechnical index properties of test soils.

Test soil	USCS	S_G	γ_d (kN/m ³)	ω_{opt} (%)	LL	PI	Fines (%)	Sand (%)
KY River sand	SP-SM	2.65	16.08	15.4	-	-	11.40	88.6
Hamburg clay	CL	2.64	15.96	20.8	33.3	12	91.55	8.45
Henderson clay	CL	2.69	17.90	12.9	28.2	8.5	98.58	1.42
Hybrid sample	-	2.70	19.50	11.4	-	-	17.06	82.94

NB: The γ_d and ω_{opt} are at standard proctor energy.

Table A-2 Electrical measurements taken during CBR testing.

Energy (kJ/m ³)	KY River sand		Hamburg clay		Henderson clay		Hybrid sample	
	Cp (pF)	Rp (k Ω)	Cp (pF)	Rp (k Ω)	Cp (pF)	Rp (k Ω)	Cp (pF)	Rp (k Ω)
300	7.29	0.611	16.29	0.469	-2.94	0.322	11.08	1.010
450	5.62	0.514	16.56	0.474	-1.87	0.362	10.21	1.300
600	3.64	0.485	17.55	0.476	-4.74	0.364	10.84	1.320
900	3.92	0.461	16.45	0.478	-4.42	0.387	9.47	1.850

Note: Cp is the capacitance; Rp is resistance.

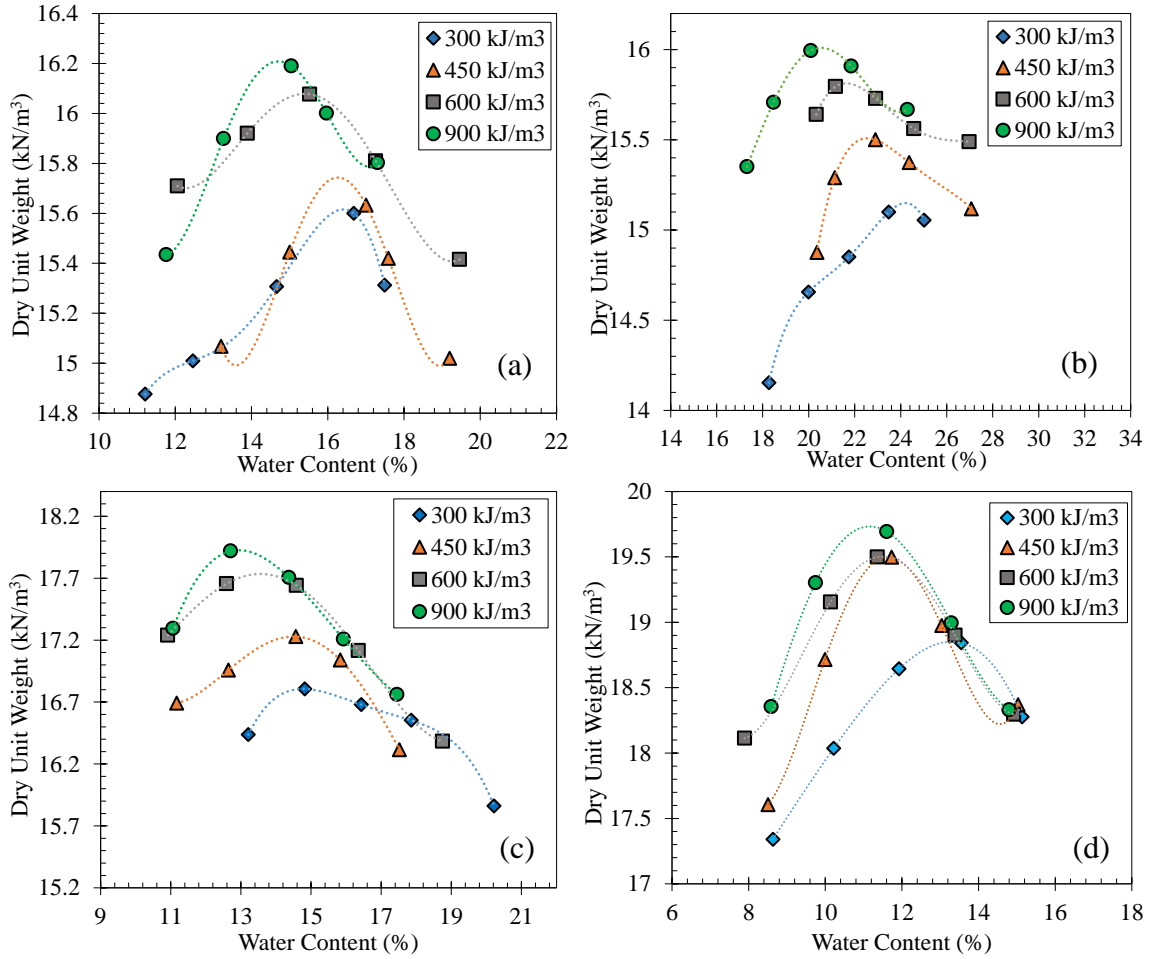


Figure A-1 Proctor test results at four different compaction energies. (a) KY River sand; (b) Hamburg clay; (c) Henderson clay; (d) Hybrid sample.

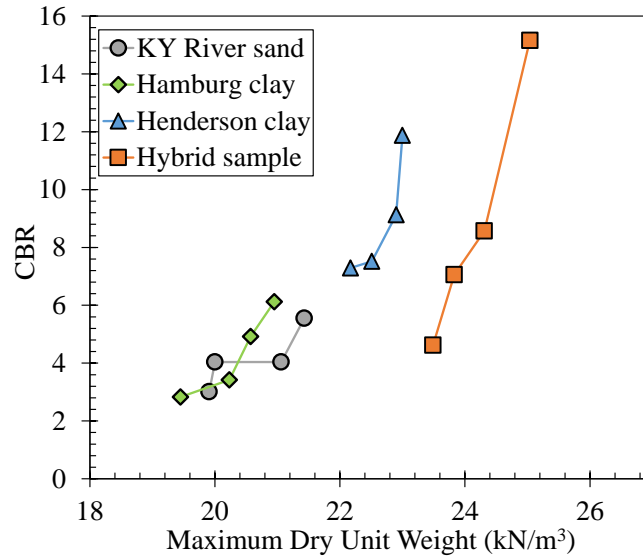


Figure A-2 Variation of CBR with maximum dry unit weight for the four test soils at four different energies.

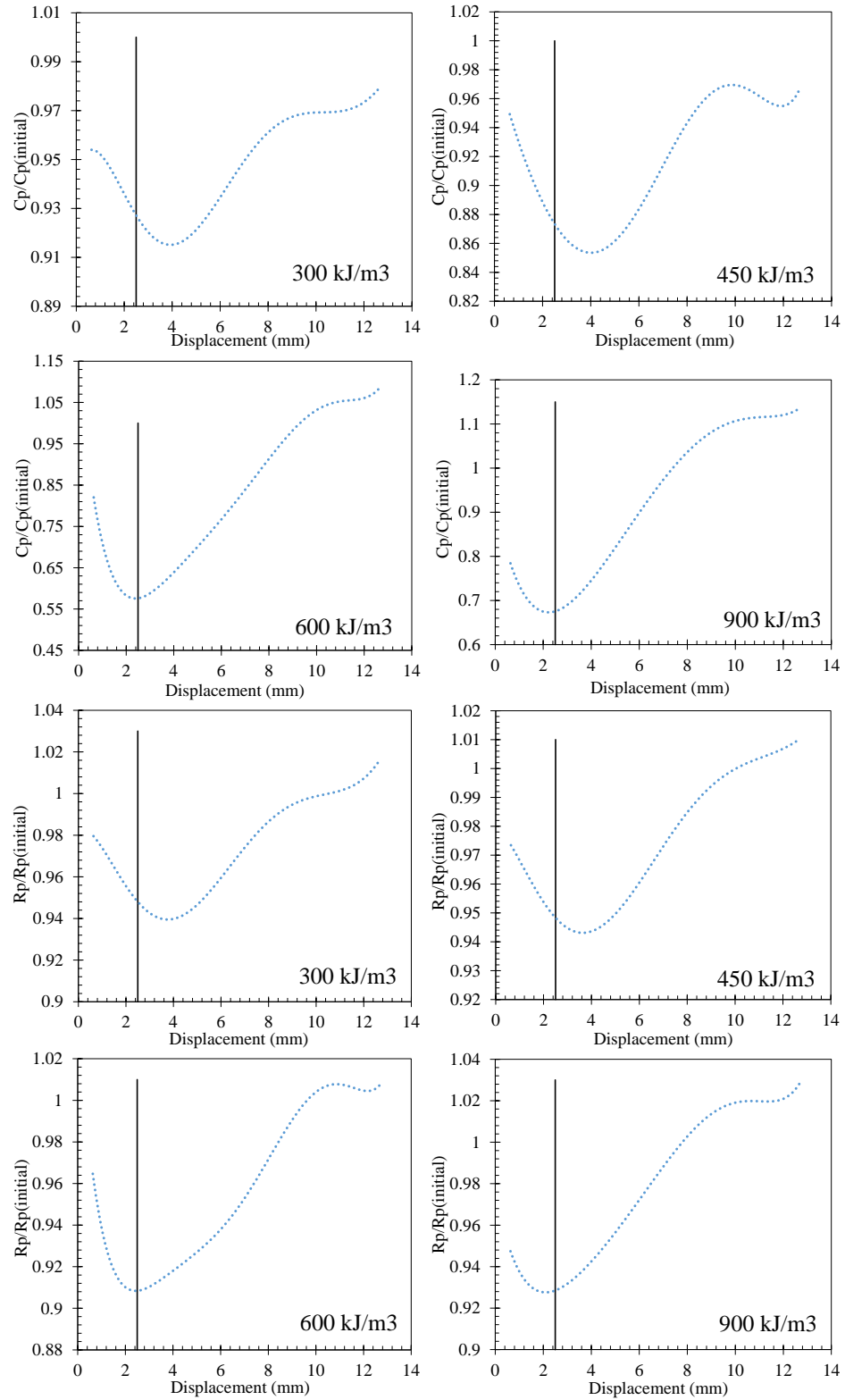


Figure A-3 Normalized capacitance and resistance for KY River sand with 2.54 mm displacement.

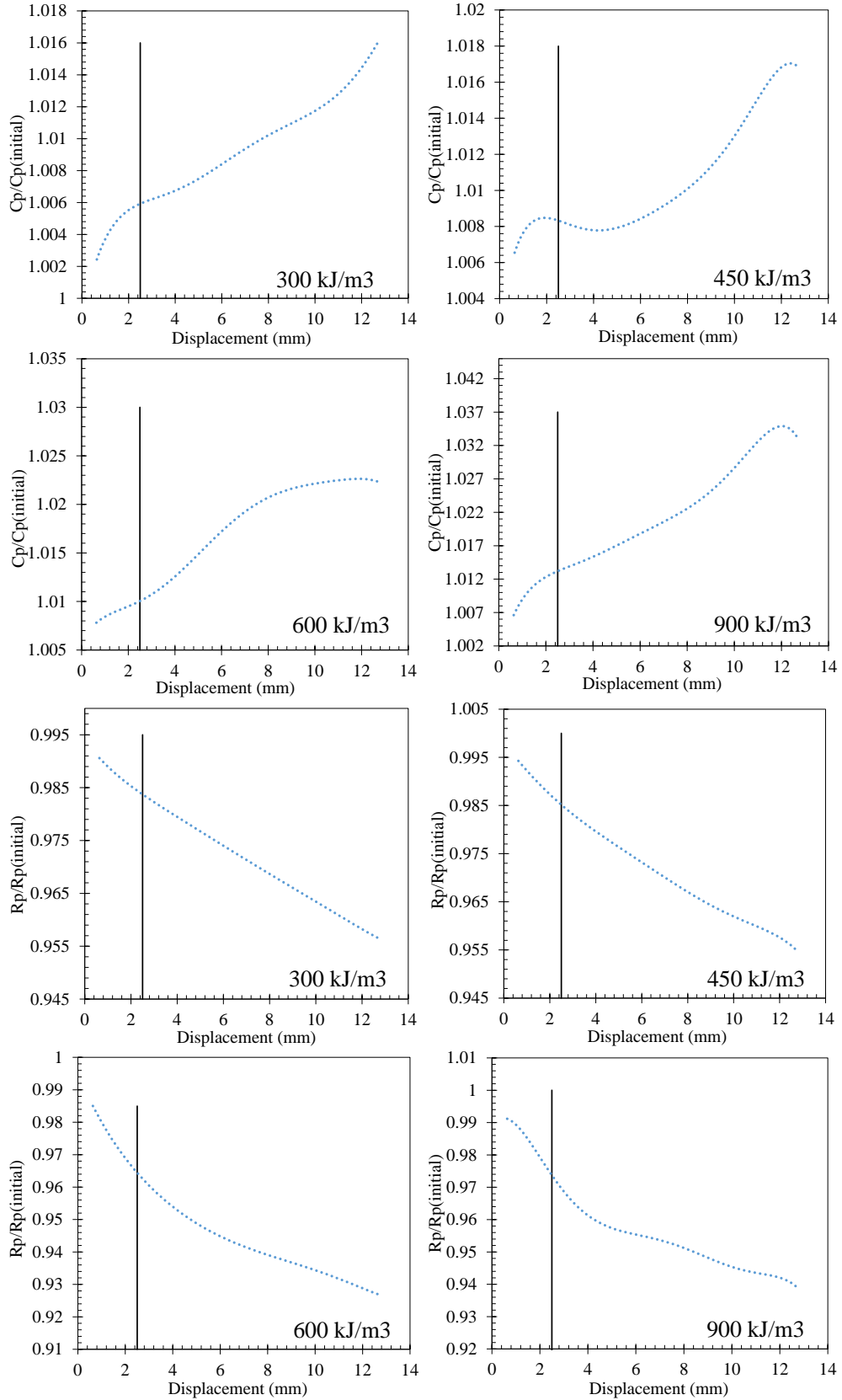


Figure A-4 Normalized capacitance and resistance for Hamburg clay with 2.54 mm displacement.

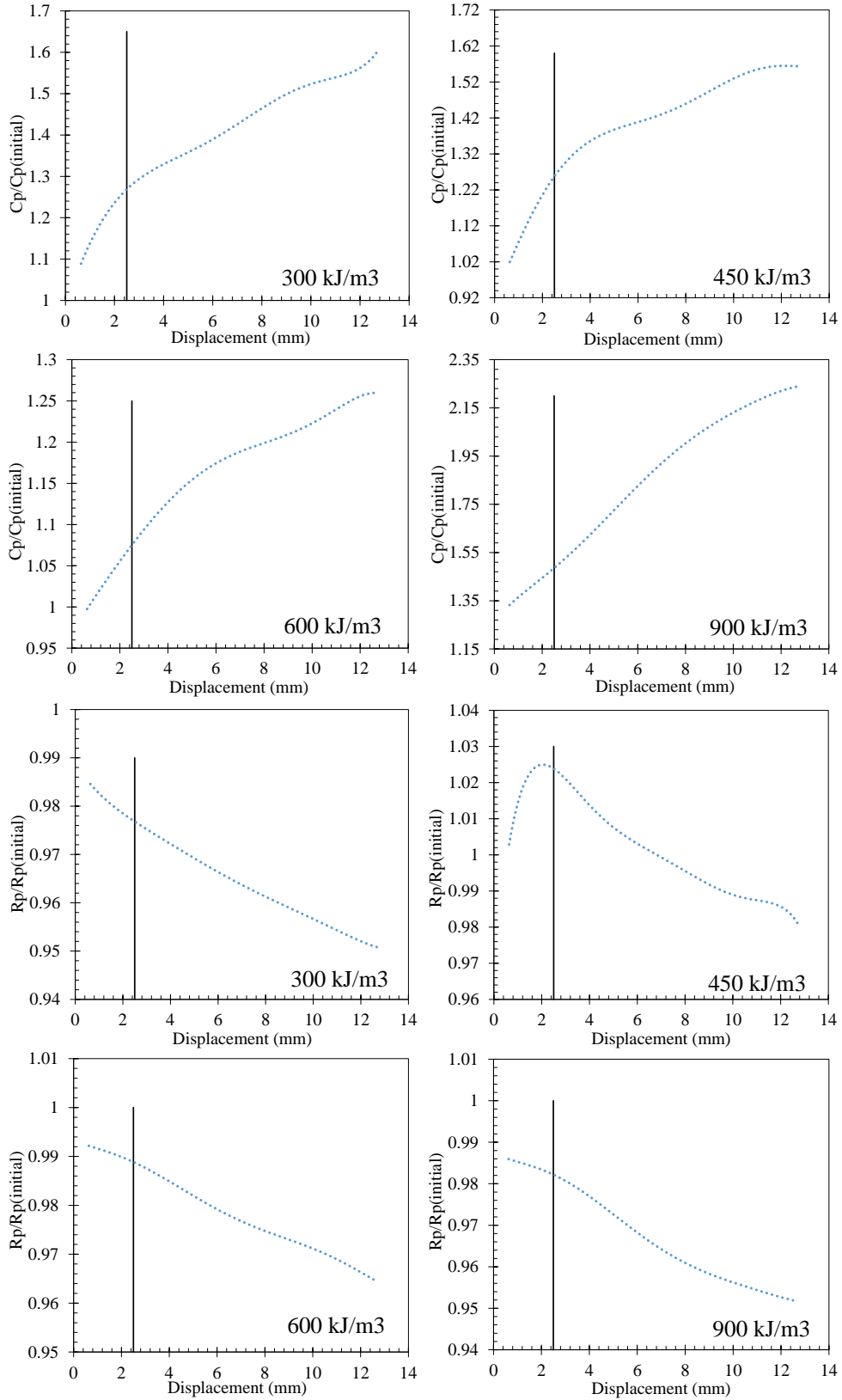


Figure A-5 Normalized capacitance and resistance for Henderson clay with 2.54 mm displacement.

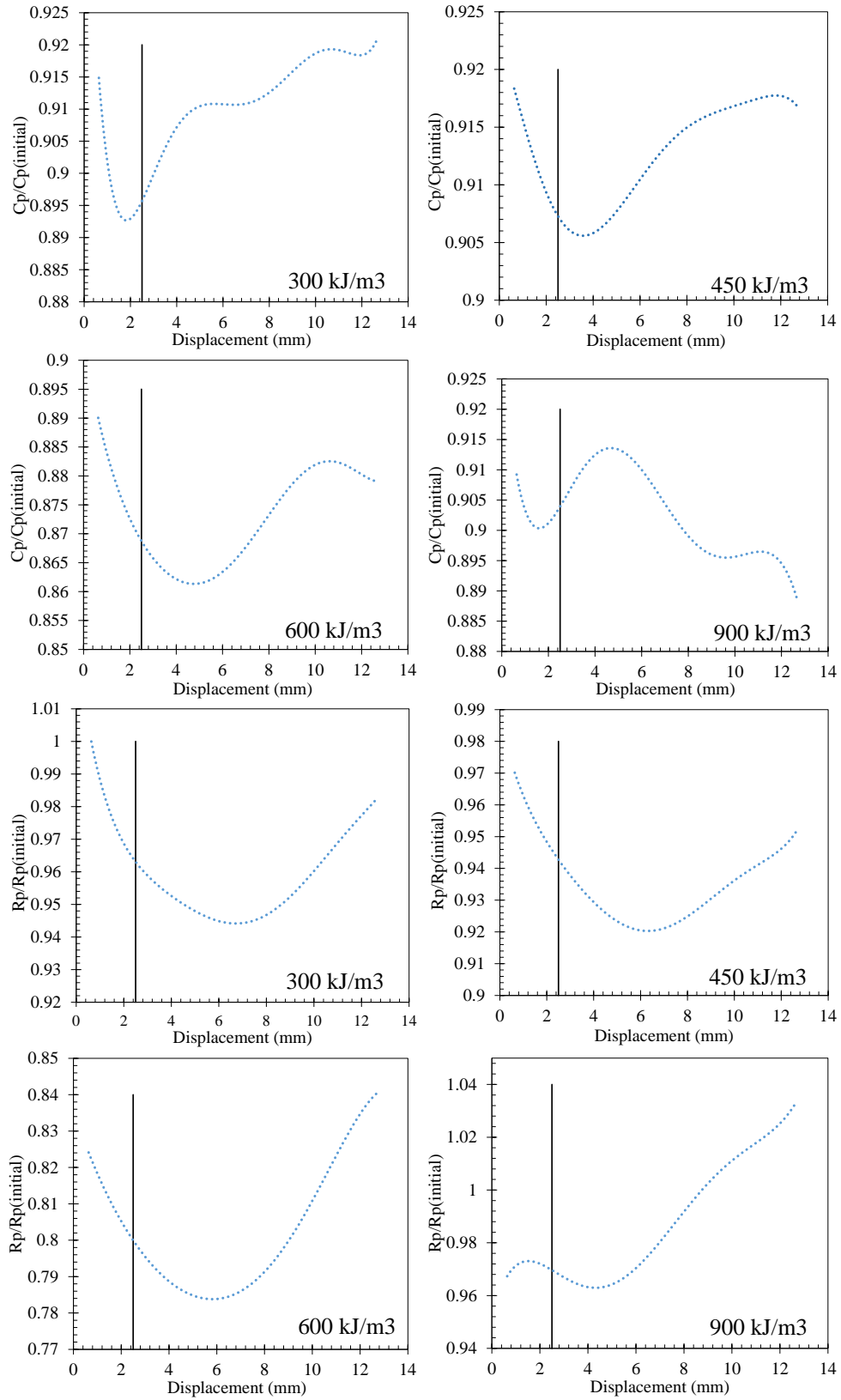


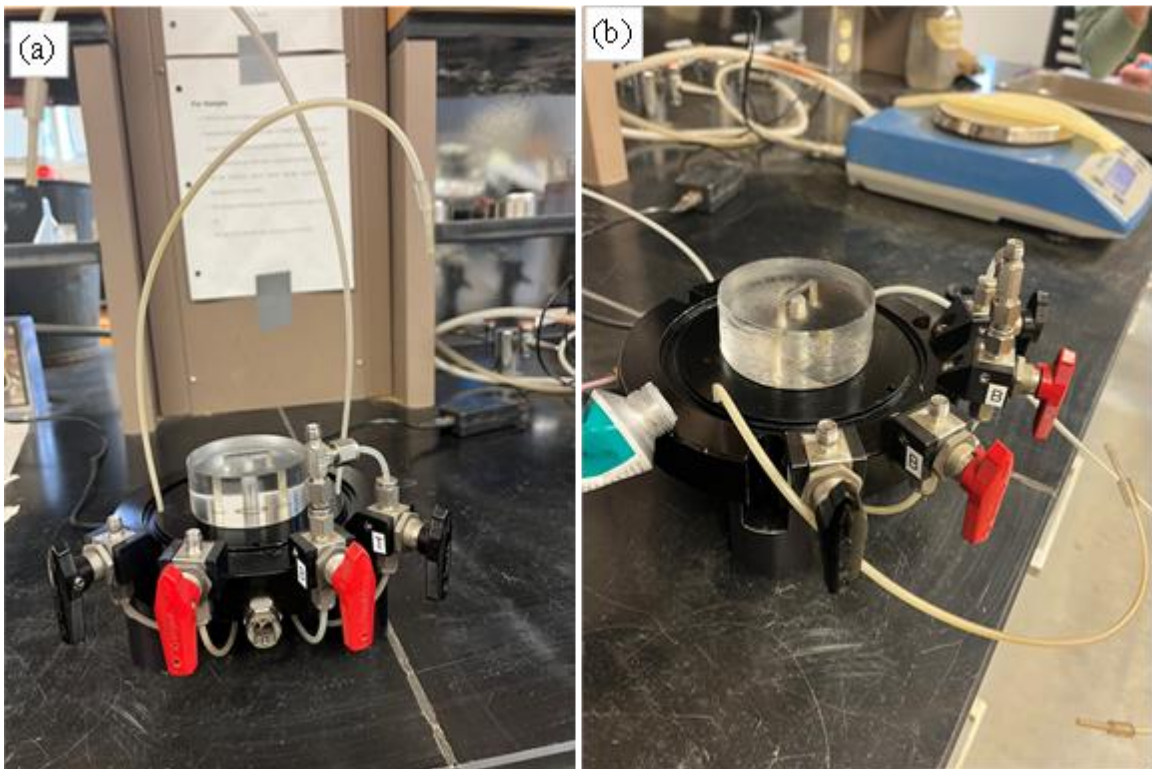
Figure A-6 Normalized capacitance and resistance for Hybrid sample with 2.54 mm displacement.

APPENDIX B - TRIAXIAL TESTING PROCEDURE

This section outlines the procedure for preparing sand and remolded clay samples for testing in a triaxial cell. Triaxial testing is performed using the Geocomp LoadTrac-II/FlowTrac-II system. This system fully automates the triaxial testing. Once the sample is prepared and in place with the testing conditions selected. The sample preparation for sand and remolded clay samples and their setup in the triaxial cell will be shown here. Additionally, the testing conditions employed will be explained. Specifically, the remolded clay sample is prepared using the Durham S-242 Compactor/Extruder.

Below are the steps detailing the preparation of sand samples, their setup within the triaxial cell, and the testing conditions:

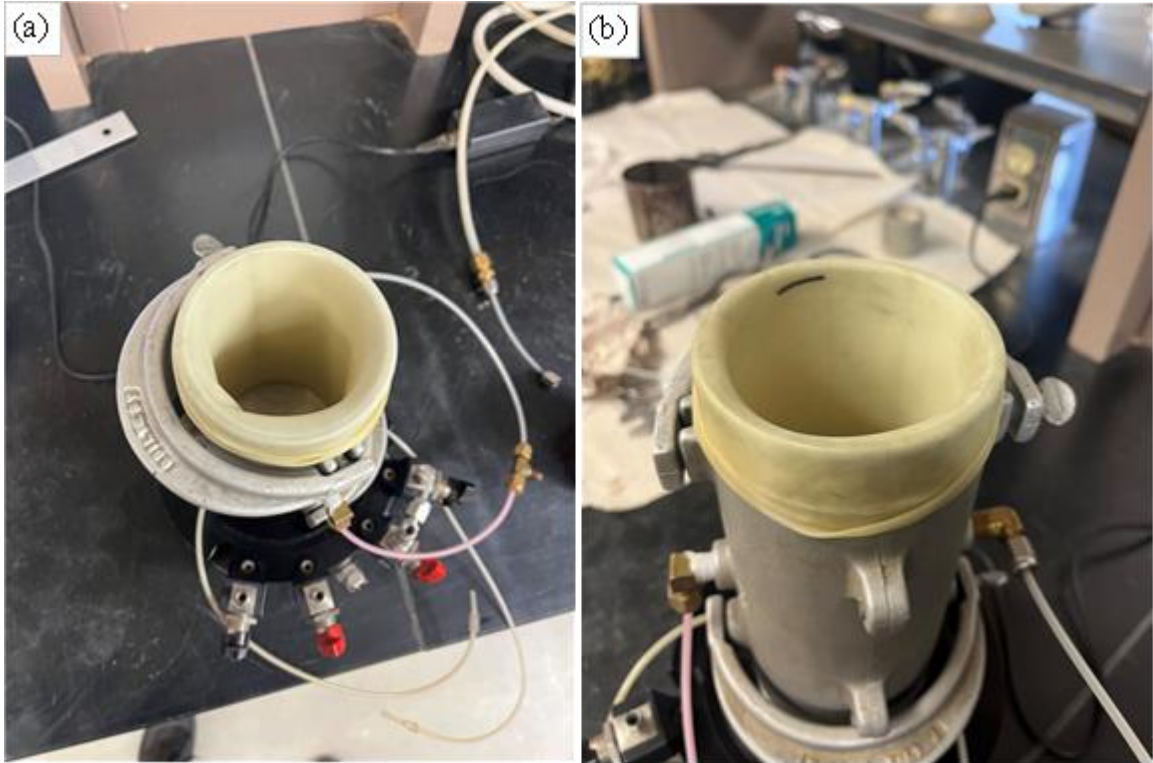
Step 1: Ensure thorough cleaning and drying of both the pedestal's base cap and the cell. Following this, apply a layer of vacuum grease around the base cap to facilitate optimal sealing:



Step 2: Place a wet porous stone and filter paper atop the base cap of the pedestal. Subsequently, position a membrane and secure it with two O-rings to ensure a tight seal:



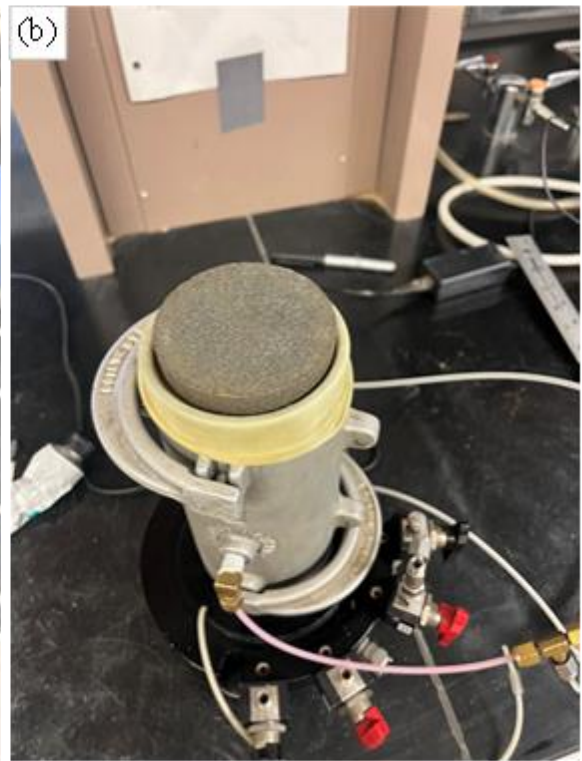
Step 3: Position a split mold and wrap the membrane around its top edge. Connect it to a vacuum source to secure the membrane in place. Proceed to mark the required specimen height on the membrane, typically 5.6 inches for clay and 6.0 inches for sand:



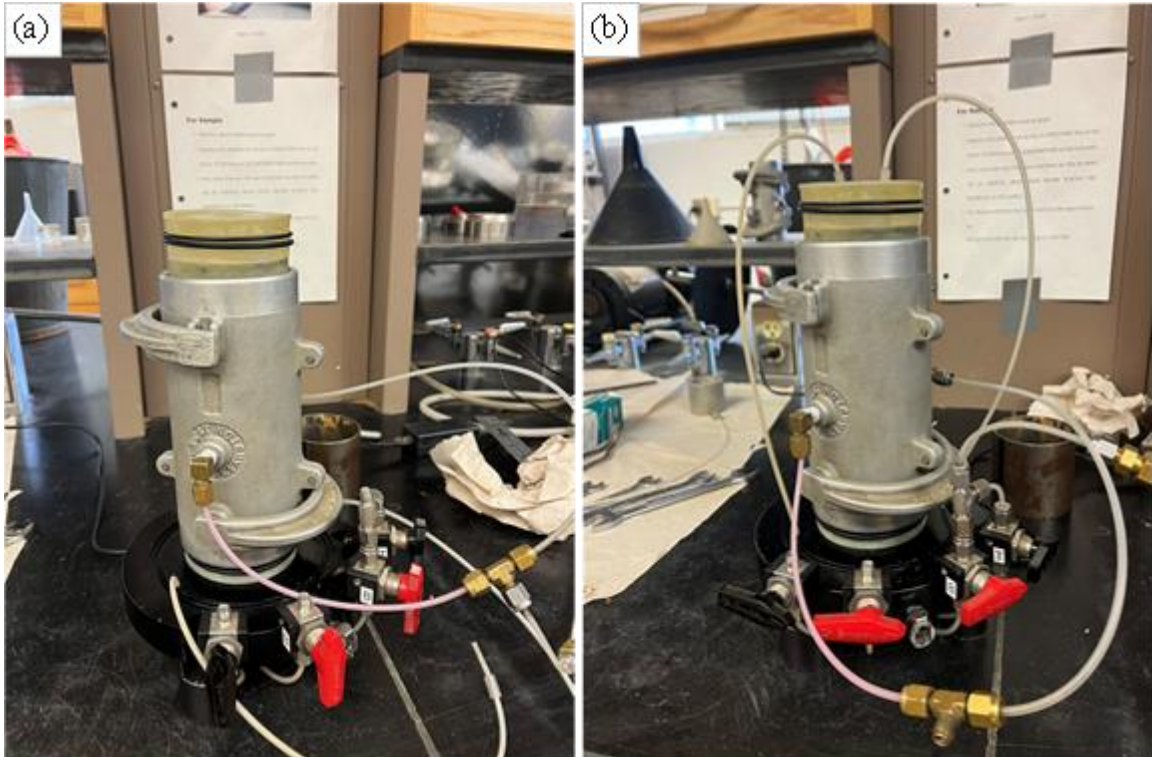
Step 4: A sand sample, either air-dry or oven-dry, is utilized but dampened to prevent dust particles during compaction in the mold. Compaction is carried out in lifts as determined by the tester, ensuring uniformity and measured using spoon counts.



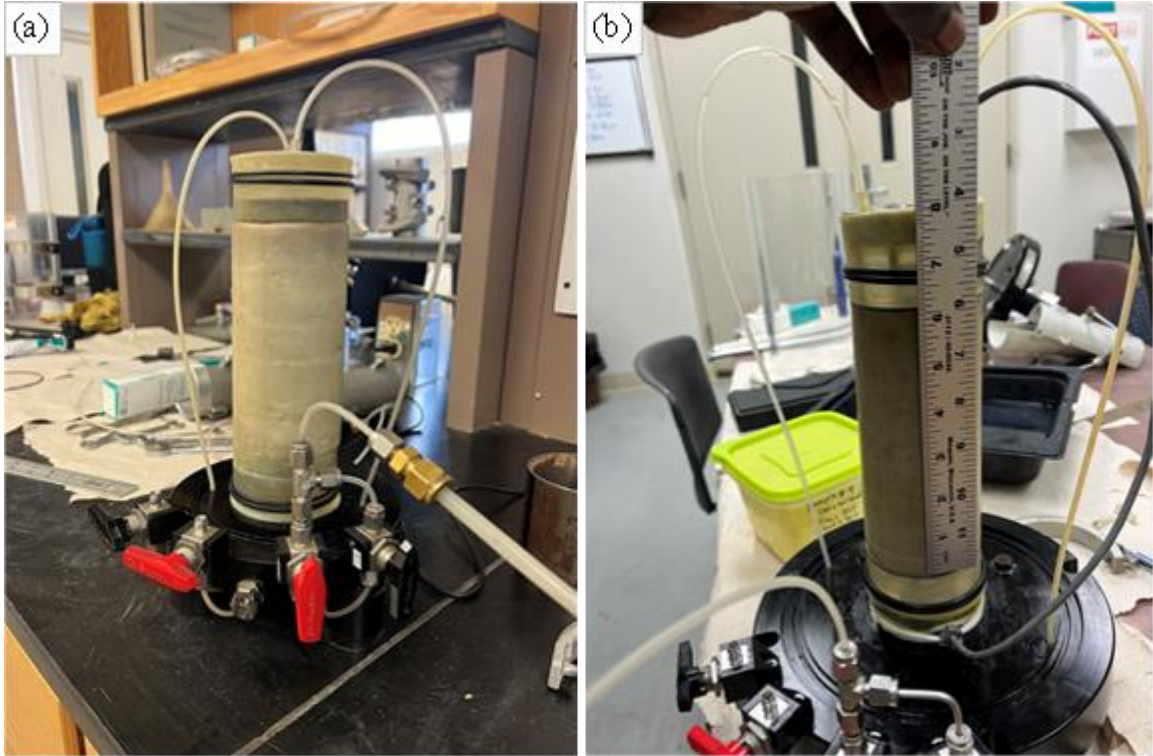
Step 5: The filter paper and porous stone, which can be wet or dry at this stage, are placed on the specimen in the specified order:



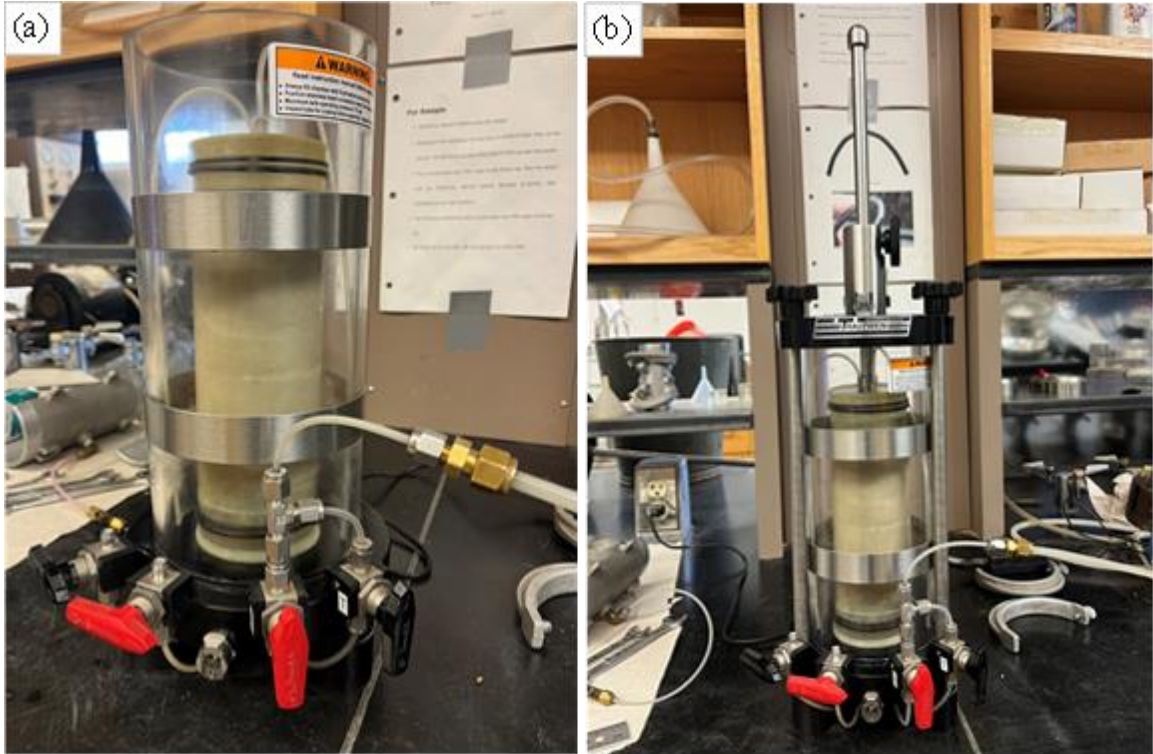
Step 6: The top cap is positioned onto the porous stone, and vacuum grease is applied to the top cap. Subsequently, the membrane is rolled over the top cap, and two O-rings are placed on the membrane to ensure a tight seal. This prevents water from seeping into the specimen or vice versa. The valves on the base pedestal can either be opened or closed, as it is not connected to vacuum or water. The top tubes connected to the base pedestal are then attached to the top cap, as illustrated below:



Step 7: Next, vacuum is transferred from the split mold to the sample on the bridge of the base pedestal. Note: If the sample is highly saturated, connect a vacuum water trap to collect the water from the sample rather than sending it to the house vacuum. Open both the top and bottom valves on the bridge simultaneously to secure the sample. However, ensure that the other two valves are closed before connecting the vacuum:



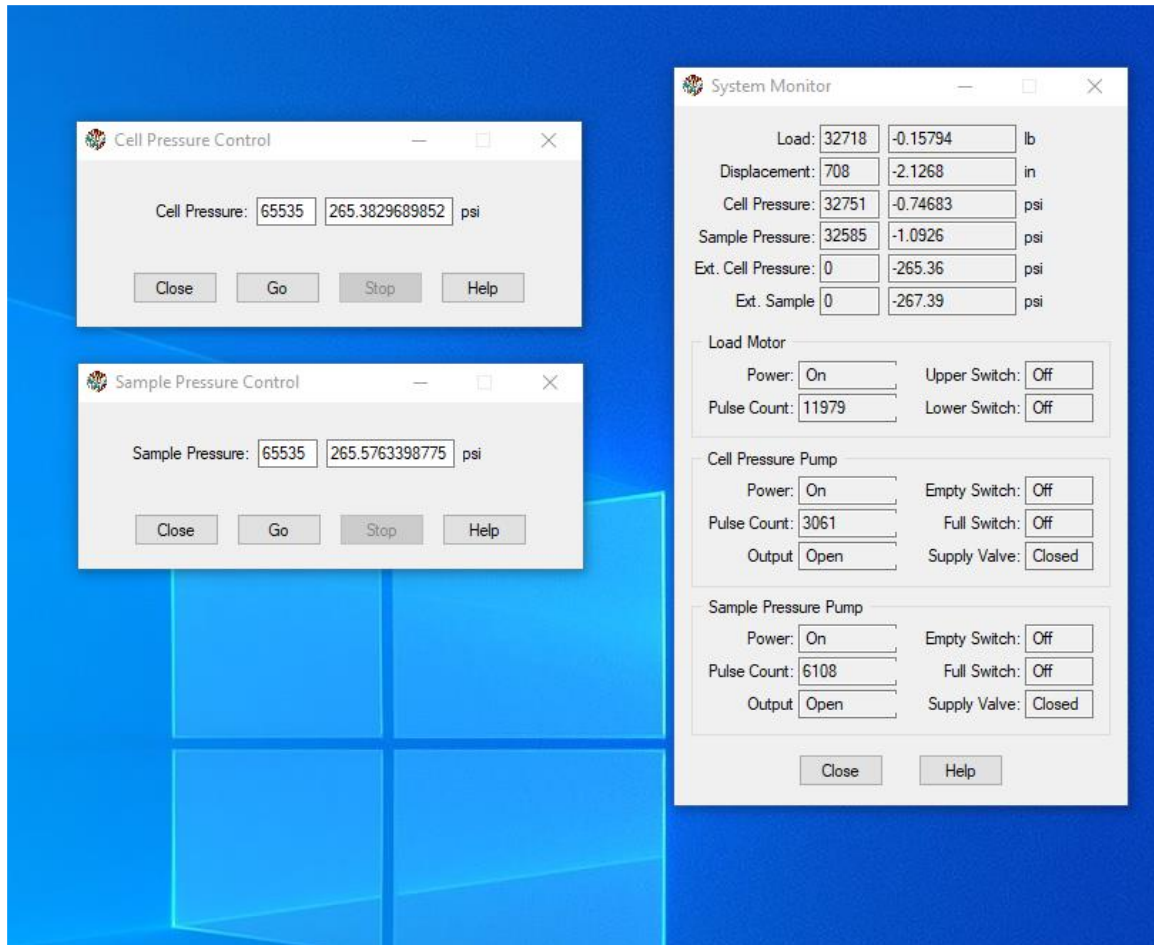
Step 8: At this stage, separate the split mold. Then, ensure the base pedestal is free from any grit or moisture. Use a vernier caliper to measure the diameter and a ruler to measure the height of the sample at the top, middle, and bottom. Calculate the averages. Next, place an O-ring on the base pedestal and apply vacuum grease to seal it. Position the chamber over the triaxial base pedestal, ensuring it rests on the O-ring. Place the top pedestal with a fitted O-ring on the chamber after applying vacuum grease to securely seal the chamber with the rods. The sample remains connected to the vacuum at this point:



Step 9: Place the sample on the platen of the load frame. Attach a quick connect to a running tap water source and fill the chamber with water as demonstrated ensuring you have an air vent on the top pedestal to avoid the accumulation of pressure in the chamber. The sample is still connected to vacuum at this point:



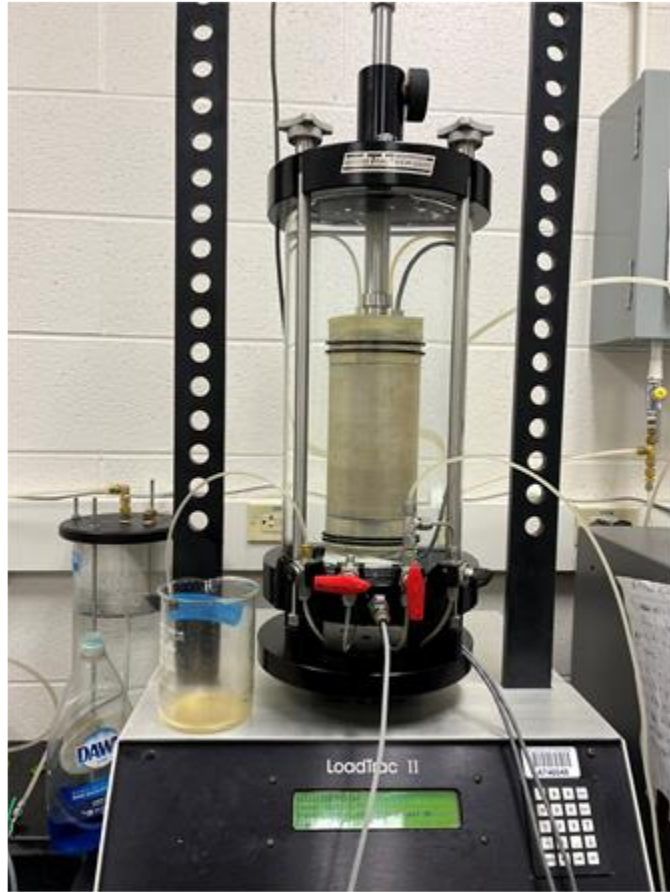
Step 10: Launch the TRIAXIAL application. The software has been calibrated and requires no further modifications. Zero cell pressure and sample pressure to initiate the test. Navigate to the **View Tab > System** to access the System Monitor. Then, proceed to the Control Tab and click on the sample pressure and cell pressure to open the respective tabs as demonstrated:



Step 11: In the cell pressure and sample pressure pump screens, select Control, then Jog to allow water to flow out through the output valve, ensuring it is saturated and void of air. After a few drops, stop the jogging water. Position the tip of the cell pressure at the center of the sample, then adjust the offset value in the cell pressure control on the computer screen to match what is displayed on the System Monitor to zero the pressure in the cell pressure pump. Connect the cell pressure to the sample and input a cell pressure of 3 psi before hitting "Go". Disconnect the vacuum and close the valves on the bridge. Repeat the procedure to zero the sample pressure. Enter a pressure of 2 psi for the sample pressure. Before opening the valve to flush drain lines and flood the sample, adjust the cell pressure to 5 psi.

Step 12: First, open the two bottom valves to flush the drain line under the sample pressure of 2 psi. Subsequently, close the valves, and repeat the procedure for the top valves. Once the drain lines are flushed, open the bottom valve on the bridge and the top valve to allow

water to flood the sample for 2-3 pump cycles. After these cycles, the sample is now prepared for testing. Typically, the cell pressure pump is filled up to full capacity before beginning the jogging stage in Step 11. However, for the sample pressure pump, it is filled up to 50% for CD tests and 70% for CU tests:



The testing parameters are configured as follows:

Step 13: In the TRIAXIAL application, navigate to the **Project** page and input the details of the project, including the sample name and a description of the testing conditions:

TRIAXIAL - C:\Users\lac225\Documents\LUCAS TRIAXIAL TESTS\TRIAXIAL\KY Riversand\Undrained\96 pcf\30 psi consolidation\... □ ×

File View Run Calibrate Control Report Options Help

Project	Saturation	Consolidation/B Table		Shear Table	
Specimen	Water Content	Read Table	Test Parameters	Initialization	Consolidation/A Table
Project Number: <input type="text"/>	Project Name: <input type="text" value="KY Riversand"/>	Client: <input type="text" value="University of Kentu"/>			
Location: <input type="text" value="Kentucky"/>	Depth: <input type="text"/>	Elevation: <input type="text"/>			
Boring Number: <input type="text"/>	Sample Number: <input type="text"/>	Test Number: <input type="text" value="1"/>			
Preparation: <input type="text"/>	Classification: <input type="text" value="Riversand"/>	Group Symbol: <input type="text"/>			
Tester: <input type="text" value="Tanner"/>	Test Date: <input type="text" value="04/04/2024"/>	Checker: <input type="text" value="Dr. Bryson"/>	Check Date: <input type="text"/>		
Description: <input type="text" value="20 psi for 95 pcf density"/>	Remarks: <input type="text"/>				
Comments: <input type="text"/>					

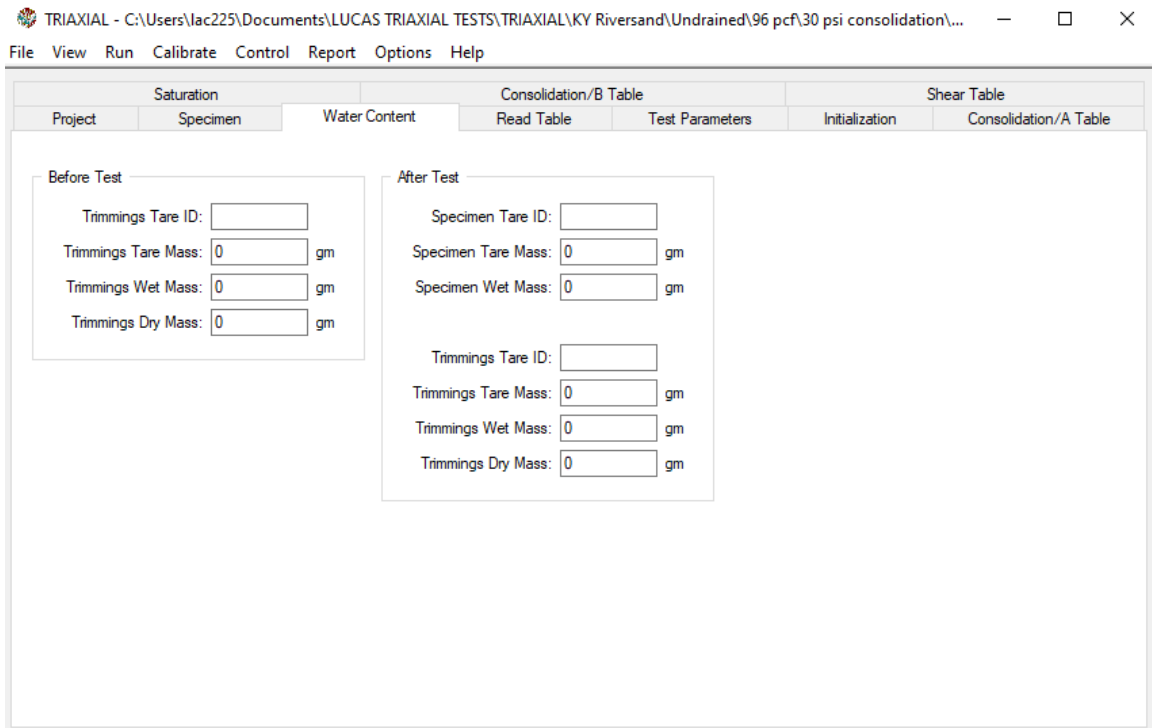
Step 14: Proceed to the **Specimen** page, where you will enter the physical attributes of the specimen. For clay and silt, select "plastic " and input the liquid limit and plastic limit values if applicable. However, for sand, select "non-plastic" as shown:

TRIAXIAL - C:\Users\lac225\Documents\LUCAS TRIAXIAL TESTS\TRIAXIAL\KY Riversand\Undrained\96 pcf\30 psi consolidation\... □ ×

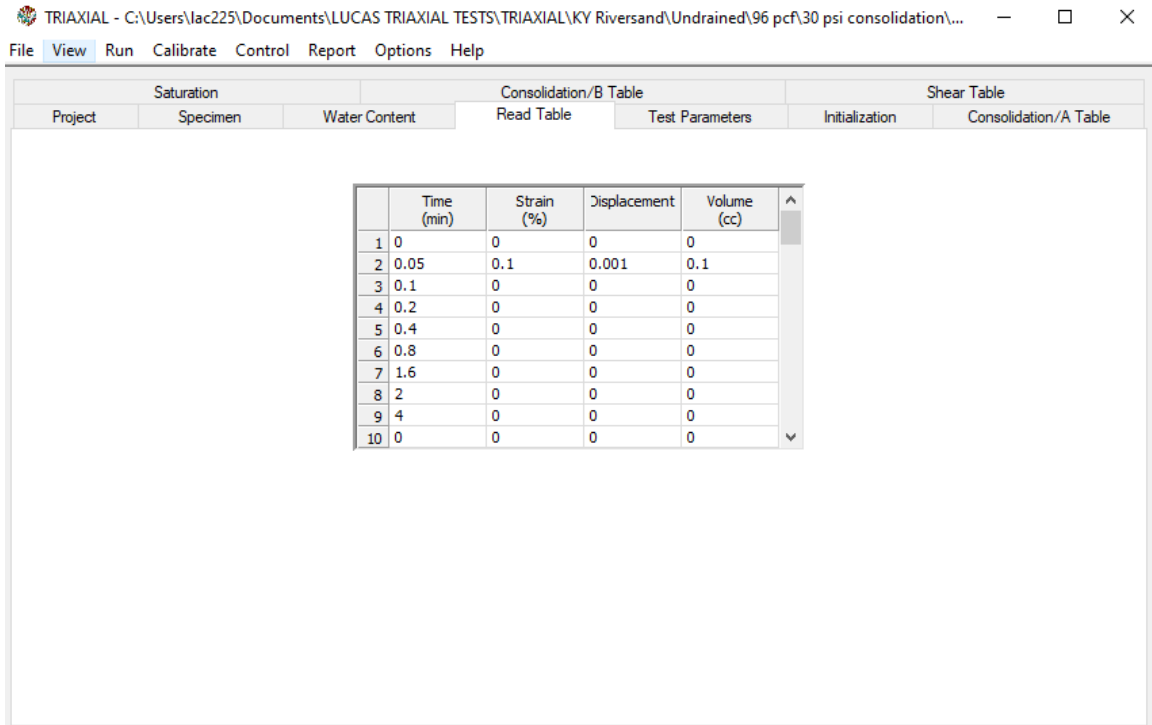
File View Run Calibrate Control Report Options Help

Project	Saturation	Consolidation/B Table		Shear Table	
Specimen	Water Content	Read Table	Test Parameters	Initialization	Consolidation/A Table
Initial Diameter: <input type="text" value="2.8"/> in					
Initial Height: <input type="text" value="6"/> in					
Initial Sample Mass: <input type="text" value="926"/> gm					
Specific Gravity: <input type="text" value="Measured"/> <input type="text" value="2.66"/>					
Plasticity: <input type="radio"/> Plastic <input checked="" type="radio"/> Non-Plastic <input type="radio"/> Unknown					
Liquid Limit: <input type="text" value="0"/>					
Plastic Limit: <input type="text" value="0"/>					

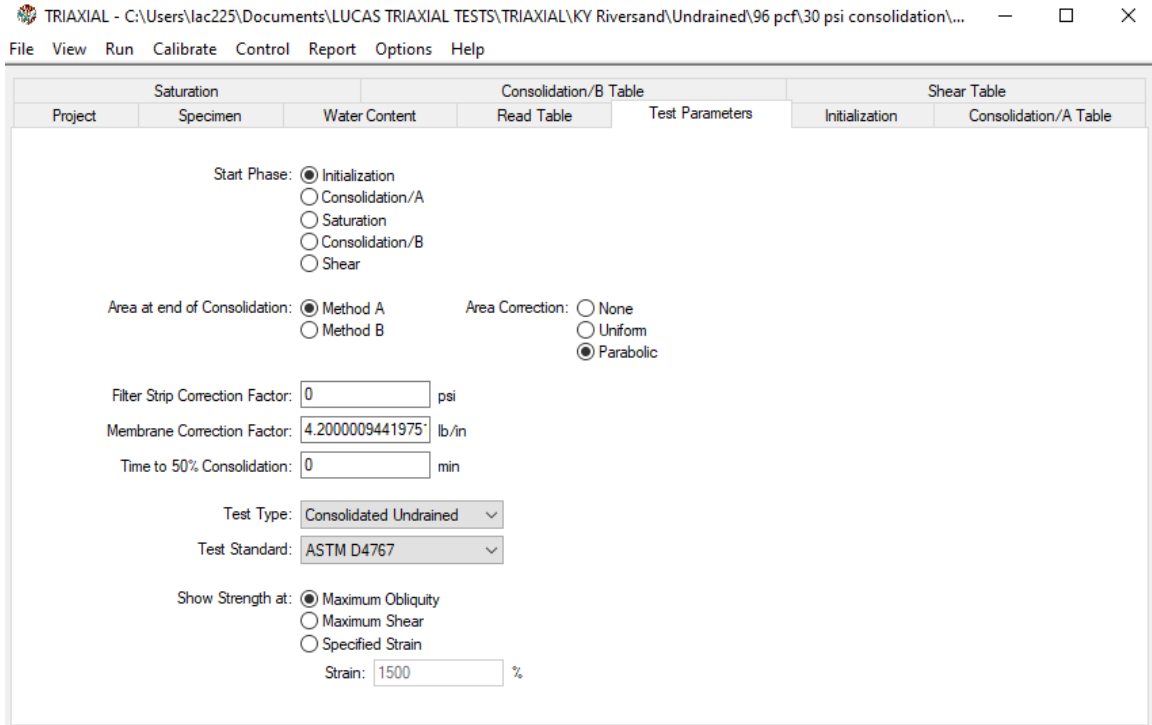
Step 15: For a sand sample, leave the **Water Content** page blank, as demonstrated below. If you prepare a remolded clay sample, you will know the approximate water content you placed in the soil, thus this page can remain blank. However, if you work with a Shelby tube non-disturbed sample, fill in the details of this page by taking trimmings before testing and placing them in the oven:



Step 16: The **Read Table** is employed to manage when the various sensor outputs are read and stored during testing, as illustrated below. Controls are time-based for the consolidation phase and strain-based for the shear phase. The read table presented is applicable for both drained and undrained conditions:



Step 17: The **Test Parameters** page, as depicted below, serves to control the test and parameters utilized for data correction. The test commences at the Initialization phase. For the area at the end of consolidation, two methods provided by ASTM are available: Method A, which computes the area based on measured volume change, and Method B, based on the final water content of the specimen. Method A is employed for all testing conducted. Area correction is executed based on a parabolic shape since the sample is loaded axially and expands radially in accordance with a parabolic profile. This correction is applied during both the consolidation and shear phases. The filter, membrane, and Time to 50% consolidation remain unchanged, as shown. The test type is selected based on drained and undrained conditions. Selecting "showing strength" does not impact the test but simply displays failure at the chosen option for graphical representation in the generated test report:



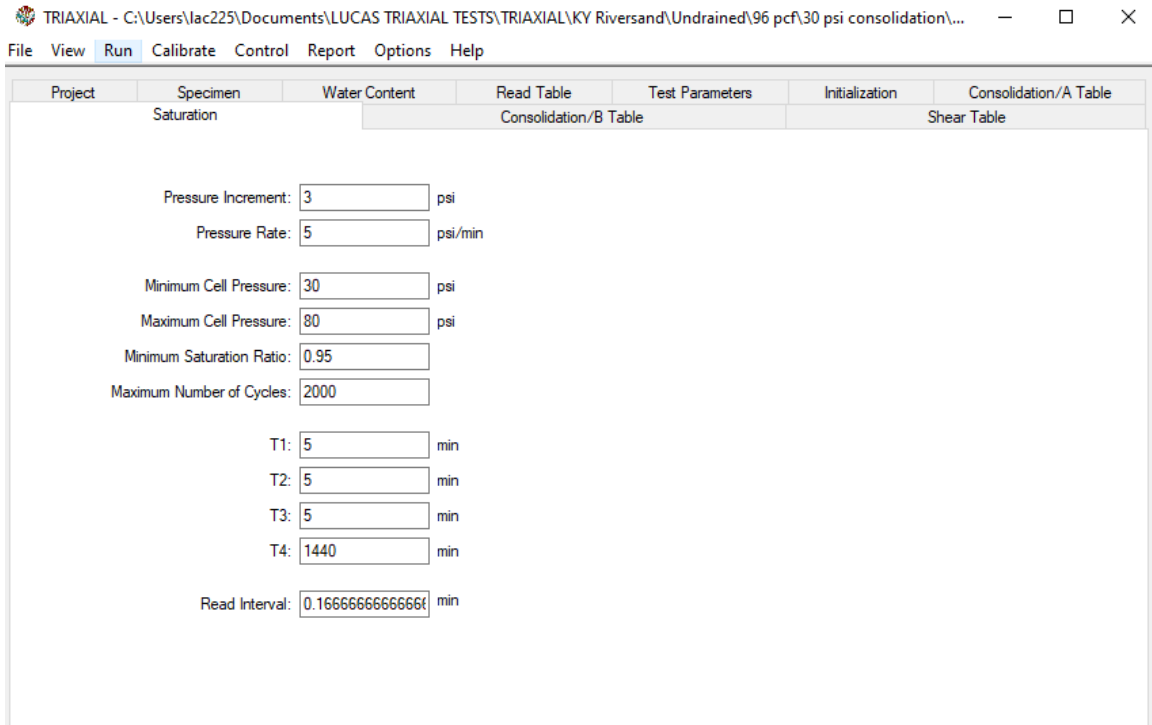
Step 18: In the **Initialization** page, the sample can be left for a period of 4, 8, 16, and 24 hours to facilitate saturation. The set cell pressure and sample pressure ensure an effective stress of 5 psi throughout the test. Depending on the effective stress you plan to test at, adjust the values accordingly to match the difference. Skip the **Consolidation/A** table and proceed to the **Saturation** page. However, if you need to perform a Consolidation/A before saturation, you can follow the same procedure provided in Step 20:

TRIAxIAL - C:\Users\lac225\Documents\LUCAS TRIAXIAL TESTS\TRIAxIAL\KY Riversand\Undrained\96 pcf\30 psi consolidation\... — □ ×

File View Run Calibrate Control Report Options Help

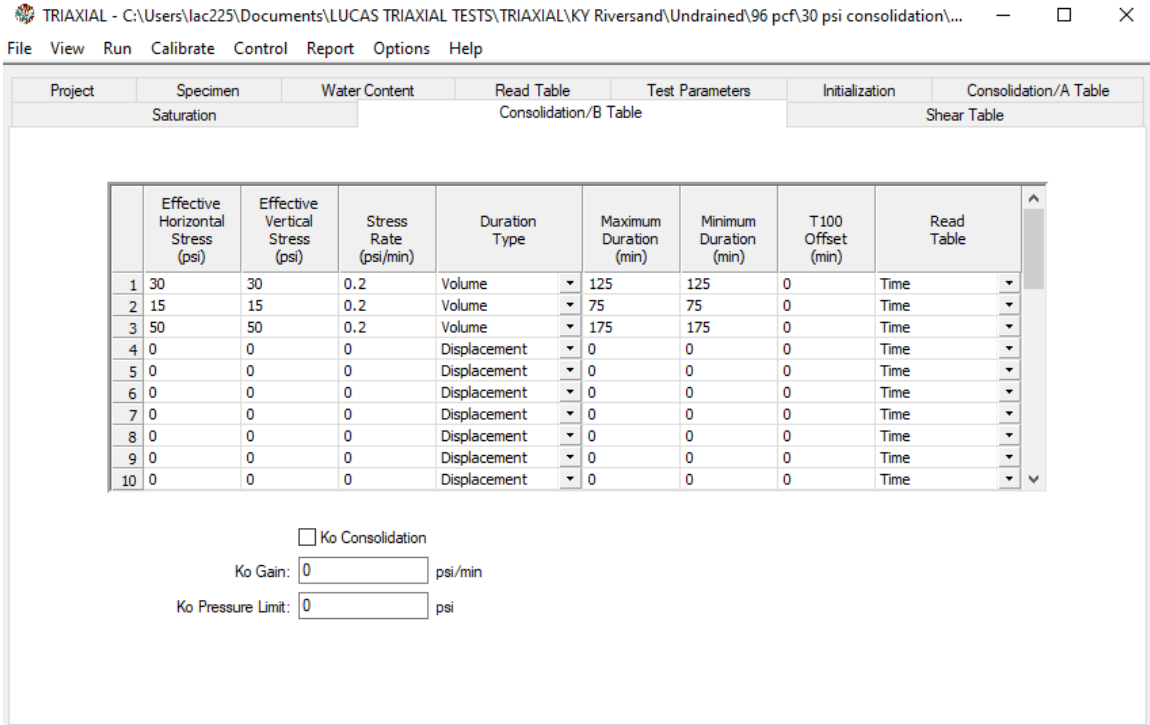
Saturation			Consolidation/B Table		Shear Table	
Project	Specimen	Water Content	Read Table	Test Parameters	Initialization	Consolidation/A Table
<p>Horizontal Stress: <input type="text" value="7"/> psi</p> <p>Vertical Stress: <input type="text" value="7"/> psi</p> <p>Sample Pressure: <input type="text" value="2"/> psi</p> <p>Stress Rate: <input type="text" value="10"/> psi/min</p> <p>Duration: <input type="text" value="1440"/> min</p> <p>Read Table: <input type="text" value="Time"/> ▾</p>						

Step 19: In the **Saturation** page provided below, input the target B value along with the pressure increment and pressure rate. The pressure increment denotes the amount by which the cell pressure and sample pressure are increased as the B value is determined at the specified pressure rate. The pressure will be continuously increased until the B value or the minimum and maximum cell pressure is achieved. T1 represents the duration during which the cell pressure is maintained before the sample pressure is increased, and the B value is measured. T2 represents the duration during which the sample pressure is maintained before the cell pressure is increased. T3 represents the duration at the beginning of each cycle between the decrease of cell and sample pressure and the increase of cell pressure. T4 represents the duration the program waits after the maximum number of cycles is achieved:



Step 20: The **Consolidation/B** table is utilized to govern the consolidation phase, both isotropically and anisotropically. The read table employed for the consolidation phase is time, and the duration type is based on volume.

The example provided below illustrates a loading, unloading, and reloading cycle of 30 psi, 15 psi, and 50 psi, respectively. To conduct a test for only a loading cycle, you would input the target effective stress pressure, which in this case would be 50 psi. The stress rate is calculated based on the effective stress and the duration for the consolidation phase:



Step 21: The **Shear Table** page is utilized to manage the shear phase of the triaxial test. The vertical stress is determined by dividing the load frame capacity by the area of the specimen. The stress type is set to relative to ensure that the vertical stress set is the increment at which the system will apply stress at the beginning of the shear phase.

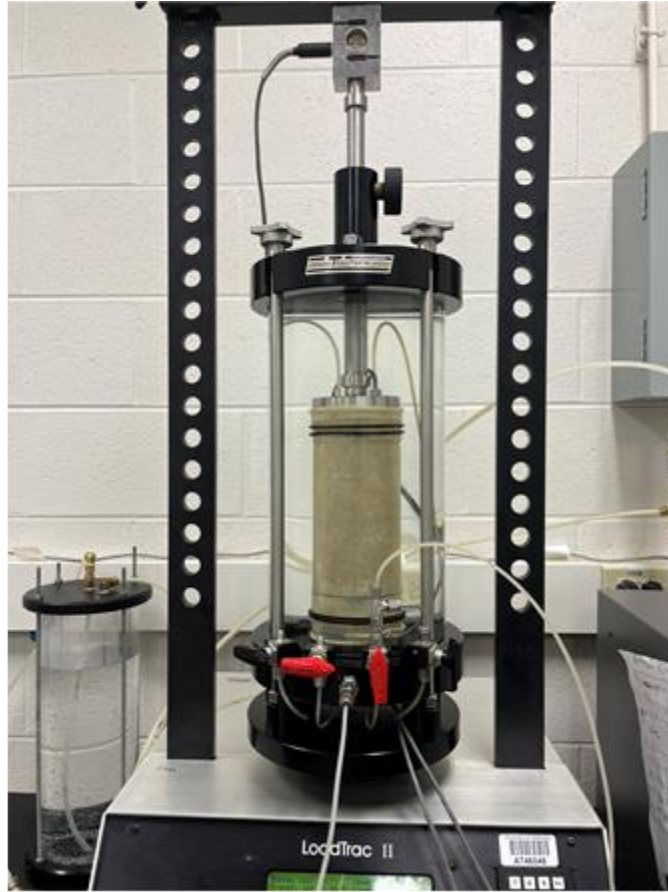
The shear step type is selected based on whether the test is drained or undrained. Shear step control is achieved by strain, and the rate is typically set at 0.05 %/min for a CU test and 0.025 %/min for a CD test. These values can be adjusted depending on the soil type and expected field conditions. The maximum strain represents the strain at which the shear phase concludes, and the test concludes:

TRIAxIAL - C:\Users\lac225\Documents\LUCAS TRIAXIAL TESTS\TRIAxIAL\KY Riversand\Undrained\96 pcf\30 psi consolidation\... — □ ×

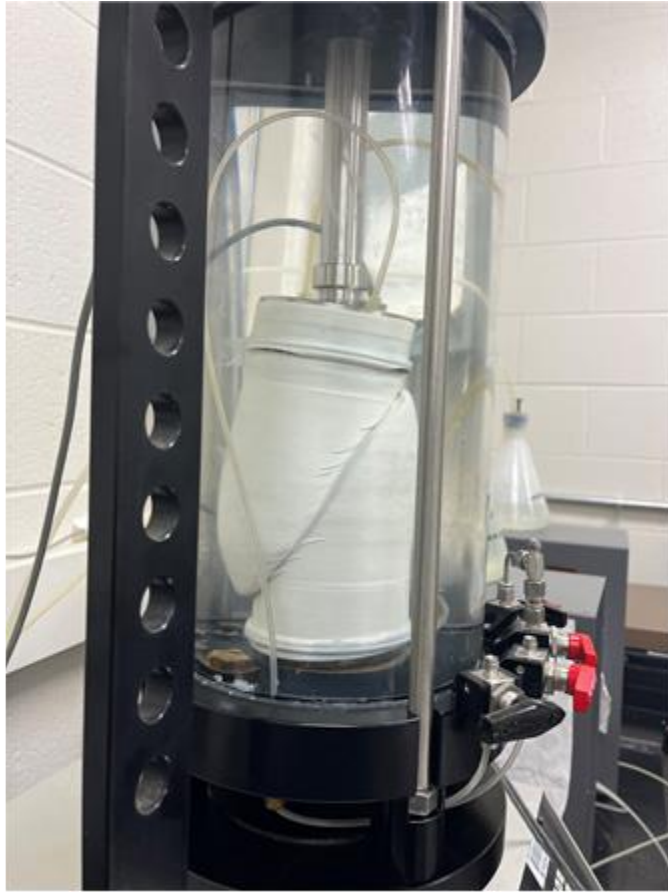
File View Run Calibrate Control Report Options Help

Project	Specimen	Water Content	Read Table	Test Parameters	Initialization	Consolidation/A Table				
Saturation		Consolidation/B Table		Shear Table						
	Horizontal Stress (psi)	Vertical Stress (psi)	Stress Type	Pore Pressure Change (psi)	Shear Step Type	Shear Step Control	Rate (/min)	Maximum Strain (%)	Maintain Time (min)	Read Table
1	0	1000	Relative ▾	0	Undrained ▾	Strain ▾	0.05	25	0	Strain ▾
2	0	0	Absolute ▾	0	Undrained ▾	Strain ▾	0	0	0	Time ▾
3	0	0	Absolute ▾	0	Undrained ▾	Strain ▾	0	0	0	Time ▾
4	0	0	Absolute ▾	0	Undrained ▾	Strain ▾	0	0	0	Time ▾
5	0	0	Absolute ▾	0	Undrained ▾	Strain ▾	0	0	0	Time ▾
6	0	0	Absolute ▾	0	Undrained ▾	Strain ▾	0	0	0	Time ▾
7	0	0	Absolute ▾	0	Undrained ▾	Strain ▾	0	0	0	Time ▾
8	0	0	Absolute ▾	0	Undrained ▾	Strain ▾	0	0	0	Time ▾
9	0	0	Absolute ▾	0	Undrained ▾	Strain ▾	0	0	0	Time ▾
10	0	0	Absolute ▾	0	Undrained ▾	Strain ▾	0	0	0	Time ▾

Step 22: After configuring the test parameters, close the sample and cell pressure controls described in Step 10. When prompted by the software to fill the pumps, decline this option as the pumps should be filled according to the specifications outlined in Step 12. Subsequently, the software proceeds to initialize the platen step and prompts you to unlock the piston. Once the piston makes contact with the load frame, you can commence the test. Open the top and bottom valves on the bridge to begin the testing process:

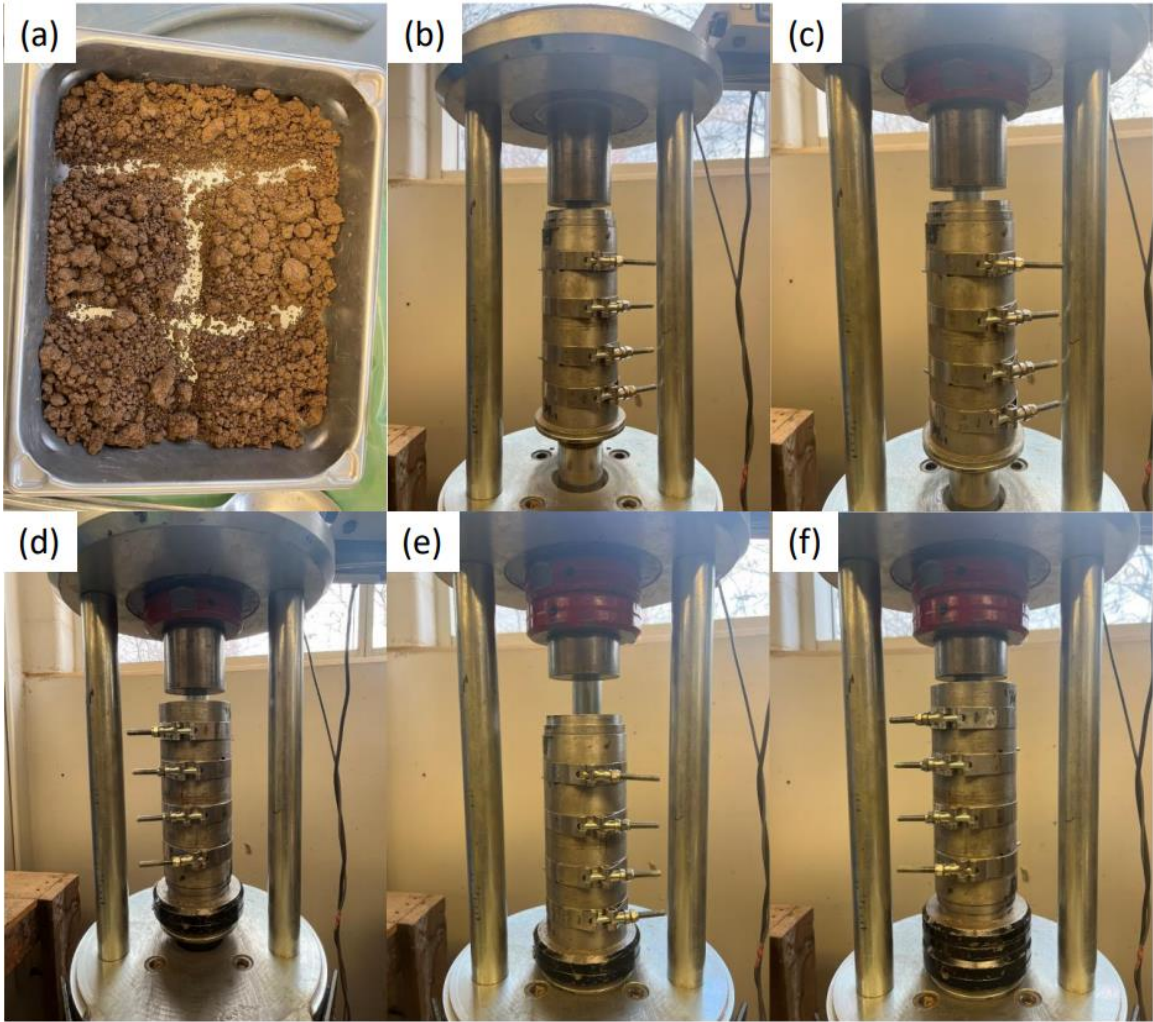


Step 23: After completing the test, close the top and bottom valves on the bridge. Then, navigate to the cell and sample pressure pump controls. Proceed to **Position > Control valves > Supply valve** to release the pressure in the cell, thereby disconnecting the sample:

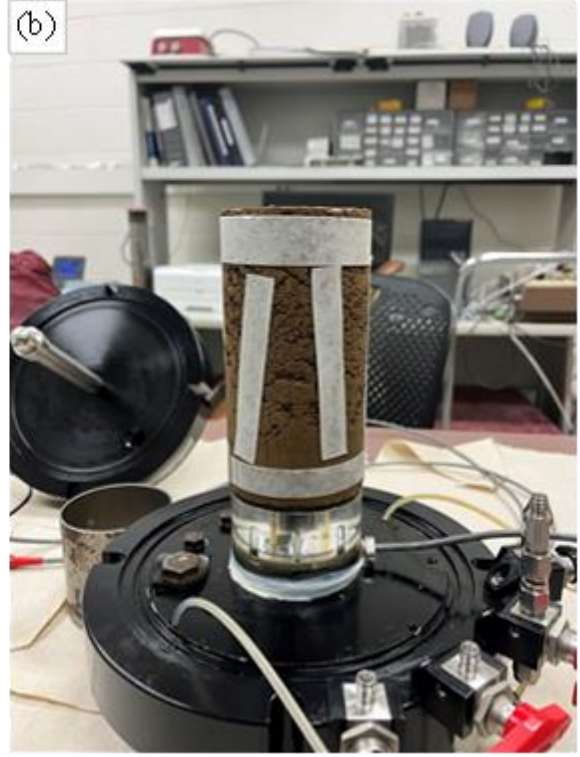


Sample preparation for Clay sample is shown in the subsequent steps:

Step 23: The sample is divided into five equal portions and compacted in lifts, with placers guiding the placement and the mold positioned accordingly. Following each lift, the surface is scarified to ensure uniform compaction and prevent breakage due to gaps between layers:



Step 24: Following compaction, the sample is extruded from the split mold and transferred into a plastic bag to preserve moisture, preparing it for testing. Paper filters are then positioned on the sample to evenly distribute water flow. Subsequently, the procedure outlined from Steps 5 to 23 is followed to conduct the test:



APPENDIX C - TRIAXIAL TEST RESULTS

The critical and peak phi angles for KY River sand and Hamburg clay at drained and undrained shearing conditions are presented in Table C-1. In Figures C-1 and C-2, the deviatoric stress, volumetric strain, and excess pore water pressure against axial strain for KY River sand and Hamburg clay are presented. Figure C-3 presents the variation of shear wave velocity during consolidation at the stages of loading, unloading, and reloading for the KY River sand at 15.39 kN/m³.

Table C-1 Peak and critical friction angles at drained and undrained conditions for the KY River sand and Hamburg clay.

Target γ_{dry} (kN/m ³)	KY River sand				Hamburg clay			
	Peak phi Angle		Critical phi angle		Peak phi angle		Critical phi angle	
	Draine d	Undraine d	Draine d	Undraine d	Draine d	Undraine d	Draine d	Undraine d
15.08	34.10	32.92	32.34	30.11	24.84	22.31	24.84	22.31
15.39	35.60	33.90	32.08	30.12	26.59	20.98	26.59	20.98
15.71	35.37	33.64	32.39	30.10	29.49	21.88	29.49	21.88
16.02	38.54	37.10	36.22	31.95	27.33	22.78	27.33	22.78

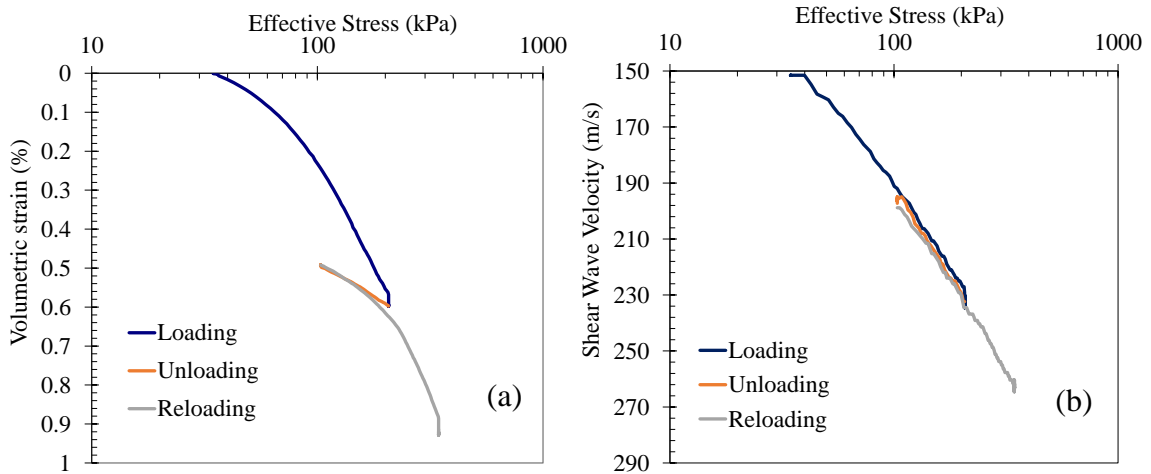


Figure C-1 Three stages of loading, unloading and reloading; (a) Consolidation plot; (b) Shear wave velocities plotted against effective stress for the consolidation phase.

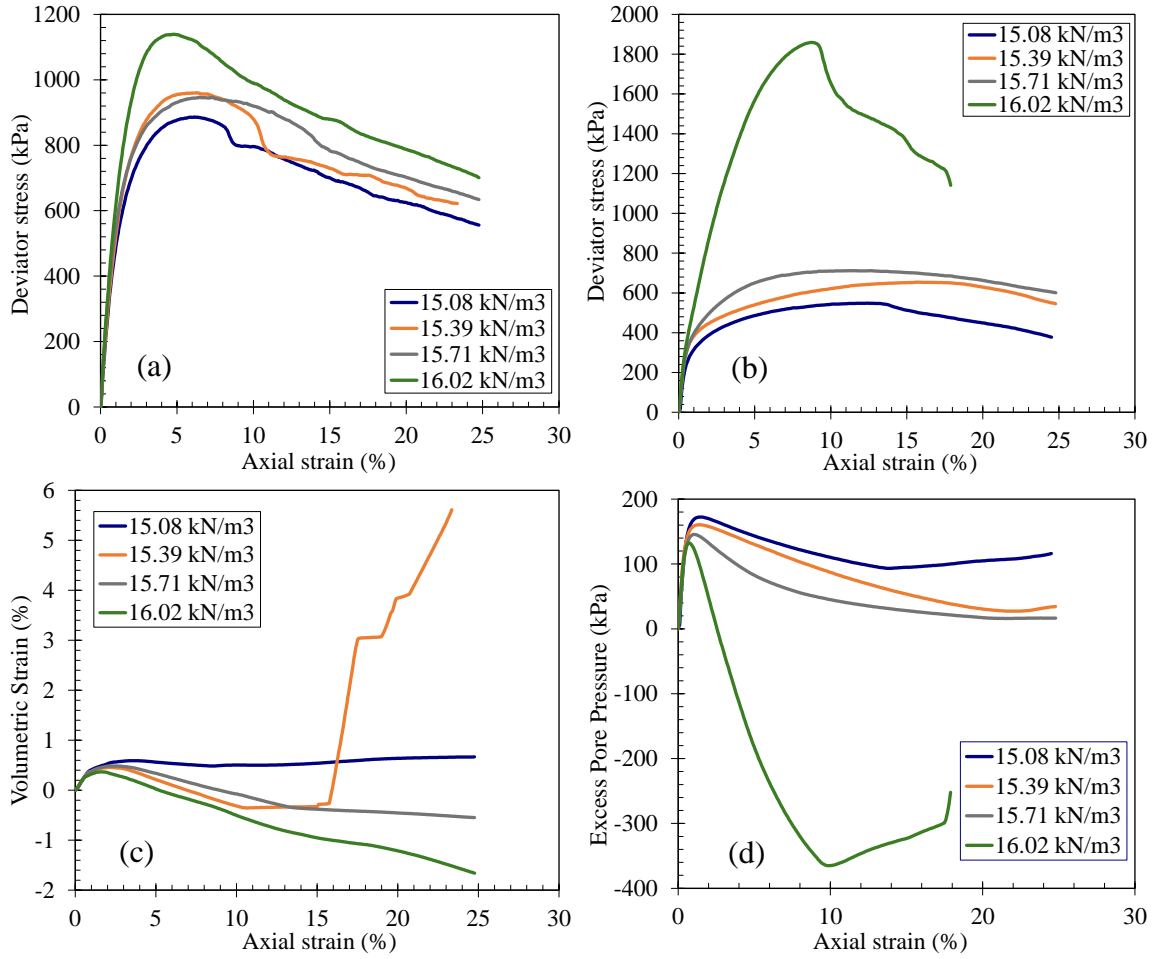


Figure C-2 Variations of the KY River sand under drained and undrained conditions. (a) Drained deviatoric stress against axial strain; (b) undrained deviatoric stress against axial strain; (c) volumetric strain at drained conditions; (d) excess pore water pressures at undrained conditions.

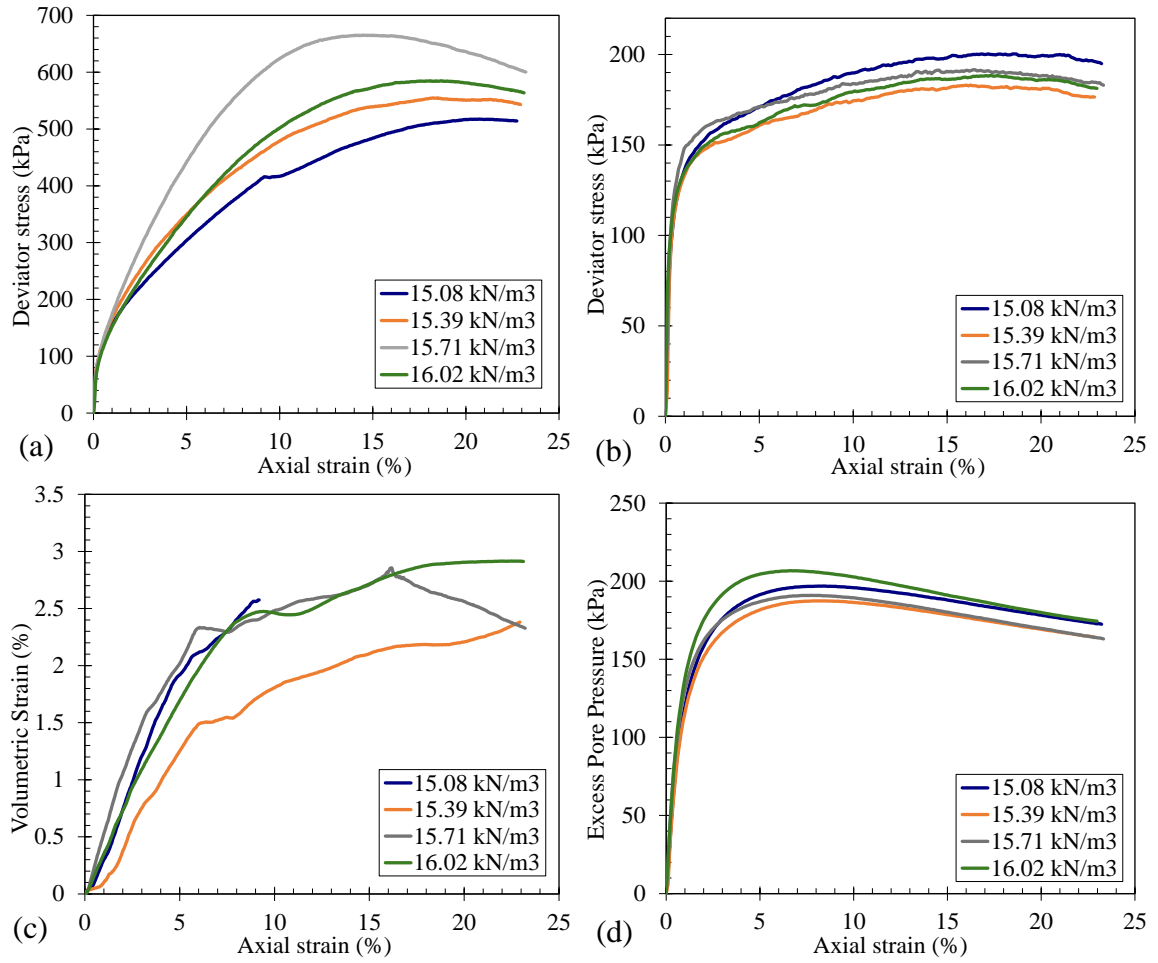


Figure C-3 Variations of the Hamburg clay under drained and undrained conditions. (a) Drained deviatoric stress against axial strain; (b) undrained deviatoric stress against axial strain; (c) volumetric strain at drained conditions; (d) excess pore water pressure.

APPENDIX D - CODE FOR AUTOMATION FOR BENDER ELEMENTS

The Windows PowerShell algorithm that enables the automation of collecting bender elements data while running triaxial tests. The code was modified to allow for four stacks to help reduce signal-to-noise ratio. To identify the mouse coordinates on the computer screen, Mofiki Coordinate Finder was used and can be downloaded at <https://www.softpedia.com/get/Desktop-Enhancements/Other-Desktop-Enhancements/Mofiki-s-Coordinate-Finder.shtml>. The algorithm for the bender automation are as follows:

```
$cSource = '@'
using System;
using System.Drawing;
using System.Runtime.InteropServices;
using System.Windows.Forms;
public class Clicker
{
//https://msdn.microsoft.com/en-us/library/windows/desktop/ms646270(v=vs.85).aspx
[StructLayout(LayoutKind.Sequential)]
struct INPUT
{
    public int    type; // 0 = INPUT_MOUSE,
                  // 1 = INPUT_KEYBOARD
                  // 2 = INPUT_HARDWARE
    public MOUSEINPUT mi;
}

//https://msdn.microsoft.com/en-us/library/windows/desktop/ms646273(v=vs.85).aspx
[StructLayout(LayoutKind.Sequential)]
struct MOUSEINPUT
{
    public int    dx ;
    public int    dy ;
    public int    mouseData ;
    public int    dwFlags;
    public int    time;
    public IntPtr dwExtraInfo;
}

//This covers most use cases although complex mice may have additional buttons
//There are additional constants you can use for those cases, see the msdn page
const int MOUSEEVENTF_MOVED    = 0x0001 ;
const int MOUSEEVENTF_LEFTDOWN  = 0x0002 ;
const int MOUSEEVENTF_LEFTUP    = 0x0004 ;
const int MOUSEEVENTF_RIGHTDOWN = 0x0008 ;
const int MOUSEEVENTF_RIGHTUP   = 0x0010 ;
const int MOUSEEVENTF_MIDDLEDOWN = 0x0020 ;
const int MOUSEEVENTF_MIDDLEUP   = 0x0040 ;
const int MOUSEEVENTF_WHEEL     = 0x0080 ;
const int MOUSEEVENTF_XDOWN     = 0x0100 ;
const int MOUSEEVENTF_XUP       = 0x0200 ;
const int MOUSEEVENTF_ABSOLUTE  = 0x8000 ;

const int screen_length = 0x10000 ;
```

```

//https://msdn.microsoft.com/en-us/library/windows/desktop/ms646310(v=vs.85).aspx
[System.Runtime.InteropServices.DllImport("user32.dll")]
extern static uint SendInput(uint nInputs, INPUT[] pInputs, int cbSize);

public static void LeftClickAtPoint(int x, int y)
{
    //Move the mouse
    INPUT[] input = new INPUT[3];
    input[0].mi.dx = x*(65535/System.Windows.Forms.Screen.PrimaryScreen.Bounds.Width);
    input[0].mi.dy = y*(65535/System.Windows.Forms.Screen.PrimaryScreen.Bounds.Height);
    input[0].mi.dwFlags = MOUSEEVENTF_MOVED | MOUSEEVENTF_ABSOLUTE;
    //Left mouse button down
    input[1].mi.dwFlags = MOUSEEVENTF_LEFTDOWN;
    //Left mouse button up
    input[2].mi.dwFlags = MOUSEEVENTF_LEFTUP;
    SendInput(3, input, Marshal.SizeOf(input[0]));
}
}
'@
Add-Type -TypeDefinition $cSource -ReferencedAssemblies System.Windows.Forms,System.Drawing
# -----

# get GDSBES process
$GDS = Get-Process GDSBES -ErrorAction SilentlyContinue
if ($GDS) {
    # try gracefully first
    $GDS.CloseMainWindow()
    # kill after five seconds
    Sleep 5
    if (!$GDS.HasExited) {
        $GDS | Stop-Process -Force
    }
}
Remove-Variable GDS

function Show-Process($Process, [Switch]$Maximize)
{
    $sig = '
    [DllImport("user32.dll")] public static extern bool ShowWindowAsync(IntPtr hWnd, int nCmdShow);
    [DllImport("user32.dll")] public static extern int SetForegroundWindow(IntPtr hWnd);
    '

    if ($Maximize) { $Mode = 3 } else { $Mode = 4 }
    $type = Add-Type -MemberDefinition $sig -Name WindowAPI -PassThru
    $hwnd = $process.MainWindowHandle
    $null = $type::ShowWindowAsync($hwnd, $Mode)
    $null = $type::SetForegroundWindow($hwnd)
}

[Clicker]::LeftClickAtPoint(512,1029)

Start-Sleep -s 5

[System.Windows.Forms.SendKeys]::SendWait("%(o)")

```

```

Start-Sleep -s 2

[Clicker]::LeftClickAtPoint(699,458)
[Clicker]::LeftClickAtPoint(699,458)

Start-Sleep -s 2

[System.Windows.Forms.SendKeys]::SendWait("144")

Start-Sleep -s 2

[System.Windows.Forms.SendKeys]::SendWait("%(n)")

Start-Sleep -s 2

[Clicker]::LeftClickAtPoint(858,386)
[Clicker]::LeftClickAtPoint(858,386)

Start-Sleep -s 1

[System.Windows.Forms.SendKeys]::SendWait("0.1")

Start-Sleep -s 1

[System.Windows.Forms.SendKeys]::SendWait("%(n)")

Start-Sleep -s 1

# Always Stack Command

[Clicker]::LeftClickAtPoint(722,461)

Start-Sleep -s 1

[System.Windows.Forms.SendKeys]::SendWait("%(n)")

Start-Sleep -s 1

[System.Windows.Forms.SendKeys]::SendWait("%(s)")

Start-Sleep -s 1

$Number_shots=20; # total number of be shots

$hour= Get-Date -Format HH # distinctive hour for the shots (hour of the FIRST shot taken)
$minute= Get-Date -Format mm # distinctive minute for the shots (hour of the FIRST shot taken)

# counter to repeat the following commands

for ($idx = 1 ; $idx -le $Number_shots ; $idx++ )
{

$delay = 80 # time delay between BE shots in SECONDS

# Triggering the bender element for the S-wave with four stacks

```

```
[Clicker]::LeftClickAtPoint(773,487)

Start-Sleep -s 1

[Clicker]::LeftClickAtPoint(773,487)

Start-Sleep -s 1

[Clicker]::LeftClickAtPoint(773,487)

Start-Sleep -s 1

[Clicker]::LeftClickAtPoint(773,487)

Start-Sleep -s 1

[Clicker]::LeftClickAtPoint(773,487)

Start-Sleep -s 2

# Save the S-wave shot

[Clicker]::LeftClickAtPoint(775,556)

Start-Sleep -s 1

[System.Windows.Forms.SendKeys]::SendWait("HamburgClay_S_$idx $hour $minute")

Start-Sleep -s 1

[System.Windows.Forms.SendKeys]::SendWait("{ENTER}")

Start-Sleep -s 1

[Clicker]::LeftClickAtPoint(1136,521)
[Clicker]::LeftClickAtPoint(1136,521)

Start-Sleep -s 1

[System.Windows.Forms.SendKeys]::SendWait("0")

# CHANGING TRIGGER TO P-WAVE
#

[Clicker]::LeftClickAtPoint(620,453)

Start-Sleep -s 1

[Clicker]::LeftClickAtPoint(616,404)

Start-Sleep -s 1

# click Ok

[Clicker]::LeftClickAtPoint(658,548)
```

```
Start-Sleep -s 1

# Triggering the bender element for the P-wave with four stacks

[Clicker]::LeftClickAtPoint(773,487)

Start-Sleep -s 1

[Clicker]::LeftClickAtPoint(773,487)

Start-Sleep -s 1

[Clicker]::LeftClickAtPoint(773,487)

Start-Sleep -s 1

[Clicker]::LeftClickAtPoint(773,487)

Start-Sleep -s 1

[Clicker]::LeftClickAtPoint(773,487)

Start-Sleep -s 2

# Save the P-wave shot

[Clicker]::LeftClickAtPoint(775,556)

Start-Sleep -s 1

[System.Windows.Forms.SendKeys]::SendWait("HamburgClay_P_$idx $hour $minute")

Start-Sleep -s 1

[System.Windows.Forms.SendKeys]::SendWait("{ENTER}")

Start-Sleep -s 1

[Clicker]::LeftClickAtPoint(1136,521)
[Clicker]::LeftClickAtPoint(1136,521)

Start-Sleep -s 1

[System.Windows.Forms.SendKeys]::SendWait("0")

# RETURNING TRIGGER TO S-WAVE
#

[Clicker]::LeftClickAtPoint(620,453)

Start-Sleep -s 1

[Clicker]::LeftClickAtPoint(497,404)

Start-Sleep -s 1
```

```

# click Ok

[Clicker]::LeftClickAtPoint(658,548)

# time delay for the next pair of shots

#Start-Sleep -s $delay

# Counter for the next pair of shots

$Counter_Form = New-Object System.Windows.Forms.Form
$Counter_Form.Text = "Countdown Timer for BE shots!"
$Counter_Form.Width = 450
$Counter_Form.Height = 200
$Counter_Label = New-Object System.Windows.Forms.Label
$Counter_Label.AutoSize = $true
$Counter_Label.ForeColor = "Green"
$normalfont = New-Object System.Drawing.Font("Times New Roman",18)
$Counter_Label.Font = $normalfont
$Counter_Label.Left = 20
$Counter_Label.Top = 20
$Counter_Form.Controls.Add($Counter_Label)
while ($delay -ge 0)
{
    $Counter_Form.Show()
    $Counter_Label.Text = "Seconds Remaining: $($delay)"
    if ($delay -lt 5)
    {
        $Counter_Label.ForeColor = "Red"
        $fontsize = 20-$delay
        $warningfont = New-Object System.Drawing.Font("Times New
Roman",$fontsize,[System.Drawing.FontStyle]([System.Drawing.FontStyle]::Bold -bor
[System.Drawing.FontStyle]::Underline))
        $Counter_Label.Font = $warningfont
    }
    start-sleep 1
    $delay -= 1
}
$Counter_Form.Close()

Show-Process -Process (Get-Process -Name GDSBES) -Maximize

}

```


APPENDIX E – MATLAB CODE FOR PICKING ARRIVAL TIMES OF WAVES

The Matlab code for picking the compressional and shear wave arrival times are provided. Matlab R2022b was used for the code.

```
clearvars
BE_files = dir('*.*bes');
%%
T = struct2table(BE_files);% convert the struct array to a table
sortedT = sortrows(T, 'date');% % sort the table by 'date'
sorted_BE_files = table2struct(sortedT);% change it back to struct array if necessary
sorted_BE_files_cell=struct2cell(sorted_BE_files);
%%

sz=[numel(BE_files) 3]
varTypes = {'string','double','double'};
varNames = {'File Name','Travel time','Period'};
Table_Data = table('Size',sz,'VariableTypes',varTypes,'VariableNames',varNames);

MaxPlot=50;%max number of traces in the figure
Plot_count=0;
MaxV=14;
figure_number=0;
figure
tpeak_I=zeros(numel(BE_files),1);
Trav_time=zeros(numel(BE_files),1);
for j=1:numel(BE_files)

    Plot_count =Plot_count+1;% counter for the number of traces in the figure

    % filename = BE_files(j).name;
    filename = sorted_BE_files(j).name;
    str=convertCharsToStrings(sorted_BE_files(j).name);
    chr=sorted_BE_files(j).name;
%    Legend_plot= (chr(strfind(str,'Wave')+5:strfind(str,'bes')-2));
    Legend_plot= (chr(strfind(str,'BE_')+12:strfind(str,'bes')-2));

    fileID = fopen(filename);
    for i = 1:4
        fgets(fileID);
    end
    AuxP=fgetl(fileID);
    Text_size=size(AuxP);
    Period_text=AuxP(27:Text_size(2)-1);
    Period=str2double(Period_text)/1000;% period in seconds
    for i = 1:10
        fgets(fileID);
    end
    tpeak_I(j)=Period/4;%time to the peak of the input wave
    %Data = textscan(fileID,'%s %s %s %s','Delimiter',' ');
    Data = textscan(fileID,'%q %q %q %q','Delimiter',' ');
    Time=str2double(Data{1});
    Input_wave=str2double(Data{2});
    Output_wave=str2double(Data{3});
```

```

if Plot_count <= MaxPlot
    hold on
    % plot(Time*1000,Output_wave+(Plot_count-1)*MaxV,'DisplayName',Legend_plot)
    plot(Time*1000,Output_wave-(Plot_count-1)*MaxV,'DisplayName',Legend_plot)
    legend
    set(legend,'fontsize',6);
    if Plot_count==MaxPlot || j==numel(BE_files)
        Peak_points=ginput(Plot_count);
        tpeak_0=Peak_points(:,1);
        Trav_time(j- length(Peak_points(:,1))+1:j)=tpeak_0-tpeak_I(j- length(Peak_points(:,1))+1:j);
    %     Table_Data(j-MaxPlot+1:j,:)= { sorted_BE_files(j-MaxPlot+1:j).name,Trav_time(j-
    MaxPlot+1:j,:),tpeak_I(j-MaxPlot+1:j)*4};
    %     Table_Data(j-MaxPlot+1:j,:)= { string(sorted_BE_files_cell((j-MaxPlot+1:j),1)),Trav_time(j-
    MaxPlot+1:j,:),tpeak_I(j-MaxPlot+1:j)*4};
        Table_Data(j- length(Peak_points(:,1))+1:j,:)=table(string(sorted_BE_files_cell((j-
    length(Peak_points(:,1))+1:j),1)),Trav_time(j- length(Peak_points(:,1))+1:j,:),tpeak_I(j-
    length(Peak_points(:,1))+1:j)*4);
        end
    else
        figure_number=figure_number+1;
        saveas(gcf,strcat('Figure',num2str(figure_number),'.png'))
        saveas(gcf,strcat('Figure',num2str(figure_number)))
        figure
        Plot_count=1;
        % plot(Time*1000,Output_wave+(Plot_count-1)*MaxV,'DisplayName',Legend_plot)
        plot(Time*1000,Output_wave-(Plot_count-1)*MaxV,'DisplayName',Legend_plot)
        set(legend,'fontsize',6);
    end
    xlim([0 4])
    xlabel('Time [ms]')
    set(gca,'YTickLabel',[]);
    % set(gca,'YTick',-MaxV:MaxV:(Plot_count-1)*MaxV);
    set(gca,'YTick',-(Plot_count-1)*MaxV:MaxV:MaxV);
    box on
    fclose(fileID);
end

%to save the last figure
if j==numel(BE_files)
    saveas(gcf,strcat('Figure',num2str(figure_number+1),'.png'))
    saveas(gcf,strcat('Figure',num2str(figure_number+1)))
end
writetable(Table_Data);

% (struct2cell(sorted_BE_files(j-MaxPlot+1:j)));ans(1,:)

```

APPENDIX F – ROSETTA

The interface for Rosetta in HYDRUS 1-D is shown in Figure F-1. The required input data for both KY River sand and Hamburg clay are shown with the predicted van Genuchten (1980) parameters, α and n as well the volumetric water contents θ_s and θ_r . The parameter m is then determined using Mualem (1976) approximation.

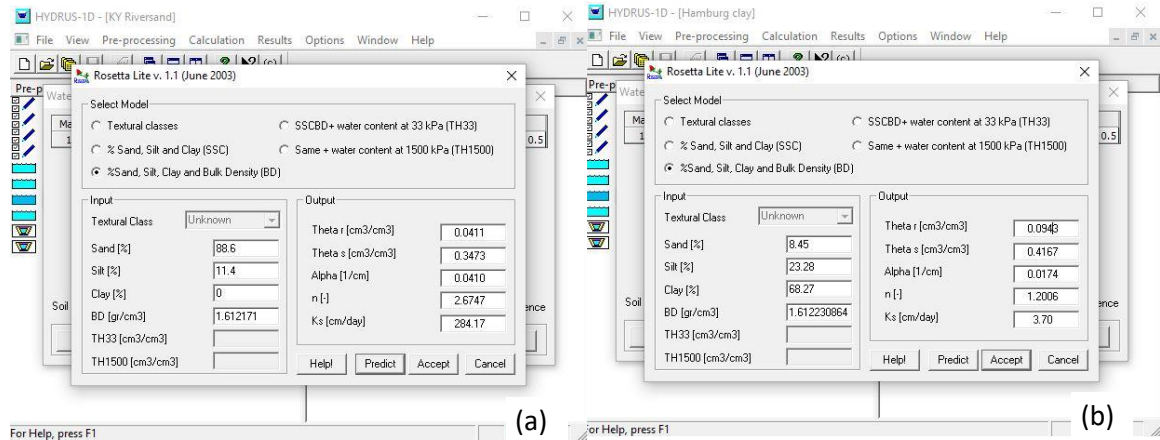


Figure F-1 Rosetta interface with input data and predicted parameters. (a) KY River sand; (b) Hamburg clay.

REFERENCES

- Adama, D., Bryson, L. S., and Wang, A. (2023). Airfield suitability assessment from geophysical methods. *Transportation Geotechnics*, 42, 101059.
- Ahmad-Adli, M., Huvaj, N., and Kartal Toker, N. (2014). Effects of the Size of Particles on Rainfall-Induced Slope Instability in Granular Soils. In *Geo-Congress 2014 Technical Papers* (pp. 4027-4036).
<https://doi.org/doi:10.1061/9780784413272.391>
- Ahmed, F. S., Bryson, L. S., and Crawford, M. M. (2021). Prediction of seasonal variation of in-situ hydrologic behavior using an analytical transient infiltration model. *Engineering Geology*, 294, 106383.
<https://doi.org/https://doi.org/10.1016/j.enggeo.2021.106383>
- Archie, G. E. (1942). The electric resistivity log as an aid in determining some reservoir characteristics: AIME Transactions, v. 46.
- Atkinson, J. H., and Sallfors, G. (1991). Experimental determination of stress-strain-time characteristics in laboratory and in-situ tests. . Proc. 10th Eur. Conf. Soil Mech. and Found Engng,
- Barus, R. M. N., Jotisankasa, A., Chaiprakaikeow, S., and Sawangsuriya, A. (2019). Laboratory and field evaluation of modulus-suction-moisture relationship for a silty sand subgrade. *Transportation Geotechnics*, 19, 126-134.
- Bayat, H., Mazaheri, B., and Mohanty, B. P. (2019). Estimating soil water characteristic curve using landscape features and soil thermal properties. *Soil and Tillage Research*, 189, 1-14. <https://doi.org/https://doi.org/10.1016/j.still.2018.12.018>
- Calamita, G., Brocca, L., Perrone, A., Piscitelli, S., Lapenna, V., Melone, F., and Moramarco, T. (2012). Electrical resistivity and TDR methods for soil moisture estimation in central Italy test-sites. *Journal of hydrology*, 454-455, 101-112.
<https://doi.org/https://doi.org/10.1016/j.jhydrol.2012.06.001>
- Carlton, B. D., and Pestana, J. M. (2016). A unified model for estimating the in-situ small strain shear modulus of clays, silts, sands, and gravels. *Soil Dynamics and Earthquake Engineering*, 88, 345-355.
<https://doi.org/https://doi.org/10.1016/j.soildyn.2016.01.019>
- Crawford, M. M., Bryson, L. S., Woolery, E. W., and Wang, Z. (2019). Long-term landslide monitoring using soil-water relationships and electrical data to estimate suction stress. *Engineering Geology*, 251, 146-157.
<https://doi.org/https://doi.org/10.1016/j.enggeo.2019.02.015>
- Cunningham, M. R., Ridley, A. M., Dineen, K., and Burland, J. B. (2003). The mechanical behaviour of a reconstituted unsaturated silty clay. *Géotechnique*, 53(2), 183-194. <https://doi.org/10.1680/geot.2003.53.2.183>
- Dadashiserej, A., Jana, A., Xu, Z., Stuedlein, A. W., Evans, T. M., II, K. H. S., and Cox, B. R. (2023). Dynamic Response of a Low Plasticity Silt Deposit: Comparison of In-situ and Laboratory Responses. *Canadian Geotechnical Journal*.
<https://doi.org/10.1139/cgj-2022-0579>
- de Melo, L. B. B., Silva, B. M., Peixoto, D. S., Chiarini, T. P. A., de Oliveira, G. C., and Curi, N. (2021). Effect of compaction on the relationship between electrical resistivity and soil water content in Oxisol. *Soil and Tillage Research*, 208, 104876. <https://doi.org/https://doi.org/10.1016/j.still.2020.104876>

- Dong, Y., Lu, N., and McCartney, J. S. (2016). Unified Model for Small-Strain Shear Modulus of Variably Saturated Soil. *Journal of Geotechnical and Geoenvironmental Engineering*, 142(9), 04016039. [https://doi.org/doi:10.1061/\(ASCE\)GT.1943-5606.0001506](https://doi.org/doi:10.1061/(ASCE)GT.1943-5606.0001506)
- Dong, Y., Lu, N., and McCartney, J. S. (2018). Scaling Shear Modulus from Small to Finite Strain for Unsaturated Soils. *Journal of Geotechnical and Geoenvironmental Engineering*, 144(2), 04017110. [https://doi.org/doi:10.1061/\(ASCE\)GT.1943-5606.0001819](https://doi.org/doi:10.1061/(ASCE)GT.1943-5606.0001819)
- Escario, V., and Juca, J. F. T. (1989). Strength and deformation of partly saturated soils. In Proc. 12th Int. Conf. on SMFE, Rio de Janeiro, Brazil.
- Escario, V., and Sáez, J. (1986). The shear strength of partly saturated soils. *Géotechnique*, 36(3), 453-456. <https://doi.org/10.1680/geot.1986.36.3.453>
- Fredlund, D. G. (2019). State of practice for use of the soil-water characteristic curve (SWCC) in geotechnical engineering. *Canadian Geotechnical Journal*, 56(8), 1059-1069. <https://doi.org/10.1139/cgj-2018-0434>
- Fredlund, D. G., Sheng, D., and Zhao, J. (2011). Estimation of soil suction from the soil-water characteristic curve. *Canadian Geotechnical Journal*, 48(2), 186-198. <https://doi.org/10.1139/t10-060>
- Gao, Y., Sun, D. a., Zhou, A., and Li, J. (2020). Predicting Shear Strength of Unsaturated Soils over Wide Suction Range. *International Journal of Geomechanics*, 20(2), 04019175. [https://doi.org/doi:10.1061/\(ASCE\)GM.1943-5622.0001555](https://doi.org/doi:10.1061/(ASCE)GM.1943-5622.0001555)
- Ghayoomi, M., and McCartney, J. S. (2011). Measurement of Small-Strain Shear Moduli of Partially Saturated Sand During Infiltration in a Geotechnical Centrifuge. *Geotechnical Testing Journal*, 34(5), 503-513. <https://doi.org/10.1520/GTJ103608>
- Guan, G. S., Rahardjo, H., and Choon, L. E. (2010). Shear Strength Equations for Unsaturated Soil under Drying and Wetting. *Journal of Geotechnical and Geoenvironmental Engineering*, 136(4), 594-606. [https://doi.org/doi:10.1061/\(ASCE\)GT.1943-5606.0000261](https://doi.org/doi:10.1061/(ASCE)GT.1943-5606.0000261)
- Hamid, T. B., and Miller, G. A. (2009). Shear strength of unsaturated soil interfaces. *Canadian Geotechnical Journal*, 46(5), 595-606. <https://doi.org/10.1139/t09-002>
- Han, K., Rahardjo, H., and Broms, B. (1995). Effect of hysteresis on the shear strength of a residual soil. Proceedings of the First International Conference on Unsaturated Soils (UNSAT'95), Paris, France.
- Han, Z., and Vanapalli, S. K. (2016). Stiffness and shear strength of unsaturated soils in relation to soil-water characteristic curve. *Géotechnique*, 66(8), 627-647. <https://doi.org/10.1680/jgeot.15.P.104>
- Hardin, B. O., and Black, W. L. (1969). Closure to “Vibration Modulus of Normally Consolidated Clay”. *Journal of the Soil Mechanics and Foundations Division*, 95(6), 1531-1537. <https://doi.org/doi:10.1061/JSFEAQ.0001364>
- Hardin, B. O., and Richart Jr, F. (1963). Elastic wave velocities in granular soils. *Journal of the Soil Mechanics and Foundations Division*, 89(1), 33-65.
- Hippley, B. T. (2003). *Elastic stiffness of unsaturated soil* [Doctoral Dissertation, University of Kentucky].
- Hoyos, L. R., Suescún-Florez, E. A., and Puppala, A. J. (2015). Stiffness of intermediate unsaturated soil from simultaneous suction-controlled resonant column and

- bender element testing. *Engineering Geology*, 188, 10-28.
<https://doi.org/https://doi.org/10.1016/j.enggeo.2015.01.014>
- Ikechukwu, A. F., Hassan, M. M., and Moubarak, A. (2021). Swelling stress effects on shear strength resistance of subgrades. *International Journal of Geotechnical Engineering*, 15(8), 939-949. <https://doi.org/10.1080/19386362.2019.1656445>
- Jafarian, Y., Javdanian, H., and Haddad, A. (2018). Dynamic properties of calcareous and siliceous sands under isotropic and anisotropic stress conditions. *Soils and Foundations*, 58(1), 172-184.
<https://doi.org/https://doi.org/10.1016/j.sandf.2017.11.010>
- Khalili, N., Geiser, F., and Blight, G. E. (2004). Effective Stress in Unsaturated Soils: Review with New Evidence. *International Journal of Geomechanics*, 4(2), 115-126. [https://doi.org/doi:10.1061/\(ASCE\)1532-3641\(2004\)4:2\(115\)](https://doi.org/doi:10.1061/(ASCE)1532-3641(2004)4:2(115))
- Khosravi, A., Ghayoomi, M., McCartney, J., and Ko, H.-Y. (2010). Impact of effective stress on the dynamic shear modulus of unsaturated sand. In *GeoFlorida 2010: Advances in Analysis, Modeling and Design* (pp. 410-419).
- Khosravi, A., and McCartney, J. S. (2012). Impact of Hydraulic Hysteresis on the Small-Strain Shear Modulus of Low Plasticity Soils. *Journal of Geotechnical and Geoenvironmental Engineering*, 138(11), 1326-1333.
[https://doi.org/doi:10.1061/\(ASCE\)GT.1943-5606.0000713](https://doi.org/doi:10.1061/(ASCE)GT.1943-5606.0000713)
- Khosravi, A., Rahimi, M., Gheibi, A., and Shahrabi, M. M. (2018). Impact of Plastic Compression on the Small Strain Shear Modulus of Unsaturated Silts. *International Journal of Geomechanics*, 18(2), 04017138.
[https://doi.org/doi:10.1061/\(ASCE\)GM.1943-5622.0001031](https://doi.org/doi:10.1061/(ASCE)GM.1943-5622.0001031)
- Khosravi, A., Shahbazan, P., and Pak, A. (2018). Impact of hydraulic hysteresis on the small strain shear modulus of unsaturated sand. *Soils and Foundations*, 58(2), 344-354. <https://doi.org/https://doi.org/10.1016/j.sandf.2018.02.018>
- Kidd, J. B. (2011). *Constitutive mechanical relationships for compacted unsaturated soils* [Master's Thesis, University of Kentucky].
- Kristo, C., Rahardjo, H., and Satyanaga, A. (2019). Effect of hysteresis on the stability of residual soil slope. *International Soil and Water Conservation Research*, 7(3), 226-238. <https://doi.org/https://doi.org/10.1016/j.iswcr.2019.05.003>
- Lee, I.-M., Sung, S.-G., and Cho, G.-C. (2005). Effect of stress state on the unsaturated shear strength of a weathered granite. *Canadian Geotechnical Journal*, 42(2), 624-631. <https://doi.org/10.1139/t04-091>
- Lee, S., Seo, W., and Kim, D. (2007). Evaluation of modulus of unsaturated compacted soils in various matric suctions using modified volumetric pressure plate extractor. Proceedings of the 60th Canadian geotechnical conference, Ottawa, Canada,
- Li, A. G., Tham, L. G., Yue, Z. Q., Lee, C. F., and Law, K. T. (2005). Comparison of Field and Laboratory Soil–Water Characteristic Curves. *Journal of Geotechnical and Geoenvironmental Engineering*, 131(9), 1176-1180.
[https://doi.org/doi:10.1061/\(ASCE\)1090-0241\(2005\)131:9\(1176\)](https://doi.org/doi:10.1061/(ASCE)1090-0241(2005)131:9(1176))
- Li, D., Gao, G., Shao, M. a., and Fu, B. (2016). Predicting available water of soil from particle-size distribution and bulk density in an oasis–desert transect in northwestern China. *Journal of hydrology*, 538, 539-550.
<https://doi.org/https://doi.org/10.1016/j.jhydrol.2016.04.046>

- Lings, M., and Greening, P. (2001). A novel bender/extender element for soil testing. *Géotechnique*, 51(8), 713-717.
- Liu, J., Otsubo, M., Kawaguchi, Y., and Kuwano, R. (2022). Anisotropy in small-strain shear modulus of granular materials: Effects of particle properties and experimental conditions. *Soils and Foundations*, 62(1), 101105. <https://doi.org/https://doi.org/10.1016/j.sandf.2021.101105>
- Liu, X., Zou, D., Liu, J., and Zheng, B. (2021). Predicting the small strain shear modulus of coarse-grained soils. *Soil Dynamics and Earthquake Engineering*, 141, 106468. <https://doi.org/https://doi.org/10.1016/j.soildyn.2020.106468>
- Lu, N., and Kaya, M. (2014). Power Law for Elastic Moduli of Unsaturated Soil. *Journal of Geotechnical and Geoenvironmental Engineering*, 140(1), 46-56. [https://doi.org/doi:10.1061/\(ASCE\)GT.1943-5606.0000990](https://doi.org/doi:10.1061/(ASCE)GT.1943-5606.0000990)
- Lu, N., and Likos, W. J. (2006). Suction Stress Characteristic Curve for Unsaturated Soil. *Journal of Geotechnical and Geoenvironmental Engineering*, 132(2), 131-142. [https://doi.org/doi:10.1061/\(ASCE\)1090-0241\(2006\)132:2\(131\)](https://doi.org/doi:10.1061/(ASCE)1090-0241(2006)132:2(131))
- Mahmoodabadi, M., and Bryson, L. S. (2021a). Direct Application of the Soil–Water Characteristic Curve to Estimate the Shear Modulus of Unsaturated Soils. *International Journal of Geomechanics*, 21(1), 04020243. [https://doi.org/doi:10.1061/\(ASCE\)GM.1943-5622.0001893](https://doi.org/doi:10.1061/(ASCE)GM.1943-5622.0001893)
- Mahmoodabadi, M., and Bryson, L. S. (2021b). Prediction of coupled hydromechanical behavior of unsaturated soils based on seasonal variations in hydrologic conditions. *Canadian Geotechnical Journal*, 58(6), 902-913. <https://doi.org/10.1139/cgj-2020-0388>
- Mancuso, C., Vassallo, R., and d'Onofrio, A. (2002). Small strain behavior of a silty sand in controlled-suction resonant column torsional shear tests. *Canadian Geotechnical Journal*, 39(1), 22-31. <https://doi.org/10.1139/t01-076>
- Mayne, P. W. (2001). Stress-strain-strength-flow parameters from enhanced in-situ tests. Proc. Int. Conf. on In Situ Measurement of Soil Properties and Case Histories, Bali,
- Mendoza, C., Colmenares, J., and Merchan, V. (2005). Stiffness of an unsaturated compacted clayey soil at very small strains. Advanced experimental unsaturated soil mechanics EXPERUS 2005,
- Miao, L., Liu, S., and Lai, Y. (2002). Research of soil–water characteristics and shear strength features of Nanyang expansive soil. *Engineering Geology*, 65(4), 261-267. [https://doi.org/https://doi.org/10.1016/S0013-7952\(01\)00136-3](https://doi.org/https://doi.org/10.1016/S0013-7952(01)00136-3)
- Minasny, B., Chaney, N. W., Maggi, F., Giap, S. G. E., Shah, R. M., Fiantis, D., and Setiawan, B. I. (2021). Pedotransfer functions for estimating soil hydraulic properties from saturation to dryness. *Geoderma*, 403, 115194.
- Morales, L., Romero, E., Jommi, C., Garzón, E., and Giménez, A. (2015). Ageing effects on the small-strain stiffness of a bio-treated compacted soil. *Géotechnique Letters*, 5(3), 217-223. <https://doi.org/10.1680/jgele.15.00044>
- Mualem, Y. (1976). A new model for predicting the hydraulic conductivity of unsaturated porous media. *Water resources research*, 12(3), 513-522.
- Naghadeh, R. A., and Toker, N. K. (2019). Exponential Equation for Predicting Shear Strength Envelope of Unsaturated Soils. *International Journal of Geomechanics*, 19(7), 04019061. [https://doi.org/doi:10.1061/\(ASCE\)GM.1943-5622.0001435](https://doi.org/doi:10.1061/(ASCE)GM.1943-5622.0001435)

- Nam, S., Gutierrez, M., Diplas, P., Petrie, J., Wayllace, A., Lu, N., and Muñoz, J. J. (2010). Comparison of testing techniques and models for establishing the SWCC of riverbank soils. *Engineering Geology*, 110(1), 1-10. <https://doi.org/https://doi.org/10.1016/j.enggeo.2009.09.003>
- Ng, C. W. W., and Peprah-Manu, D. (2023). Pore structure effects on the water retention behaviour of a compacted silty sand soil subjected to drying-wetting cycles. *Engineering Geology*, 313, 106963. <https://doi.org/https://doi.org/10.1016/j.enggeo.2022.106963>
- Ng, C. W. W., Xu, J., and Yung, S. Y. (2009). Effects of wetting–drying and stress ratio on anisotropic stiffness of an unsaturated soil at very small strains. *Canadian Geotechnical Journal*, 46(9), 1062-1076. <https://doi.org/10.1139/t09-043>
- Ng, C. W. W., and Yung, S. Y. (2008). Determination of the anisotropic shear stiffness of an unsaturated decomposed soil. *Géotechnique*, 58(1), 23-35. <https://doi.org/10.1680/geot.2008.58.1.23>
- Ngoc, T. P., Fatahi, B., and Khabbaz, H. (2019). Impacts of Drying-Wetting and Loading-Unloading Cycles on Small Strain Shear Modulus of Unsaturated Soils. *International Journal of Geomechanics*, 19(8), 04019090. [https://doi.org/doi:10.1061/\(ASCE\)GM.1943-5622.0001463](https://doi.org/doi:10.1061/(ASCE)GM.1943-5622.0001463)
- Ngoc, T. P., Fatahi, B., Khabbaz, H., and Sheng, D. (2020). Impacts of matric suction equalization on small strain shear modulus of soils during air drying. *Canadian Geotechnical Journal*, 57(12), 1982-1997. <https://doi.org/10.1139/cgj-2019-0742>
- Oh, W. T., and Vanapalli, S. K. (2014). Semi-empirical model for estimating the small-strain shear modulus of unsaturated non-plastic sandy soils. 32, 259-271.
- Oh, W. T., Vanapalli, S. K., and Puppala, A. J. (2009). Semi-empirical model for the prediction of modulus of elasticity for unsaturated soils. *Canadian Geotechnical Journal*, 46(8), 903-914. <https://doi.org/10.1139/t09-030>
- Oloo, S. Y., and Fredlund, D. G. (1996). A method for determination of ϕ_b for statically compacted soils. *Canadian Geotechnical Journal*, 33(2), 272-280. <https://doi.org/10.1139/t96-006>
- Pham, H., Fredlund, D., and Barbour, S. L. (2002). A simple soil-water hysteresis model for predicting the boundary wetting curve. Proceedings of the 55th Canadian Geotechnical Conference, Ground and Water-Theory to Practice, Niagara Falls, Ontario, pp 20-23,
- Pham, T. A., and Sutman, M. (2023). An analytical model for predicting the shear strength of unsaturated soils. *Proceedings of the Institution of Civil Engineers - Geotechnical Engineering*, 176(4), 369-387. <https://doi.org/10.1680/jgeen.21.00135>
- Pittaki-Chrysodonta, Z., Moldrup, P., Knadel, M., Iversen, B. V., Hermansen, C., Greve, M. H., and de Jonge, L. W. (2018). Predicting the Campbell soil water retention function: Comparing visible–near-infrared spectroscopy with classical pedotransfer function. *Vadose Zone Journal*, 17(1), 1-12.
- Pittaki-Chrysodonta, Z., Hartemink, A. E., and Huang, J. (2021). Rapid estimation of a soil–water retention curve using visible–near infrared spectroscopy. *Journal of hydrology*, 603, 127195. <https://doi.org/https://doi.org/10.1016/j.jhydrol.2021.127195>

- Rahardjo, H., Heng, O. B., and Choon, L. E. (2004). Shear strength of a compacted residual soil from consolidated drained and constant water content triaxial tests. *Canadian Geotechnical Journal*, 41(3), 421-436. <https://doi.org/10.1139/t03-093>
- Rahardjo, H., Kim, Y., and Satyanaga, A. (2019). Role of unsaturated soil mechanics in geotechnical engineering. *International Journal of Geo-Engineering*, 10(1), 8. <https://doi.org/10.1186/s40703-019-0104-8>
- Rassam, D. W., and Williams, D. J. (1999). A relationship describing the shear strength of unsaturated soils. *Canadian Geotechnical Journal*, 36(2), 363-368. <https://doi.org/10.1139/t98-102>
- Romana-Giraldo, J., and Bryson, L. S. (2023). Geophysics-based approach to predict triaxial undrained and drained compressive behavior in soft soils. *Journal of Applied Geophysics*, 213, 105022.
- Romero-Ruiz, A., Linde, N., Keller, T., and Dani, O. (2018). A review of geophysical methods for soil structure characterization. *Reviews of Geophysics*, 56.
- Roodposhti, H. R., Hafizi, M. K., Kermani, M. R. S., and Nik, M. R. G. (2019). Electrical resistivity method for water content and compaction evaluation, a laboratory test on construction material. *Journal of Applied Geophysics*, 168, 49-58. <https://doi.org/https://doi.org/10.1016/j.jappgeo.2019.05.015>
- Sawangsurriya, A., Edil, T. B., and Bosscher, P. J. (2009). Modulus-Suction-Moisture Relationship for Compacted Soils in Postcompaction State. *Journal of Geotechnical and Geoenvironmental Engineering*, 135(10), 1390-1403. [https://doi.org/doi:10.1061/\(ASCE\)GT.1943-5606.0000108](https://doi.org/doi:10.1061/(ASCE)GT.1943-5606.0000108)
- Schaap, M. G., Leij, F. J., and Van Genuchten, M. T. (1998). Neural network analysis for hierarchical prediction of soil hydraulic properties. *Soil Science Society of America Journal*, 62(4), 847-855.
- Schaap, M. G., Leij, F. J., and Van Genuchten, M. T. (2001). Rosetta: A computer program for estimating soil hydraulic parameters with hierarchical pedotransfer functions. *Journal of hydrology*, 251(3-4), 163-176.
- Schnellmann, R., Rahardjo, H., and Schneider, H. R. (2013). Unsaturated shear strength of a silty sand. *Engineering Geology*, 162, 88-96. <https://doi.org/https://doi.org/10.1016/j.enggeo.2013.05.011>
- Schnellmann, R., Rahardjo, H., and Schneider, H. R. (2015). Controlling parameter for unsaturated soil property functions: validated on the unsaturated shear strength. *Canadian Geotechnical Journal*, 52(3), 374-381. <https://doi.org/10.1139/cgj-2013-0278>
- Shi, J., Xiao, Y., Hu, J., Wu, H., Liu, H., and Haegeman, W. (2022). Small-strain shear modulus of calcareous sand under anisotropic consolidation. *Canadian Geotechnical Journal*, 59(6), 878-888. <https://doi.org/10.1139/cgj-2021-0329>
- Simunek, J., Van Genuchten, M. T., and Sejna, M. (2005). The HYDRUS-1D software package for simulating the one-dimensional movement of water, heat, and multiple solutes in variably-saturated media. *University of California-Riverside Research Reports*, 3, 1-240.
- Sivakumar, V., Kodikara, J., O'Hagan, R., Hughes, D., Cairns, P., and Mckinley, J. D. (2013). Effects of confining pressure and water content on performance of unsaturated compacted clay under repeated loading. *Géotechnique*, 63(8), 628-640. <https://doi.org/10.1680/geot.10.P.103>

- Soltani, A., Azimi, M., Boroomandnia, A., and O'Kelly, B. C. (2021). An objective framework for determination of the air-entry value from the soil–water characteristic curve. *Results in Engineering*, 12, 100298. <https://doi.org/https://doi.org/10.1016/j.rineng.2021.100298>
- Song, Y.-S., and Hong, S. (2020). Effect of clay minerals on the suction stress of unsaturated soils. *Engineering Geology*, 269, 105571. <https://doi.org/https://doi.org/10.1016/j.enggeo.2020.105571>
- Takkabutr, P. (2006). *Experimental investigations on small-strain stiffness properties of partially saturated soils via resonant column and bender element testing* [Doctoral Dissertation, The University of Texas at Arlington].
- Taukoor, V., Rutherford, C. J., and Olson, S. M. (2019). A semi-empirical relationship for the small-strain shear modulus of soft clays. *E3S Web Conf.*, 92, 04005. <https://doi.org/10.1051/e3sconf/20199204005>
- Thu, T. M., Rahardjo, H., and Leong, E.-C. (2006). Shear Strength and Pore-Water Pressure Characteristics during Constant Water Content Triaxial Tests. *Journal of Geotechnical and Geoenvironmental Engineering*, 132(3), 411-419. [https://doi.org/doi:10.1061/\(ASCE\)1090-0241\(2006\)132:3\(411\)](https://doi.org/doi:10.1061/(ASCE)1090-0241(2006)132:3(411))
- Tran, T. P. A., Fredlund, D. G., and Vanapalli, S. (2023). Anchor Conditions for Estimated Unsaturated Shear Strength Functions. *Canadian Geotechnical Journal*. <https://doi.org/10.1139/cgj-2022-0255>
- Tso, C. H. M., Kuras, O., and Binley, A. (2019). On the field estimation of moisture content using electrical geophysics: The impact of petrophysical model uncertainty. *Water resources research*, 55(8), 7196-7211.
- van Genuchten, M. T. (1980). A Closed-form Equation for Predicting the Hydraulic Conductivity of Unsaturated Soils. *Soil Science Society of America Journal*, 44(5), 892-898. <https://doi.org/https://doi.org/10.2136/sssaj1980.03615995004400050002x>
- Vanapalli, S. K., Fredlund, D. G., Pufahl, D. E., and Clifton, A. W. (1996). Model for the prediction of shear strength with respect to soil suction. *Canadian Geotechnical Journal*, 33(3), 379-392. <https://doi.org/10.1139/t96-060>
- Viggiani, G., and Atkinson, J. (1995). Interpretation of bender element tests. *Géotechnique*, 45(1), 149-154.
- Wang, F., Li, D., Du, W., Zarei, C., and Liu, Y. (2021). Bender Element Measurement for Small-Strain Shear Modulus of Compacted Loess. *International Journal of Geomechanics*, 21(5), 04021063. [https://doi.org/doi:10.1061/\(ASCE\)GM.1943-5622.0002004](https://doi.org/doi:10.1061/(ASCE)GM.1943-5622.0002004)
- Wang, H.-L., Yin, Z.-Y., Zhang, P., and Jin, Y.-F. (2020). Straightforward prediction for air-entry value of compacted soils using machine learning algorithms. *Engineering Geology*, 279, 105911. <https://doi.org/https://doi.org/10.1016/j.enggeo.2020.105911>
- Wassar, F., Gandolfi, C., Rienzner, M., Chiaradia, E. A., and Bernardoni, E. (2016). Predicted and measured soil retention curve parameters in Lombardy region north of Italy. *International Soil and Water Conservation Research*, 4(3), 207-214. <https://doi.org/https://doi.org/10.1016/j.iswcr.2016.05.005>

- Xu, J., and Zhou, C. (2016). A simple model for the hysteretic elastic shear modulus of unsaturated soils. *Journal of Zhejiang University-SCIENCE A*, 17(7), 589-596. <https://doi.org/10.1631/jzus.A1600300>
- Yan, J., Kong, L., and Wang, J. (2023). Evolution law of small strain shear modulus of expansive soil: From a damage perspective. *Engineering Geology*, 315, 107017. <https://doi.org/https://doi.org/10.1016/j.enggeo.2023.107017>
- Yan, K., Wang, Y., Yang, Z., Lai, X., and Chen, C. (2022). Experimental Study on Small-Strain Shear Modulus of Unsaturated Silty-Fine Sand. *Applied Sciences*, 12(17), 8743. <https://www.mdpi.com/2076-3417/12/17/8743>
- Yang, J., and Liu, X. (2016). Shear wave velocity and stiffness of sand: the role of non-plastic fines. *Géotechnique*, 66(6), 500-514.
- Zhai, Q., Rahardjo, H., Satyanaga, A., and Dai, G. (2019). Estimation of unsaturated shear strength from soil–water characteristic curve. *Acta Geotechnica*, 14(6), 1977-1990. <https://doi.org/10.1007/s11440-019-00785-y>
- Zhang, C., and Lu, N. (2019). Unitary Definition of Matric Suction. *Journal of Geotechnical and Geoenvironmental Engineering*, 145(2), 02818004. [https://doi.org/doi:10.1061/\(ASCE\)GT.1943-5606.0002004](https://doi.org/doi:10.1061/(ASCE)GT.1943-5606.0002004)
- Zhang, L., Zhang, S., Liu, X., and Sun, Y. (2021). Characterizing the Effect of Water Content on Small-Strain Shear Modulus of Qiantang Silt. *Journal of Marine Science and Engineering*, 9(12), 1363. <https://www.mdpi.com/2077-1312/9/12/1363>
- Zhou, A.-N., Sheng, D., Sloan, S. W., and Gens, A. (2012). Interpretation of unsaturated soil behaviour in the stress – Saturation space, I: Volume change and water retention behaviour. *Computers and Geotechnics*, 43, 178-187. <https://doi.org/https://doi.org/10.1016/j.compgeo.2012.04.010>
- Zhou, A., Huang, R., and Sheng, D. (2016). Capillary water retention curve and shear strength of unsaturated soils. *Canadian Geotechnical Journal*, 53(6), 974-987. <https://doi.org/10.1139/cgj-2015-0322>

VITA
LUCAS ACHEAMPONG

EDUCATION

Master of Science Civil Engineering 01/2022 – 05/2024

University of Kentucky, Lexington, Kentucky.

Bachelor of Science Geological Engineering 09/2015 - 05/2019

Kwame Nkrumah of Science and Technology, Kumasi, Ghana.

PROFESSIONAL EXPERIENCE

Graduate Research and Teaching Assistant 01/2022 – 05/2024

Department of Civil Engineering, University of Kentucky, Lexington, Kentucky

Materials Assistant 09/2019 - 11/2021

Geotechnical Lab, Ghana Highway Authority, Kumasi, Ghana.

Intern 01/2019 - 02/2019

CSIR-Building and Road Research Institute, Kumasi, Ghana

Intern 06/2018 - 08/2018

nextPlace Research Laboratory, University of Applied Science, Detmold, Germany

PROFESSIONAL SOCIETY

American Society of Civil Engineers

HONORARY SOCIETY

Chi Epsilon